Flow regimes and dryout in horizontal, heated tubes

by

Keith E. Crowe

B.S.M.E., Univ. of Lowell, Lowell, Massachusetts (1985)

M.S.M.E, M.I.T, Cambridge, Massachusetts (1988)

Submitted to the Department of
Mechanical Engineering
in partial fulfillment of the
requirements for the degree of

Doctor of Philosophy

at the

Massachusetts Institute of Technology

June, 1992

Signature of Author .....

Department of Mechanical Engineering

Certified by .....

Peter Griffith, Professor of Mechanical Engineering

Thesis Supervisor

Accepted by .....

Ain A. Sonin

Chairman, Departmental Committee on Graduate Students

Flow regimes and dryout

in horizontal, heated tubes

by

Keith E. Crowe

Submitted to the Department of Mechanical Engineering on

June 18, 1992 in partial fulfillment of the requirements

for the Degree of Doctor of Philosophy in Mechanical Engineering

Abstract

The operational limit of horizontal boiler tubes is often not dictated by heat transfer or pressure drop considerations but by dryout of the liquid film on the tube's upper surface. This phenomenon can result in tube wall overheating and rupture or thermally induced fatigue failure. Dryout, which can occur at low, intermediate, and high qualities corresponding to the stratified, slug and annular flow regimes, results from the tendency for the flow to stratify if the mass flux is insufficient. Different physical mechanisms control its occurrence in each regime. Therefore, the minimum mass flux for tube isothermal operation will depend on the most limiting dryout type under the given conditions.

The dryout limits were found experimentally in a horizontal two-inch diameter pipe operating at atmospheric pressure. The results were presented on superficial flow regime maps where the dryout was associated with flow regime type. A simple model incorporating the post-slug film drainage, evaporation and the frequency of slugging was constructed. The effects of bubble nucleation in the film were studied visually and deemed negligible. The film thickness evolution between consecutive slugs was measured with a flush conductance probe in an adiabatic, air-water system and compared to a simple drainage theory. The slug frequency was measured and correlated to various slug flow conditions for adiabatic and diabatic cases. The results indicate frequency augmentation with the application of heat flux. The model using these results compares conservatively with the dryout data in the intermittent flow regime. The stratified flow dryout limit, $Fr = 1$, is adequate to bound the low and intermediate quality anisothermal zones at atmospheric pressure. Entrance regions induced by minor fabrication defects in the piping system were found to have an adverse affect on the downstream thermal field.

The physical mechanisms responsible for the existence of horizontal annular flow have not been well quantified. The onset of annular flow, which is essentially a dryout bound, was located experimentally. The mechanism of circumferential secondary flow in the vapor core was argued to be a principle effect in establishing a continuous liquid annulus under the conditions near this stratified - annular transition. A simple, physically based model was assembled, which considers only the secondary flow mechanism, to predict this bound as a function of heat flux. The secondary flow in the gas core, which results from asymmetry of the liquid film distribution, was correlated to the gas core velocity and the

effective wall roughness using experimental data from a single phase air flow. Both laminar and turbulent film analyses were employed to determine if the film flow to the pipe top is sufficient under the imposed heat loading. The resulting flow transition bound using the secondary flow-laminar film model is in fair agreement with the data.

Thesis Supervisor: Peter Griffith, Professor of Mechanical Engineering

Acknowledgements

I would like to thank all those who made this research project possible and whose contributions greatly facilitated the work. First, I thank Professor Peter Griffith for his insight, guidance, and patience over the past three years. The opportunity to work with Professor Griffith will certainly prove invaluable in the years to come. We are grateful to the Department of Energy for funding this research.

Thanks to Professors Leon Glicksman and Harri Kytomaa for taking the time to serve on my thesis committee. Our meetings were interesting and insightful. Thanks to Professor Shahryar Motakef for the extensive computational support. The computational facility is a tremendous asset to the Heat Transfer Laboratory which enriched this work considerably.

Infinite thanks to Patrick Robert Griffin whose help and support is hard to measure. From helping me think through research problems, to helping me deal with computer-phobia, to talking about personal dilemmas, Patrick is a jack-of-all-trades who was never too busy.

Graduate school often makes the road rough for a relationship. I thank Melissa Page for her continuous love, patience, and support, throughout all the difficult times.

Thanks to my colleague Aaron Flores whose annular flow experiments helped support a major portion of my work. Thanks also to Joseph (Tiny) Caloggero and his staff, Norm and Bob, for the fabrication of the experimental apparatus used in this project and for much technical advice over the years.

Thanks to Kevin Kelly for the companionship during the early years while we were taking classes, studying for qualifiers, and taking part in philosophical discussions at the Muddy Charles. Thanks also to Mike Lints, Tony Varone, Bruce Easom, Jayanta Kapat, Arlene Lanciani-Marge and the rest of the students of the Heat Transfer Laboratory who have helped make my stay at M.I.T. more enjoyable.

Finally, I am very grateful to my father for his continued support and tolerance of the "professional student" in the family.

List of Figures

Nomenclature

Symbol	Definition
D	Pipe diameter
ΔT	Top - Bottom temperature difference across pipe
δ	liquid film thickness
Fr,F	Froude number
g	Gravitational acceleration
ν	Kinematic viscosity
q''	Heat flux
R	Pipe radius
ρ	Density
u	Film circumferential velocity component
w	Film axial velocity component
j	Superficial velocity
τ	Shear stress, time constant
θ	Circumferential coordinate, as measured from pipe top
x	Thermodynamic quality
y	Radial inward coordinate
z	Axial coordinate
P	Pressure
G	Mass flux
σ	Surface tension
X	Martinelli parameter
r	Pipe bend radius
h_{fg}	Evaporation enthalpy
U	Velocity
Re	Reynolds number
k	Thermal conductivity
c	Specific heat

b	Pipe wall thickness
Pr	Prandtl number
h	Heat transfer coefficient, liquid level
v_{fg}	Volume change of evaporation
T	Temperature
V	Voltage
Γ , Q	Film flow rate
μ	Dynamic viscosity
C_f	Skin friction coefficient
λ	Friction factor
κ	von Karman constant

Subscripts

Subscript	Meaning
g	gas
l	liquid
o	initial
t	top, turbulent
b	bottom
cl	centerline
ave	average value
sat	saturation value
w	wall value
i	incipient, interfacial, interchange
eff	effective value
ss	stainless steel
axi	axial
sec	secondary

Table of Contents

CHAPTER 1

Introduction

Horizontal heated tubes find use in a wide variety of heat exchange components. These include once-through boilers and fluidized bed combustors (FBC). The use of horizontal tubes is driven by certain advantages inherent to this geometry. Two-phase pressure drop associated with horizontal tubes is lower than that for vertical upflow tubes all else being equal. Also, horizontal flow is more stable because the pressure drop-flow rate instabilities inherent in downflow are not present.

Horizontal steam generating tubes must be designed to provide effective heat transfer with a minimum of pressure drop at the given operating conditions. In addition to these considerations, tube life influences the design process as well. As will be seen, tube operating life is highly dependent on the prevailing flow regime. In once-through boilers, the horizontal tubes must carry two-phase fluid mixtures that pass through several different flow regimes in which the structure of the flow varies considerably. As a result, these tubes must be designed to give effective heat transfer, with minimal pressure drop, for an extended lifetime, under conditions that are continually changing through the pipeline.

1.1. Parameters influencing tube life

Typical parameters used in horizontal boiler tubes are controlled by the necessary heat transfer and the acceptable pressure drop. Pressure drop is very sensitive to diameter; to first order depending on D^5. However, heat transfer is better for smaller sizes and the tradeoff occurs for sizes between one and two inch. For power production, high pressures, in the range of 600 to 1000 psi, are employed. To minimize space, the heat fluxes are made as large as possible provided they are below the critical heat flux (CHF). The application of heat flux is often circumferentially non-uniform in the applications of interest. Though non-uniform heat flux may have a small effect on the two-phase flow regime, the effect on the temperature field in a tube that carries a thermally detrimental flow regime is not well known but potentially hazardous.

CHF marks the onset of a heat transfer regime change where nucleate boiling gives way to film boiling and the heat transfer coefficient falls markedly. A dry wall condition results with associated high wall temperature which can cause tube corrosion and failure. CHF is by now well documented and an easily calculated *heat transfer* phenomenon.

In a heat exchanger, the tube outside is usually heated by hot, gaseous products of combustion, so the outside heat transfer coefficient represents the limiting resistance to heat transfer. Thus, the heat transfer is not affected much by the inside (waterside) mass flux. The phenomenon that dictates the minimum mass flux through the tube is another dry wall condition which is referred to as *dryout*. Many researchers have used the term dryout interchangeably with *burnout* or CHF, but in fact dryout is almost purely hydrodynamic in origin and can lead to exceedingly high wall temperatures

even at low heat flux.

1.2. Description of dryout

Though dryout can occur in vertical tubes, the problem is more complicated and prevalent in horizontal tubes. The reason for this lies in the inherent asymmetry of the liquid distribution caused by gravity. In the case of two-phase flow where the tube does not run full of liquid, gravity continually acts to bring liquid to the bottom of the tube, depleting the top of coolant. Three of the four major flow regimes found in horizontal flow have an associated dry top wall condition. The mechanism governing the dryout in each of these regimes is different however. In a once-through boiler, it may be possible to experience all three dryouts at different locations in the system. The elimination of dryout will be governed by the minimum liquid mass flux that removes the most limiting dryout type, which in turn depends on the precise conditions used in the tube.

In this research, all three dryout types were studied in a two inch, atmospheric, horizontal tube. In particular, dryout associated with intermittent flow (moderate quality) and annular flow (high quality) are not well understood and have constituted the major portion of the work presented. Stratified (low quality) dryout has been previously studied more extensively and is more predictable.

There are various problems associated with tube wall dryout. Clearly, in the locations inside the tube that are depleted of liquid there is a substantial reduction of the heat transfer coefficient. Most important, there is an associated overheating of the tube wall material. At the high heat fluxes used in industrial heat exchangers, the tube

temperature can easily exceed the creep limit, which for steel is around 850^0F. High pressure systems would not require temperature this high to produce a rupture. Associated with intermittent intermittent dryout giving rise to periodic temperature rises in the tube wall. Though the amplitude of these temperature oscillations may not be that high, the periodic thermal stress induced can produce fatigue failure. For example, if one assumes that the endurance limit is about half of the yield strength, it can be shown that temperature variations over time in excess of $40\Delta^0$F will ultimately fail a two-inch stainless steel tube. Finally, the exceedingly high temperature, or periodic heating and quenching will certainly lead to accelerated corrosion which affects tube life, heat transfer and pressure drop.

To deal with this problem in practice several remedies have been employed. The asymmetry of the flow (stratification) can be reduced by introducing *swirl* to the liquid, either with rifled tubes or by a spiral swirl device. These suffer from the disadvantages of increasing the pressure drop and the initial cost particularly in the case of rifled tubes.

Another solution is to raise the mass flux throughout the whole system. Increasing the velocity so that the pipe runs full counteracts the stratifying effect of gravity and will maintain liquid at the tube top in all flow regimes. The drawback is the increased pumping power. The power consumed will roughly depend on the cube of the flow rate (V^3) so this can represent an expensive solution as well. For example, if the flow was about 10% higher than actually necessary to keep the tube wet, this would require pumping power one third greater than the minimum necessary. Therefore it is important to know precisely what the liquid flow dryout limit is.

1.3. Thermal and hydrodynamic bounds

As mentioned, there are four major flow regimes in horizontal two-phase flow. A sketch of what these regimes look like is shown in Figure 1.1. Only the dispersed bubble flow regime, which is only attainable with very high liquid flow rates, is benign under all conditions. The stratified, intermittent (slug), and annular flow regimes all can experience dryout. Annular flow dryout can be associated with the onset of annular flow where the structure is basically annular, but at the top of the pipe, the annulus is incomplete. Annular flow dryout can also occur at very high quality when the tube begins to run out of liquid, so the annulus disappears at the top.

To understand this hydrodynamic dryout it is important to understand the flow regimes. Flow regimes transitions have been successfully defined by Taitel & Dukler[1] on maps that use the most generalized non-dimensional variables. These non-dimensional parameters are rather obscure and difficult to use. For a given set of operating conditions, the maps can be transformed into a dimensional mapping using the superficial velocity coordinates. These maps are more physically understandable and of more practical use since the superficial quantities are readily calculated. Shown in Figure 1.2, is such a map constructed for two inch pipe for steam and water under adiabatic, atmospheric conditions. Also shown is an operating locus, that is a locus of two-phase flow states encountered in a heated system. As one moves along the locus from left to right, the gas velocity increases and the liquid velocity decreases as the thermodynamic quality increases. Clearly, the system can run through multiple flow regimes and perhaps multiple dryouts. The essential purpose of this research is to determine the range of conditions under which dryout occurs, what type of dryout it is

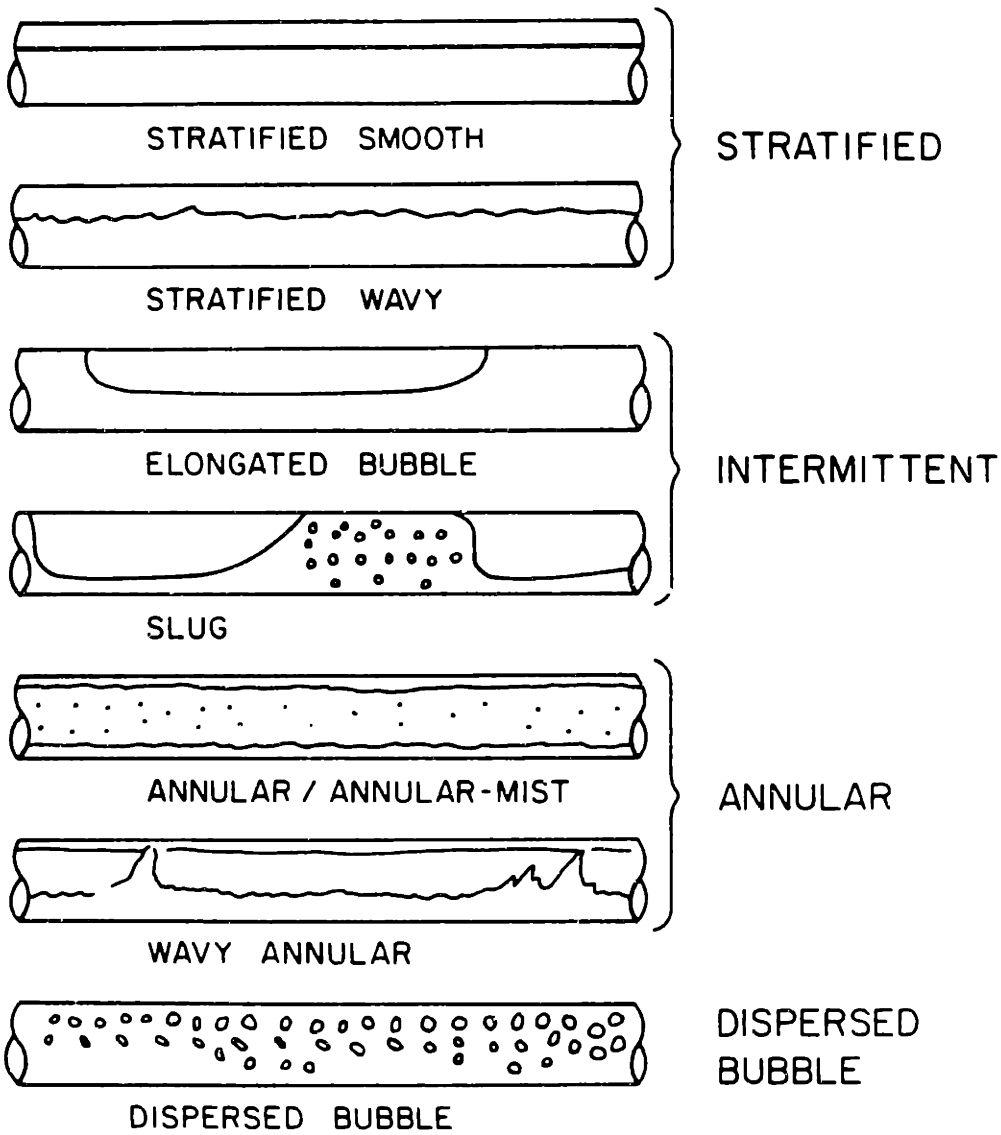

Figure 1.1: Flow regime types in horizontal flow. From reference 1

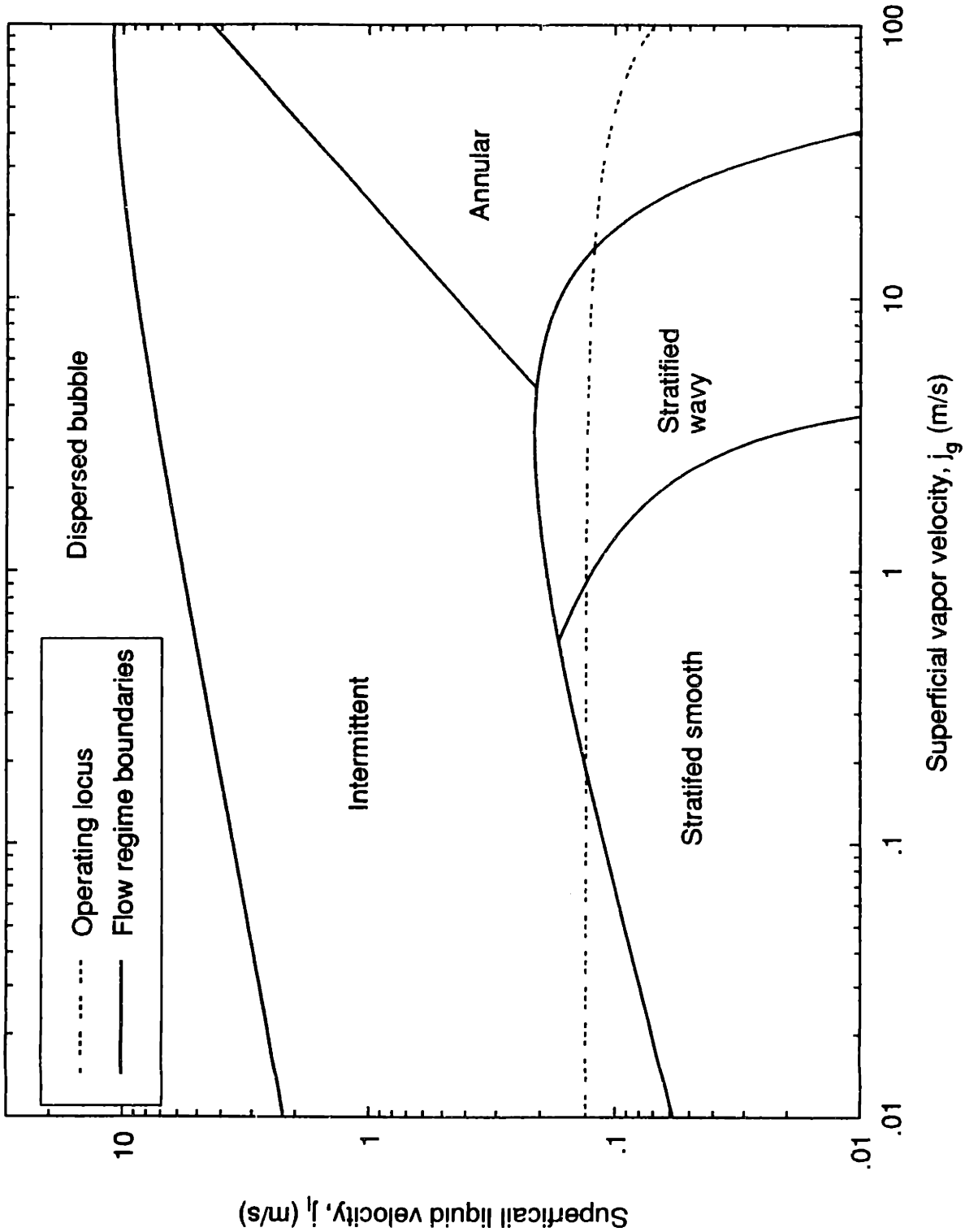

Figure 1.2: Flow regime map for two-inch horizontal tube

and to correlate it on a flow regime map of the type shown in Figure 1.2 in the form of *thermal boundaries*. These thermal boundaries will delineate the regions of (un)acceptable operating conditions.

The map in Figure 1.2 is only appropriate for the specific operating conditions in question. To parameterize the thermal bounds as a function of pressure, heat flux and diameter, it would be necessary to run many experiments and construct many maps. It does not seem possible construct a general thermal bound for use on a general hydrodynamic map since it is not likely that dryout bounds scale in the same way as the hydrodynamic bounds. Thus, a major thrust in this research was to build physically based models of the mechanisms influencing dryout in order to predict the thermal bounds under more general operating conditions.

1.4. Variables influencing dryout

The parameters influencing dryout in horizontal flow are numerous and cover a wide range, the important ones being tube diameter, heat flux, operating pressure, and tube inclination. Somewhat less quantifyable are heat flux distribution and inlet (or upstream) conditions. As will be seen, there are four possible effects that control the dryout in the most complex case of intermittent flow. These are post-slug film evaporation and drainage as well as nucleation effects in the film and the period of the intermittency. The role of each of these will be quantified and an attempt will be made to determine how these mechanisms scale with the above parameters.

1.5. Outline of thesis

The presentation of the research effort will be given as follows: Chapter two reviews the relevant literature on two-phase flow regimes and previous dryout work. Chapter three introduces the experimental apparati and method of determining the thermal bounds. Chapter four presents the intermittent dryout data. Chapter five discusses the assembly of the intermittent dryout model and makes comparison to the experimental data. Chapter five also describes the auxiliary experiments used to examine the dryout mechanisms individually. Chapters six and seven concern dryout associated with the onset of annular flow, the former presenting further literature review and background on the current understanding of the physics of annular flow. Chapter seven explains the modeling approach used to predict the onset of annular flow and provides a comparison with the dryout data. Chapter eight presents the conclusions of this study.

CHAPTER 2

Review of the Horizontal Flow Dryout Literature

Understanding the physics of dryout has motivated a need to correlate the dryout bounds with flow regimes. For example, if the dispersed bubble regime and the annular dispersed liquid regime can be shown to be thermally benign, one can be assured that the thermal bound will lie only in the stratified or slug regions on the hydrodynamic map. A useful starting point for the literature review is the flow regime information.

2.1. Flow Regimes

There have been four major regimes identified by numerous researchers although some have classified subsets of these. The stratified, intermittent, annular, and dispersed bubble flows each have a regime of prevalence which depends on the phase velocities, pipe diameter and fluid properties. The boundaries delineating these regimes have been determined theoretically by Taitel & Dukler.[1] Each boundary is governed by a critical value of a different dimensionless group because the transition physics is different for each boundary. In the most general form, the boundaries for horizontal flow are plotted in the form of parameters F, T, K vs. the dimensionless

liquid level h/D. The liquid level is correlated to the Martinelli parameter, X which is defined as:

$$X = \sqrt{\frac{(dP/dz)_g}{(dP/dz)_l}} \tag{2-1}$$

where the pressure gradients are computed as if the each phase occupied the pipe alone. Figure 2.1 shows the generalized map while Figure 2.2 shows the liquid level curve for horizontal, adiabatic flow.

Of course, since F,T,K and X depend on the fluid properties, flow rates, and geometry, the above generalized map can be converted to superficial velocity coordinates which is more useful and physically understandable. An example of this conversion for adiabatic flow in a two inch pipe is shown in Figure 2.3. Also given on the plot are the air-water data of Mandhane.[2] As seen, the agreement between the boundaries found experimentally by Mandhane and the theory of Taitel & Dukler[1] is quite good. A comparison of Mandhane's one inch pipe data also shows good agreement, indicating the bounds scale correctly with diameter.

In fact, many data sets agree well with the Taitel & Dukler maps, however it was observed by Weisman[3] that the main shortcoming was the boundary between the intermittent and annular flow regimes. Taitel & Dukler simply stated that a liquid level less than 0.5 was not enough to support a complete tube blockage by the liquid phase and annular flow must prevail. Weisman observed that the boundary is less dependent on the liquid flow than dictated by h/D = 0.5 and proposed the following correlation which agrees with a wide variety of data sets:

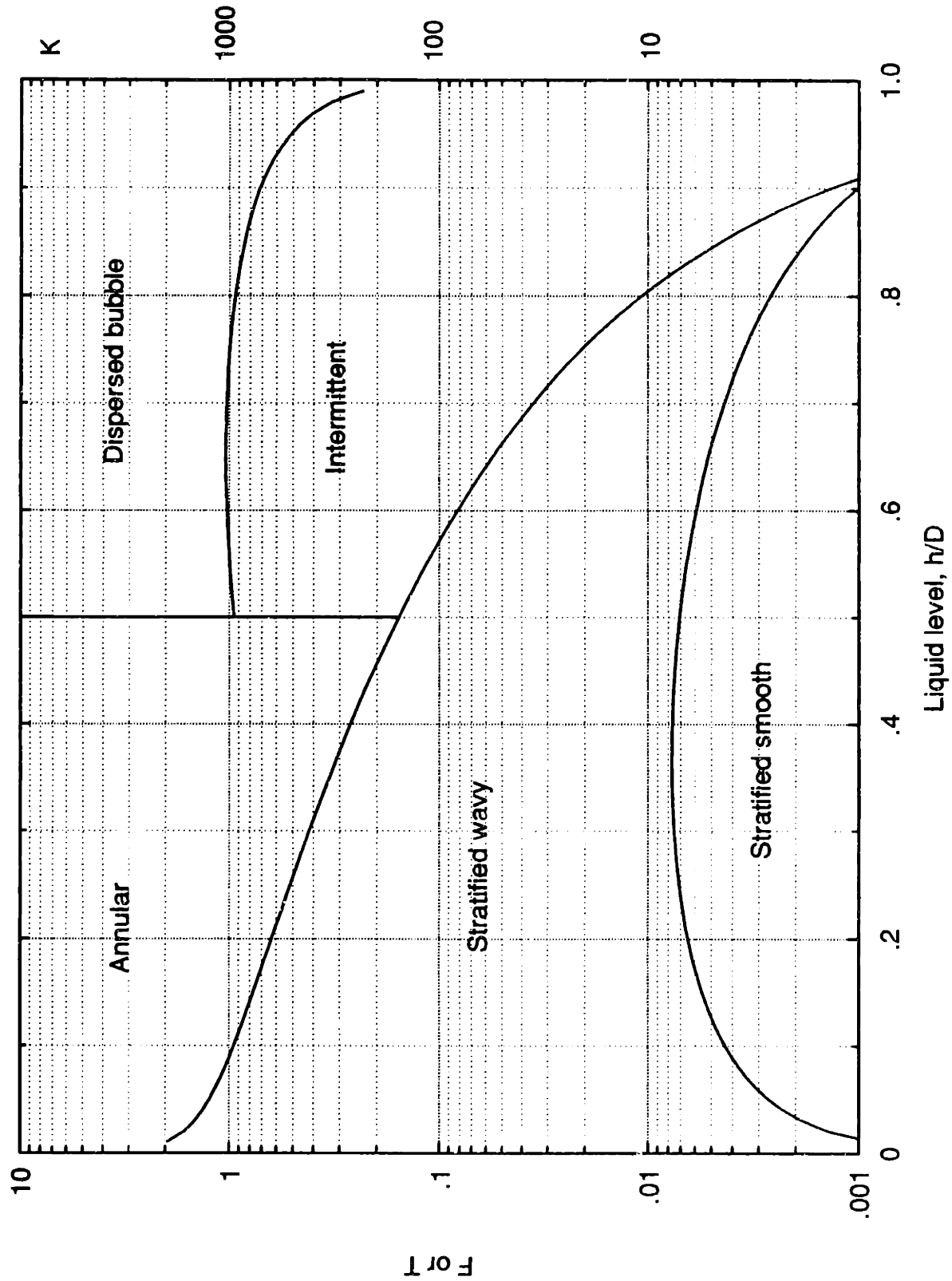

Figure 2.1: Generalized flow regime map

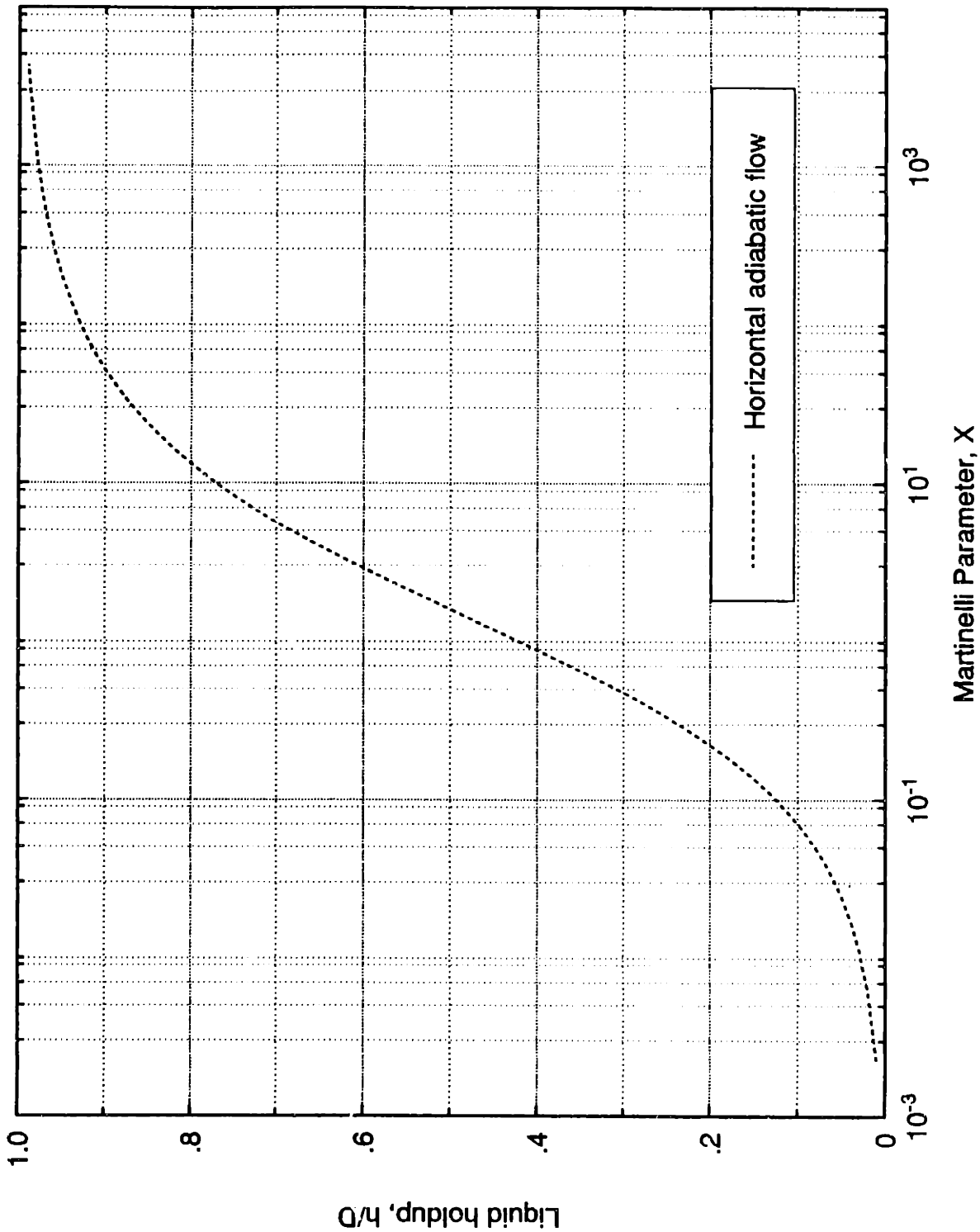

Figure 2.2: Equilibrium liquid level curve for horizontal adiabatic flow

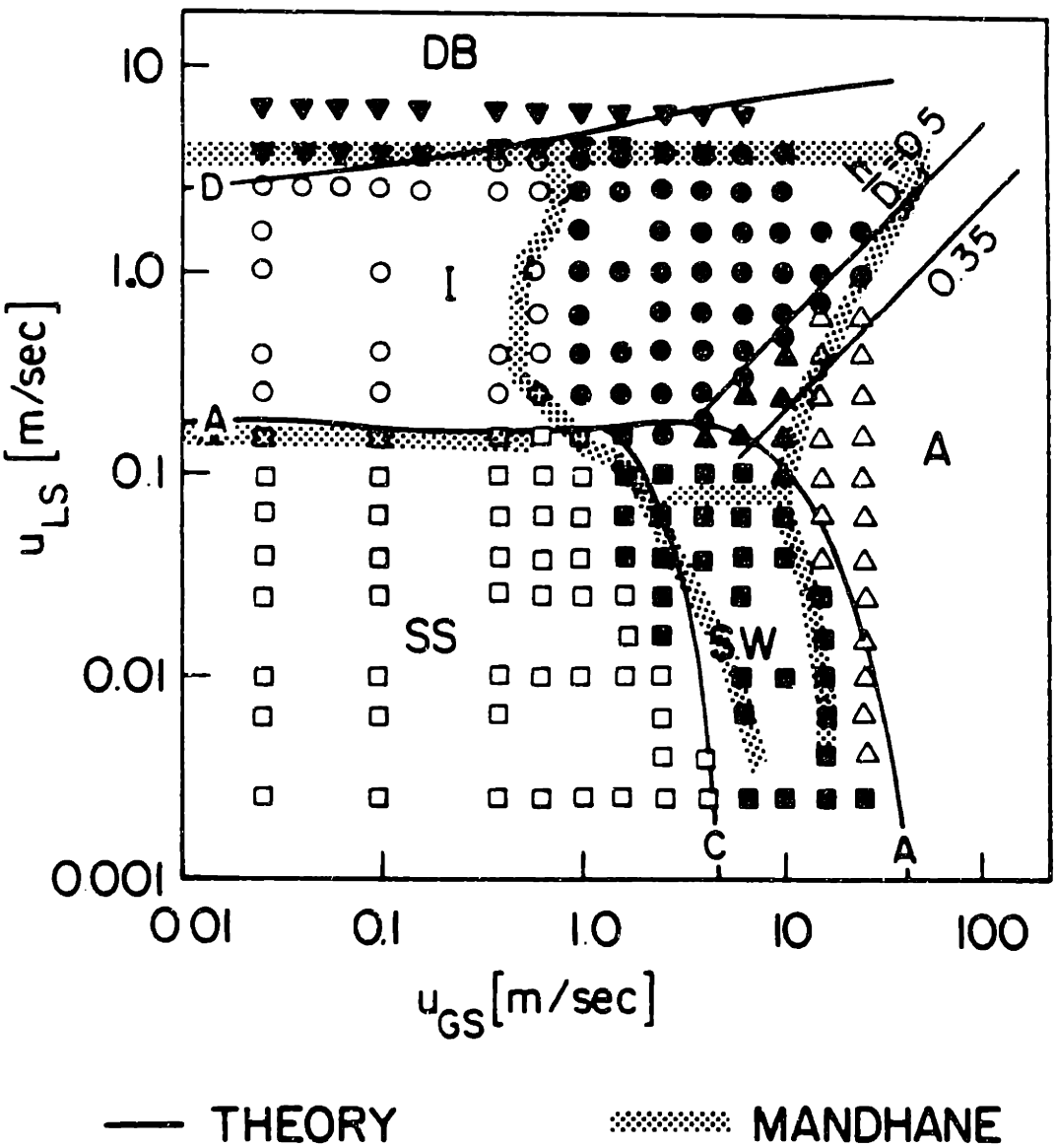

Figure 2.3: Flow regime map for 0.0508 m pipe with Mandhane's data. (See ref. 3)

$$Fr_g = \frac{j_g}{\sqrt{gD}} = \left[\frac{1.9(j_g/j_l)^{0.125}(g(\rho_l - \rho_g)\sigma)^{0.05}}{(\rho_g j_g^2)^{0.1}} \right]^{2.78} \quad (2\text{-}2)$$

This bound, shown in Figure 2.4, has a negative slope and is less dependent on the liquid velocity than the constant holdup line. The Taitel & Dukler hydrodynamic bounds with the correction of the Weisman intermittent-annular transition correctly predicts many data sets and is the generally accepted flow regime map for horizontal flow.

2.2. Dryout in Horizontal Pipes

The existence of dryout of the upper inside pipe surface under certain flow conditions has been known for some time. Only recently has the dryout been associated with flow regimes and classified by quality level, i.e. low, moderate, and high quality.

The earliest documented experience with circumferential wall temperature variations (occurrence of dryout) was that of Styrikovich & Miropolski[4] who conducted experiments in two inch pipe operating at pressures up to 182 bar. Lacking the tools to predict flow regimes, they concluded that the wall temperature variations were the result of the stratified flow and believed that avoiding this regime would ensure pipe isothermal operation. It was found that this condition could be avoided with an increase in the mass flux or by inclining the pipe in excess of 9.5^0. More recently, Ruder[5] in attempting to correlate thermal and hydrodynamic bounds found that the Styrikovich & Miropolski[4] data indicated that their flows were typically in the intermittent flow regime showing that pipe anisothermality could result in regimes other than stratified.

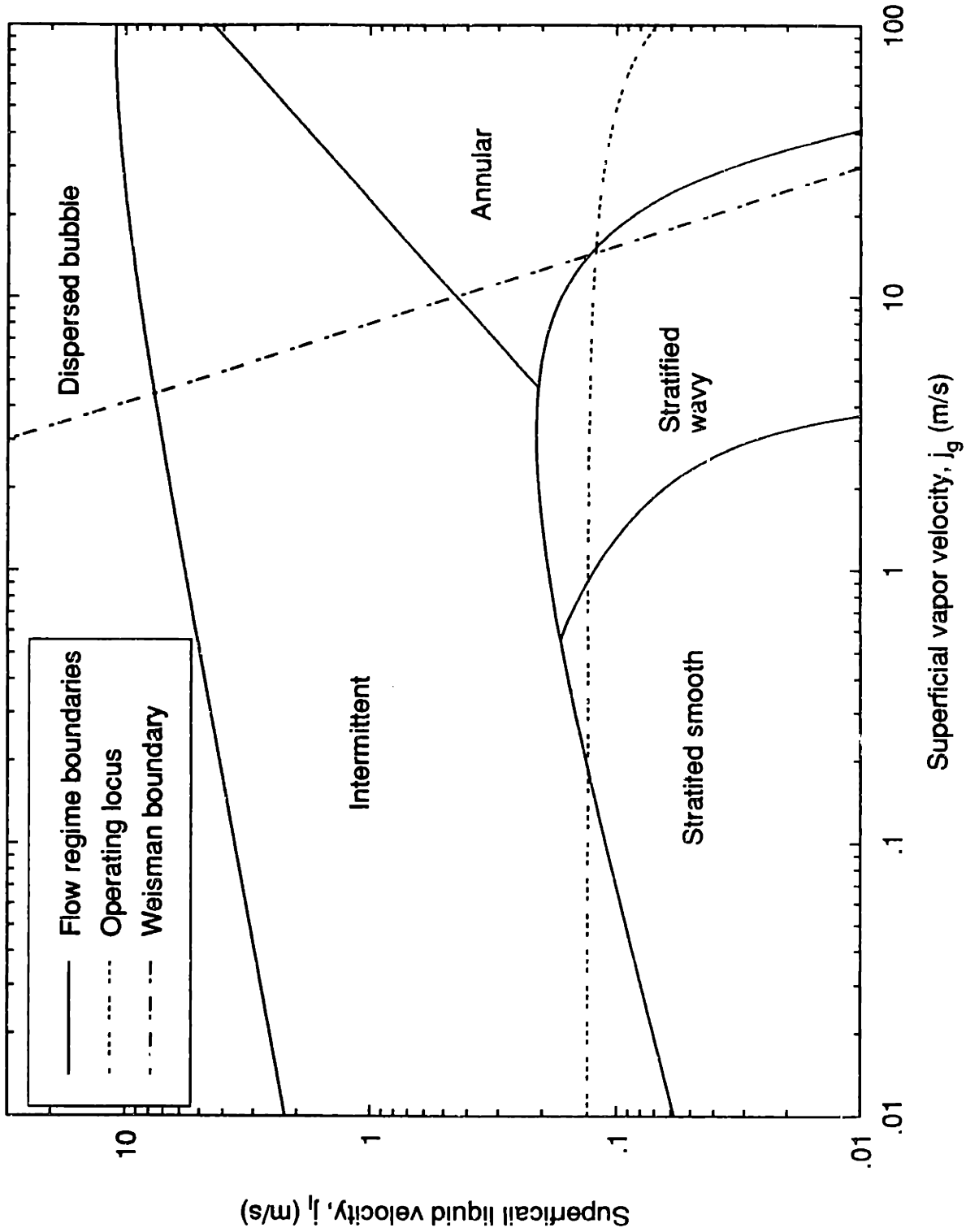

Figure 2.4: Flow regime map for two-inch horizontal adiabatic flow

There have been only a few dryout studies in horizontal lines since the work of Styrikovich & Miropolski, notably Lis & Strickland, Robertson, Fisher & Yu, and Ruder. The work of Lis & Strickland[6] involved a 41mm diameter test section that was preceded by a 180^0 bend either in a horizontal or vertical plane. Pressures up to 66.5 bar and heat fluxes up to 63 kW/m^2 were used. The quality range investigated was from zero to about 70% thus several flow regimes were encountered. A dryout zone was defined by either high steady temperatures (dry wall) or by oscillating temperatures as measured on the top external pipe surface. The dryout zone size was measured by both length of dried out pipe and quality range of dryout condition and is mapped as x vs. L/D. Lis & Strickland observed that a calming section placed after the bend having length of 56 D attenuated but did not eliminate the detrimental effects of the vertical bend, which was believed to effectively stratify the phases for some length downstream. The bend placed in the horizontal plane was not nearly as troublesome, giving rather modest anisothermality.

Inlet effects are believed to play a role in these experiments with respect to the location and causes of the dryout and it is not expected that the flow regime maps designed for fully-developed flow would be applicable in this case. However, the general trends observed are worth noting. An increase in heat flux increased the size of the dryout zone. Also, the minimum mass flux needed to eliminate the dryout zone increased rather substantially with pressure. Although no reference is made to the flow regimes, the quality where oscillating temperatures were found were nominally in the range or 5-40% which would, at these elevated pressures, correspond to intermittent and annular flow. In fact, a plot of the dryout boundary in the form of Froude number

(modified with the bend radius) vs steam volumetric flow rate indicated two straight lines of differing slope, interpreted as a regime change.

In a similar experiment to Lis & Strickland, Robertson[7] found the dryout bounds in both a 1/2 inch and 3/4 inch pipe at pressures between 500-1000 psi and heat flux up to 1 MW/m^2. Robertson observed that the minimum heat flux where dryout prevailed decreased with increasing pressure. Increasing diameter had a similar effect; the 3/4 inch pipes had a lower dryout heat flux than the smaller pipe, although the pressure effect was more pronounced. However, both of these pipe sizes had significantly lower dryout heat fluxes than a 1/2 inch vertical tube operating under the same conditions. This demonstrates the sensitivity of horizontally oriented pipes to the problematic dryout condition. The range of conditions were plotted on a Baker[8] flow regime map which indicated that all operating conditions were either in the annular or annular spray regimes. Robertson concluded that the annular regime without spray should be avoided for dryout considerations and that the presence of the vertical 180^0 bend tended to reduce the dryout heat flux just downstream of the bend particularly for larger diameters.

In what would appear to be a system identical to the one used by Lis & Strickland,[6] Fisher & Yu[9] found the dryout bounds in a serpentine evaporator employing Freon-12 as the working fluid. They hypothesized that increased pressure would help to alleviate the dryout problem because as the density ratio tends toward unity, the tendency for stratification is less. The diameter was fixed at 41 mm and heat fluxes up to 18.5 kW/m^2 were used. Pressures of 1 MPa and 3.55 MPa were used corresponding to 6.65 MPa and 18 MPa of steam-water, respectively, dictated by matching the

vapor-liquid density ratio.

The dryout data was plotted in the same way as the Lis & Strickland[6] data where a plot of quality vs. L/D indicated a zone of either steady high temperatures or oscillating temperatures. The data show very similar trends. Typically, dryout was initiated between 5-30 D past the bend and both increasing heat flux and pressure had adverse effects on the size of the dryout zones. To eliminate dryout entirely at the highest heat flux it was necessary to raise the mass flux up to 2530 kg/m^2s (U_{l_0} = 2.92m/s). These authors found that both the Lis & Strickland data and the low pressure F-12 data could be correlated by:

$$\frac{\rho_g j_g^2}{(\rho_l-\rho_g)gR}\left[\frac{R}{r}\right]^{0.2} = 17.0x-0.2 \qquad (2\text{-}3)$$

It is interesting to note that this correlation was appropriate for both the dryout onset and the rewet. Apparently, the high pressure data was not correlated with this, but it was stated that rewetting did not occur at high pressure, further indicating that high pressure is more susceptible to dryout.

In addition to the thermal tests, Fisher & Yu made measurements of the film thickness after passage of a surge using a conductance probe designed and analyzed by Coney.[10] It was found that the film thickness as a function of time for air-water flow was accurately predicted by a model proposed by Coney.[11] The probe saturated at thicknesses of 250 μm, so the initial thickness of the liquid layer at the tube top after passage of surge was at least that much. As will be seen, this is a crucial number in the determination of dryout boundaries. Measurements were also made of the film thickness evolution in the heated case which gave the time to dryout as a function of

heat flux and it was found that these times were equal for systems with the same constant $\frac{q''}{\rho_l h_{fg}}$. The initial thickness for this comparison was 70 μm so the effect of gravitational draining was small. Based on these results, the authors suggested that knowledge of the surge frequency could lead to the prediction of a dryout bound.

Based on the evaluation of these works, it would seem that at least tentatively it may be concluded that there exists dryout of the tube upper surface at qualities corresponding to stratified, intermittent, and annular flow. In addition, the problem appears to be accentuated at higher pressure and heat flux due to the enhanced evaporation rate of the film and with larger diameters because the tendency for phase stratification is greater. Also, it would seem the presence of inlet conditions like the 180^0 bend preceding the test section in the experiments of Lis & Strickland,[6] Robertson[7] and Fisher & Yu,[9] positively affected the presence of dryout due to stratification taking place just downstream of the bend. Though the effect of pressure, diameter and heat flux is believed to show qualitatively in those experiments, it would be desirable to evaluate the effect of these variables in a system where the inlet effects do not play a role.

Most recently a study of this sort was conducted by Ruder, Bar-Cohen, and Griffith.[12] This work focused on the low and moderate quality dryouts and presented the results in the context of Taitel & Dukler flow regime maps. This work was limited to one inch pipes operating at atmospheric pressure for heat flux less than 100 kW/m^2. However, the test section was 6m long, so in contrast to the other work, the effect of an inlet bend was removed. In this way, the effects producing dryout could be

evaluated without the additional factor of entrance effects. Ruder[5] found that there exists two separate dryout zones associated with low quality (stratified flow) and moderate quality (intermittent flow). Criteria were developed for each of these dryout limits and these will be discussed separately here.

2.2.1. Low quality dryout limit

In the work of Ruder et. al., the criterion for the low quality dryout limit was established by examining the stability of stratified flow. Essentially, stratified flow was treated as a stationary bubble that required a minimum liquid velocity in order to convect it downstream. The analysis of Benjamin[13] for the *Benjamin bubble* gives a critical value for the approach velocity of the liquid upstream of the stationary bubble:

$$V = 0.542\sqrt{gD} \tag{2-4}$$

where V is the upstream liquid velocity which can be taken as the superficial liquid velocity, j_l. Then the Froude number limit is:

$$Fr_l = 0.542 \tag{2-5}$$

Given the assumptions employed in deriving this limit, the operational limit was taken as:

$$Fr_l = 1 \tag{2-6}$$

Above this limit, the flow is intermittent or bubbly. A further limit was put forth for low quality if the flow system contained entrance effects such as bends or fittings or diameter changes. This operational limit is given by:

$$Fr_l = 2 \tag{2-7}$$

This later bound is not justified in any way and appears to be based on using a safety factor of two.

2.2.2. Moderate quality dryout limit

When operating in certain parts of the intermittent or slug flow regime, Ruder[14] found that the pipe could run anisothermally; that is, moderate quality dryout was found to be a subset of the slug flow regime. It was observed that a small band of qualities where isothermal operation prevailed separated the low and moderate quality zones.

Using an approach similar to Fisher & Yu,[9] Ruder calculates the thermal bound for this regime by balancing the time to dry out the post-slug film with the slug period. He considers the effects of film drainage and evaporation, but assuming an initial thickness of the post-slug film to be $\delta_0 = 50\ \mu m$, he concludes that the contribution of drainage is small and considers evaporation only. The slug frequency was calculated from a correlation given by Gregory & Scott[15] for adiabatic air-water flow in small diameter pipes. Equating evaporation time with the slug period gives a locus of points along which impending dryout occurs:

$$gD(j_l + j_g)\left[\frac{q''}{0.0226 h_{fg}\rho_l\delta_0}\right]^{0.833} = j_l^2(j_l + j_g) + j_l j_g(j_l + j_g) + 19.75 j_l \qquad (2\text{-}8)$$

This locus takes the form of a dome on a superficial velocity map that has a maximum liquid velocity which is due to the fact that the slug frequency has a minimum at a particular gas velocity. This maximum is of chief concern because it defines the minimum allowable flow rate to avoid dryout. The peak of the locus is given by Ruder to be,

$$Fr_l = 3.2\times10^4\sqrt{D}\left[\frac{q''}{\rho_l h_{fg}}\right]^{0.833} \qquad (2\text{-}9)$$

where all quantities are in mks units. This thermal bound peak depends almost linearly with heat flux (or more precisely on the evaporation rate) as might be expected.

The dryout regions determined by Ruder based on top-bottom temperature differences show a domelike region on a superficial velocity map in the region of intermittent flow. However, the peak of the dome does not have the expected dependence on heat flux, actually *decreasing* slightly with heat flux. So, for high heat flux the model overpredicts the dryout bound. The reason was not resolved but was suspected to be the shortcomings of the *adiabatic* slug frequency correlation for diabatic conditions. Ruder et. al. hypothesized that there was frequency enhancement for increasing heat flux but this was not confirmed by experiment nor theory. Nevertheless, $Fr_l = 1$ bounded both the low and moderate quality data at atmospheric pressure.

The two bounding criteria scale differently with system properties and is worth noting. The low quality bound ($Fr_l = 1$) is strictly kinematic and the liquid rate necessary scales as the square root of the pipe diameter. The moderate quality bound depends on heat flux and fluid properties as well as scaling *linearly* with diameter. This would imply that moderate quality dryout would be most prevalent for large diameters operating at high pressure and heat flux.

As specific recommendations, Ruder stated that the pipe should run isothermally if the lower of two bounds is exceeded; the intermittent dryout limit peak (given in equation 2-9) or the intersection between the bound for the bubbly-slug transition and the slug-annular transition (see flow regime map, Figure 2.4). This later bound defines

whether slug flow will in fact be encountered. If it is not, then the thermal bound is meaningless. In addition, the $Fr_l = 1$ bound should always be exceeded unless inlet effects due to fittings are suspected, in which case $Fr_l = 2$ is appropriate. Finally, Ruder notes that a tube inclination exceeding 2^0 (upward) is sufficient to remove the dryout region for mass flux greater than 73 kg/m^2s ($U_{l_0} = 0.076m/s$).

The preceding literature review was intended to give an overview of previous work on flow regimes and dryout in horizontal pipes. Literature on more specific subject areas within this envelope will be discussed as needed at the appropriate point later in the text.

CHAPTER 3

Experimental Apparatus and Methodology

The proper design and fabrication of the experimental rig for this study of intermittent and high quality dryout required consideration of the parametric range of interest. The limitations of power and physical space available dictate that no single version of a test rig can cover the whole range of operating conditions. Therefore, the basic apparatus was designed around intermittent flow dryout but was left adaptable for other studies. The basic apparatus will be described in detail here and changes to the rig explained as needed.

3.1. Design Parameters

As mentioned previously, the industrially important range of diameter for steam generating tubes is one - two inch. Ruder[5] has studied the smaller size and the effect of increased diameter was studied here to expand the data base and to check the predictions of Ruder. Many steam generating and heat transfer components employ very high heat fluxes, so the system was designed for the maximum value physically obtainable for a reasonable sized system. A nominal operating value for FBC's is 50,000 Btu/hr–ft^2 (158 kW/m^2). For the available 45 kW power supply, this

corresponds to a system length of about 63 inches. The design procedure is simplified and the system is more flexible for alteration if designed to run at atmospheric pressure. Also, at the low pressure, flow regime visualization is possible with the use of transparent viewing ports.

Clearly, to study intermittent dryout, the proper range of quality and flow rate must be produced by the pump in conjunction with the heating system. The predictions of Ruder[5] are a useful starting point. The peak of the thermal bounding curve is given by:[5]

$$j_l = 3.2x10^4\sqrt{g}\, D\left[\frac{q''}{\rho_l h_{fg}}\right]^{0.833} \tag{3-1}$$

So, for a heat flux of 158 kW/m^2 (50,000 Btu/hr–ft^2) the minimum superficial liquid velocity required to exceed the dryout limit for a two-inch pipe is 2 m/s or 65 gpm of single phase liquid. The quality range is below about 5%. This quality is unobtainable for high liquid rates using only the available power supply, so preheating or direct steam injection was required and incorporated into the design. The calculated pressure drop under these conditions, using standard two-phase methods and approximate system length of 20 ft is about 10 psi. A non-positive displacement pump fulfilling these needs was chosen.

3.1.1. System Hardware

With these considerations, the horizontal flow test rig was designed, fabricated, and is schematically shown in Figure 3.1. The closed flow loop begins in the holding tank which acts as a reservoir and steam-water separator. The slightly subcooled liquid is pumped with an 80 gpm, 20 psi impeller pump, controlled with main and by-

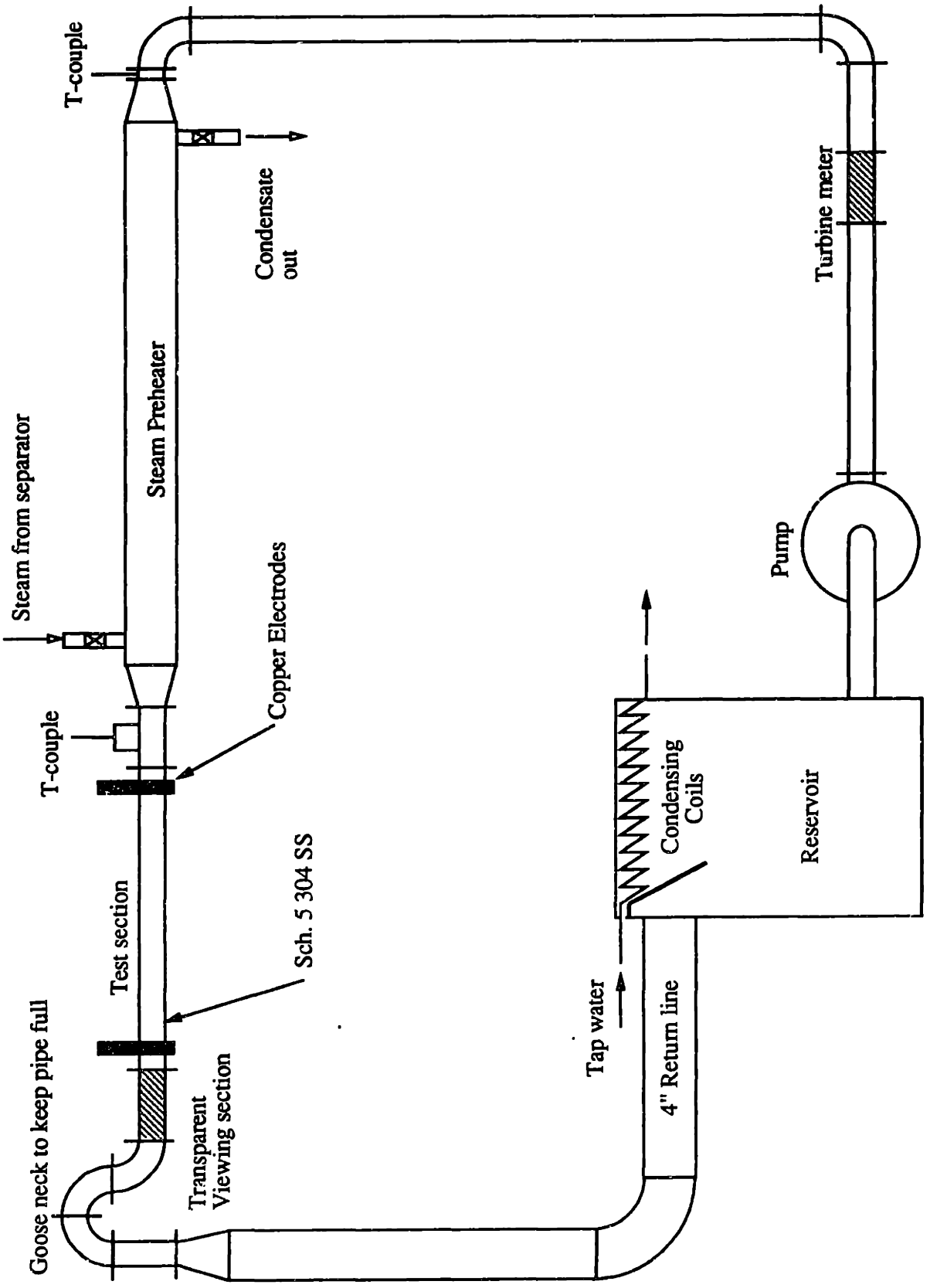

Figure 3.1: Sketch of the atmospheric pressure rig with two-inch test section

pass globe valves and measured with a 1½ inch stainless steel turbine meter manufactured by Hoffer flow controls (model HO11) having a linear range between 6 and 93 gpm. The flow enters the single tube-in-shell condensing preheater to achieve a two-phase state before entering the test section. The steam source was high quality 60 psi steam which was separated to give saturated steam into the preheater.

The thin walled (schedule 5) stainless steel test section has an overall length of 80 inches. Stainless steel was chosen to withstand extreme temperatures due to continuous dryout and to minimize corrosion. The wall thickness was chosen to produce the optimal electrical resistance to achieve maximum power dissipation from the 45 kW, 3000 A, DC generators. A secondary benefit is the rapid thermal response of the 0.065 inch thick wall. As a result, much of the temperature history information is not filtered out by the pipe capacitance and can be used for statistical analysis.

A sight glass at the outlet allows for visual observation of the flow regime. The goose neck following prevents a sudden stratification of the flow which would occur had the outlet dropped vertically. It also simulates the upflow serpentine tube which is typical of heat exchangers of this type. Four-inch diameter pipe was used thereafter to minimize the two-phase pressure drop. Within the holding tank, there are four 25 foot lengths of 3/8 in. copper tube using tap water to condense the produced steam.

With the exception of the test section, all the piping is copper to minimize corrosion. Type K thermocouples were inserted as shown but only the preheater inlet thermocouple was used routinely to measure the degree of subcooling.

None of the system was insulated, except for small regions over each test section thermocouple. The overall heat loss was calculated to be about 6% and could be reliably accounted for or neglected. The benefit of achieving a rapid and reliable steady-state upon changing thermal or hydrodynamic conditions outweighed the loss of accuracy in the heat balance. A heat balance check of the condensing preheater confirmed that the temperature rise of single phase liquid through the flow loop was balanced by the collected condensate within 2%.

3.1.2. Instrumentation

For the determination of the thermal state, the test section was instrumented with 19 thermocouple sets. For most experiments, only ten sets were used to increase the data sampling rate. An example of a thermocouple set assembly is shown schematically in Figure 3.2. The unsheathed type K thermocouples were held tight against the pipe with a thermally conducting, electrically insulating cement in between. The Omega Thermcoat CC cement was essential to isolate the thermocouple from the electric potential present in the metal pipe. To insure thermal equilibrium with the pipe, a two inch square of 1 inch thick quartz wool covered each thermocouple and the whole assembly was held on with two 2 inch x 2 inch curved aluminum sheets and a hose clamp.

Nineteen such assemblies were fabricated and put on the system at four inch intervals. The thermocouple sets were wired differentially at terminal connectors located near the pipe. Extension grade thermocouple wire brought the signal to the data acquisition board.

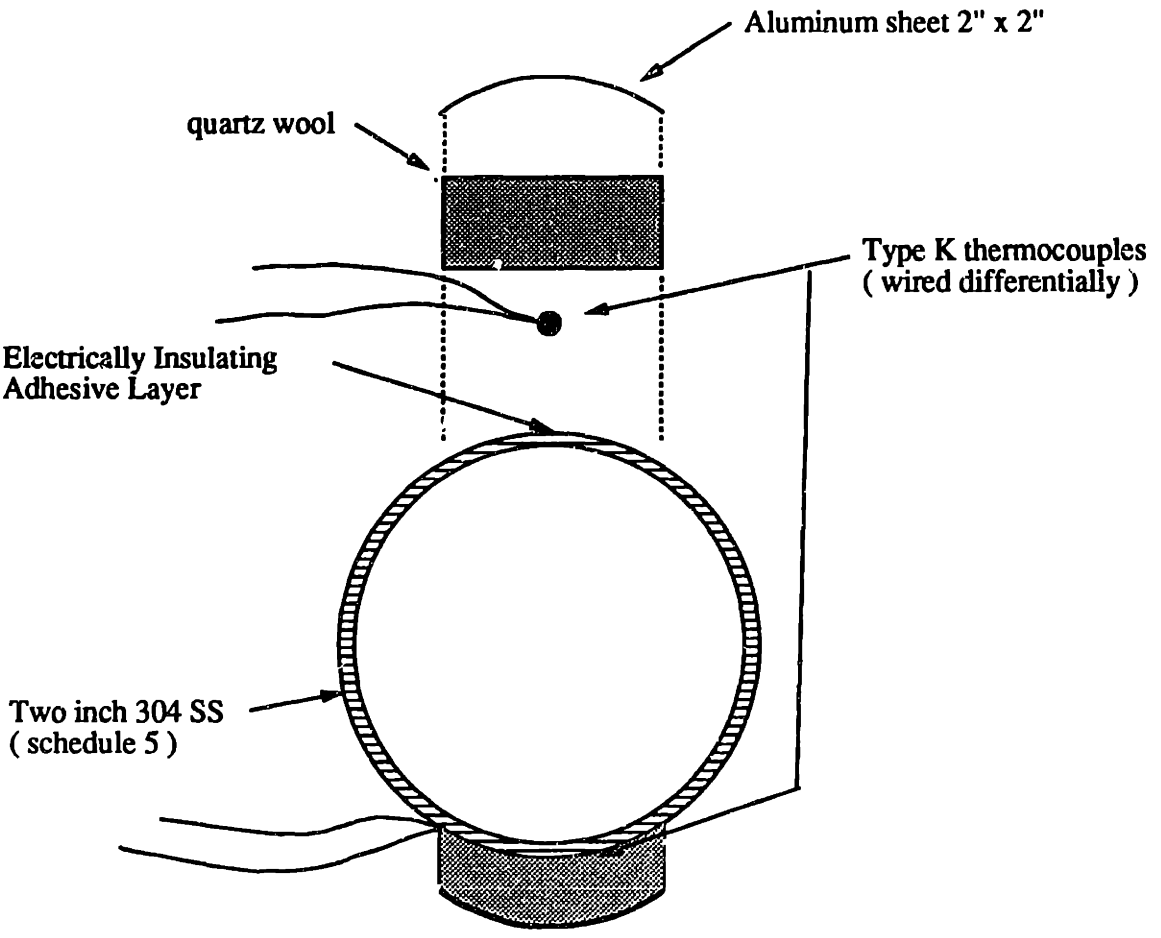

Figure 3.2: Sketch of differential thermocouple assembly

Ten of the differential thermocouples (at eight inch spacings) were input to a Metrabyte EXP-16 multiplexer board. This board employed a gain of 1000 and was connected to the computer's DASH-16F board. An IBM-AT computer using Labtech Notebook version 4.3 was used for the data acquisition. With ten differential inputs, the computer could sample each at 15 Hz which was believed to be sufficient to resolve the system thermal frequency.

Finally, the test section current was measured from a calibrated shunt on the power controller which gives a voltage proportional to system current. Wires connected to each end of the test section allowed simple voltage measurement with a digital voltmeter to compute the power input.

3.2. Experimental Methodology

The experimental goal of the project was to construct an operational map delineating regions of (un)acceptable operation. The mapping chosen was in superficial velocity coordinates for its convenience and because of its utility in delineating regimes in two-phase flow. To parameterize heat flux, a map is required for each heat loading tested. Then for each test, j_{l_o} was found through the flow rate. The quality, x(z) was calculated from a heat balance. Ten map points result, corresponding to each thermocouple location with its accompanying thermal state.

The determination of dryout using external temperature information is not straightforward and somewhat arbitrary. Ruder[5] used the difference in the steady-state averaged temperature between top and bottom as the criterion. Since the bottom is always wet in horizontal flow, a positive difference of $\Delta T=T_t-T_b$ exceeding some

threshold indicates dryout, although he is not clear what threshold was used or how to justify it. This method has its share of difficulties. First, there exists imprecision in all thermocouples and although typically rather small, manufacturer specifications do not boast great precision on standard thermocouples. For type K thermocouples, the uncertainty band increases with temperature but is $\pm 2^0$F at best. In the differential mode then, the accuracy is $\pm 4^0$F. Conceivably, two differential sets reading the same state could give a result $8\Delta^0$F different in the worst case. To deal with this, one would have to accept a large threshold to reliably conclude anything about the thermal state. Secondly, there are channel to channel variations in the multiplexer board which are not specified but believed to be of order one-two degrees.

Another issue concerns the interpretation of a steady state temperature differential. One cannot assume that a positive ΔT, no matter how small, is an indication of *impending* dryout. If no dryout is present in slug flow, the time averaged heat transfer coefficient at the tube top has contributions from a boiling/convection h, as the slug passes, weighted with a film evaporation h as the bubble passes. Along the bottom, only the boiling/convection h applies. Since the heat transfer coefficient for the evaporating film is substantially higher, the average h, under pre-dryout conditions, is higher on top leading to a lower average wall temperature under uniform flux conditions. So, with dryout impending in the slug flow regime, it can be shown that $\Delta T = T_t - T_b$ is actually negative. Use of a positive ΔT threshold to show the incipience of slug flow dryout is likely to either: misinterpret the flow regime, or indicate only those dryout conditions that are extreme enough.

A solution to these dilemmas is proposed here. If one preserves all of the temperature history information, i.e. $\Delta T(t)$, and analyzes this data without regard for a baseline temperature, the thermocouple errors noted above are reduced substantially. In effect, the absolute ΔT is ignored and the assessment is made from the fluctuations of ΔT. Clearly, the set to set variations due to thermocouple imprecision and multiplexer channel imprecision are cancelled out and the only uncertainty arises from differing thermocouple response constants, which are certainly within a few percent.

Since the whole temperature history is saved, statistical analysis and thresholding can be done in any number of ways, e.g. average ΔT, maximum ΔT, maximum slope dT/dt, or maximum range of ΔT, defined as ΔT_{fluc}. This was the parameter used in this work. With this measure, the actual problem associated with slug flow dryout can be seen; the fluctuation of pipe temperature with time.

This approach of course will not average the ever present noise in the thermocouple signal as time averaging will. However, using the maximum range of ΔT, the effect of noise is added and choosing an appropriate value for the fluctuation threshold will embody this effect. The criterion for ΔT_{fluc} was chosen after analysis of the data. All thermocouple sets had fluctuations of ΔT and the choice of a threshold was based upon capturing contiguous regions of dryout points, thus filtering out points where the fluctuation of temperature was insignificant. This method will be discussed further in the next chapter.

3.3. Experimental Procedure

After the system had achieved operating temperature, the flow and heating conditions were set. Typically, the heat flux and preheater steam rate were maintained constant and flow was changed from a maximum and lowered in increments. Possible damage to the system defined the lower limit of flows studied. Steady state was achieved within a few minutes when the flow rate and test section current were stable. For each run, data was taken on all channels for two minutes. It was found that this time was sufficient to capture the full envelope of temperature fluctuations on any set. During this time, the single phase liquid flow rate and steam condensate volume flow were measured, as well as the inlet temperature and test section current and voltage.

3.4. Analysis of Data

For each run, the T(t) data was smoothed to minimize the effect of noise using a five point nearest neighbor averaging technique which gave effective smoothing while not "filtering" the signal drastically. The average single phase velocity U_{l_o} was found from the flow rate in gpm and the quality, x(z) was found from equilibrium thermodynamic relations. The superficial velocities, for mapping purposes, were found from the following relations:

$$U_v = \left[\frac{\rho_l}{\rho_v}\right] x U_{l_o} \tag{3-2}$$

$$U_l = U_{l_o} - \left[\frac{\rho_v}{\rho_l}\right] U_v \tag{3-3}$$

The flow rate of liquid and the inlet quality were the input parameters used for each run at a given heat flux. These were varied to fill out the dryout map over the

operating range of interest. The next chapter presents the data for the four heat fluxes tested.

CHAPTER 4

Intermittent Dryout Results

4.1. Description of Thermal Bounding Map

Using the previously described experimental procedure, thermal bounding maps were constructed at four different heat fluxes up to 146 kW/m^2 (46,000 $Btu/hr-ft^2$) corresponding to maximum available power. The results are shown in Figures 4.1 - 4.4. Each velocity - quality pair (or j_l,j_g) is mapped with the corresponding thermal state. The Taitel & Dukler flow regime boundaries[1] are shown for reference. Typically, the data points appear in groups of 10 corresponding to the ten thermocouple locations. Since the map is on log-log coordinates, the points lie closer together for increasing quality. Mapping the entire region required changing the test section inlet quality at a given flow. Sometimes points overlapped where the mass flow and quality were identical but where a differing inlet quality was employed. The range covered was dictated by power and pumping constraints as well as provision for enough mass flow to prevent damage to the test section.

In general, four states have been distinguished. The plus signs represent points where dryout does not occur. The solid squares are where it is believed dryout

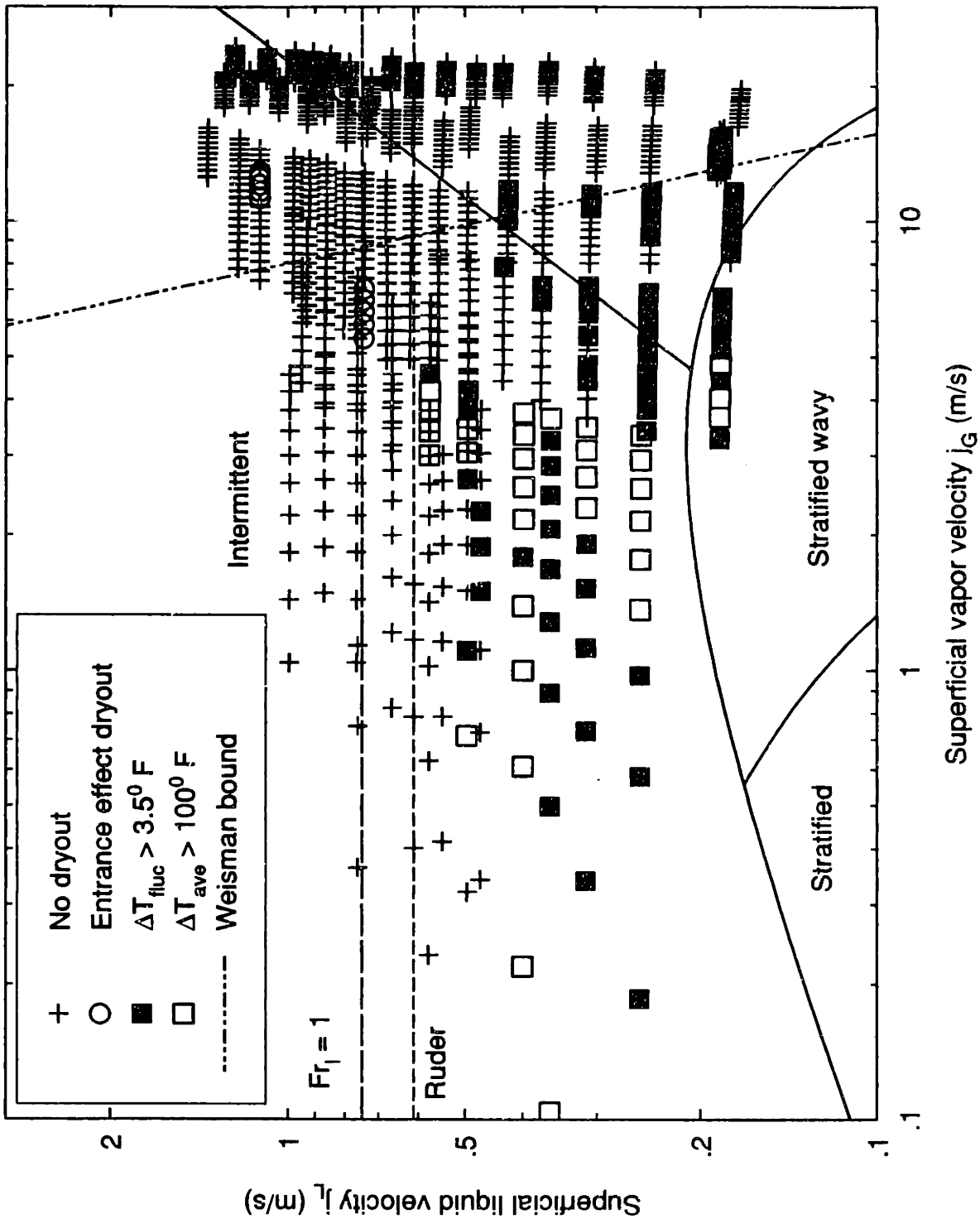

Figure 4.1: Dryout map for q'' = 37 kW/m^2

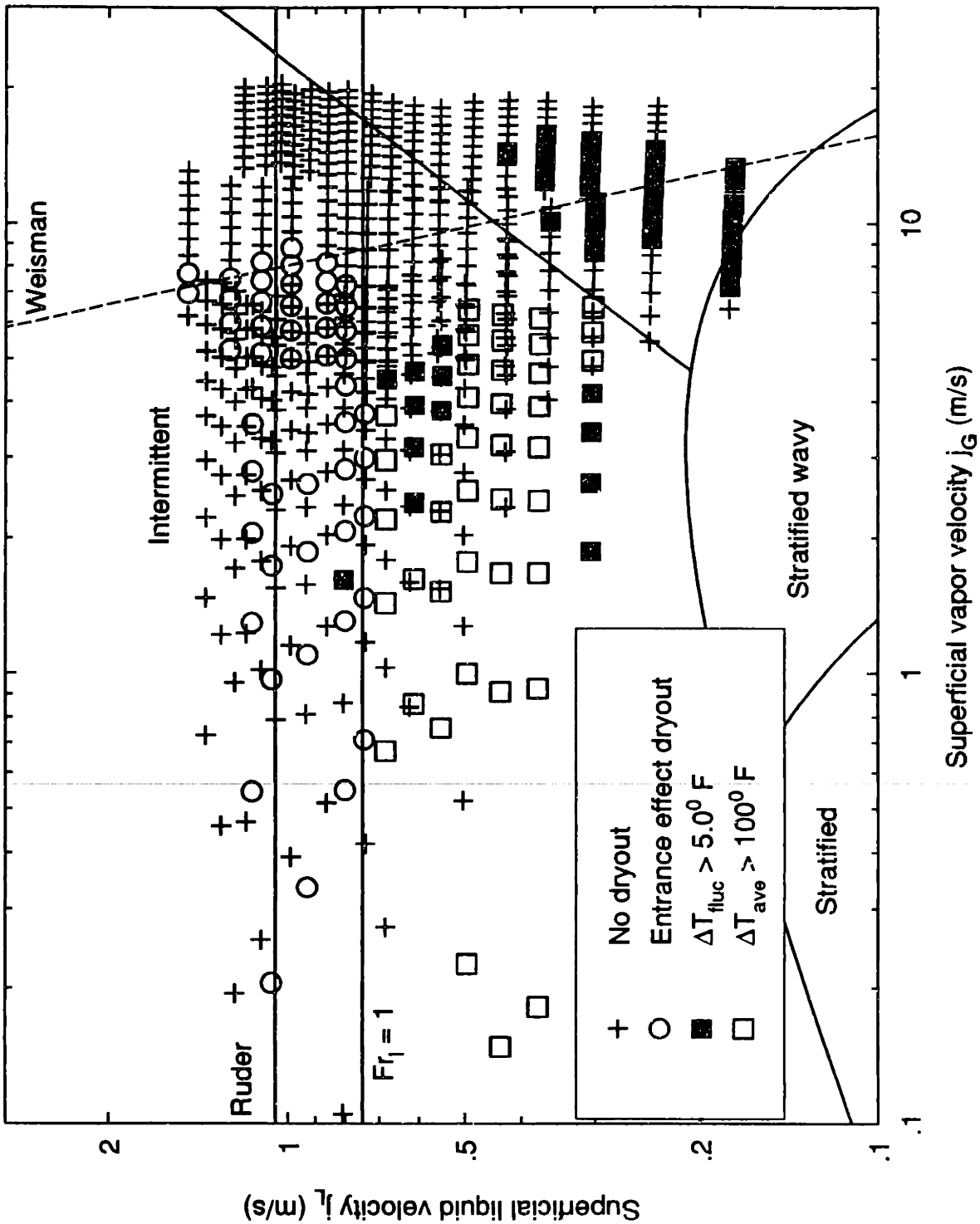

Figure 4.2: Dryout map for q'' = 71 kW/m^2

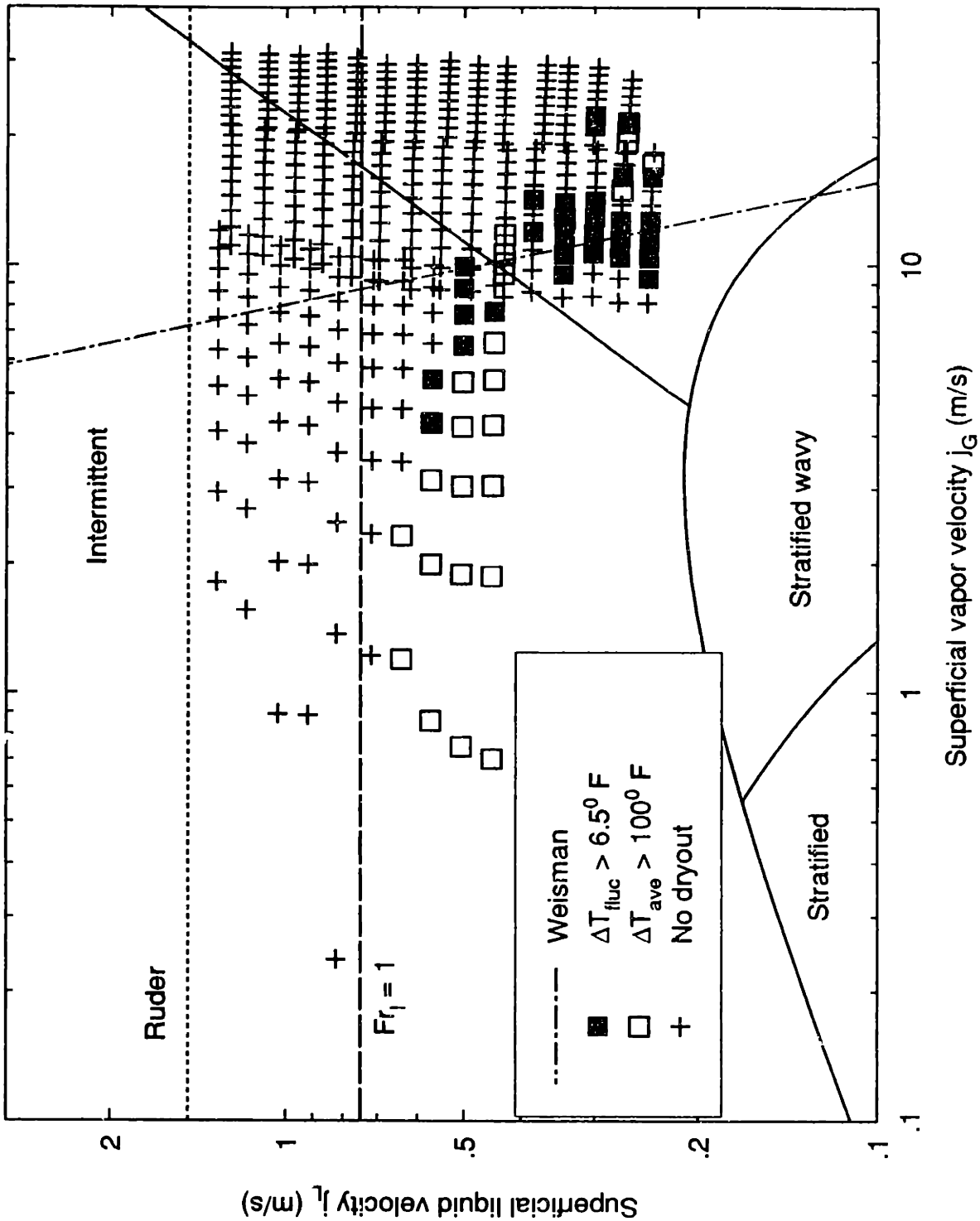

Figure 4.3: Dryout map for q'' = 106 kW/m^2

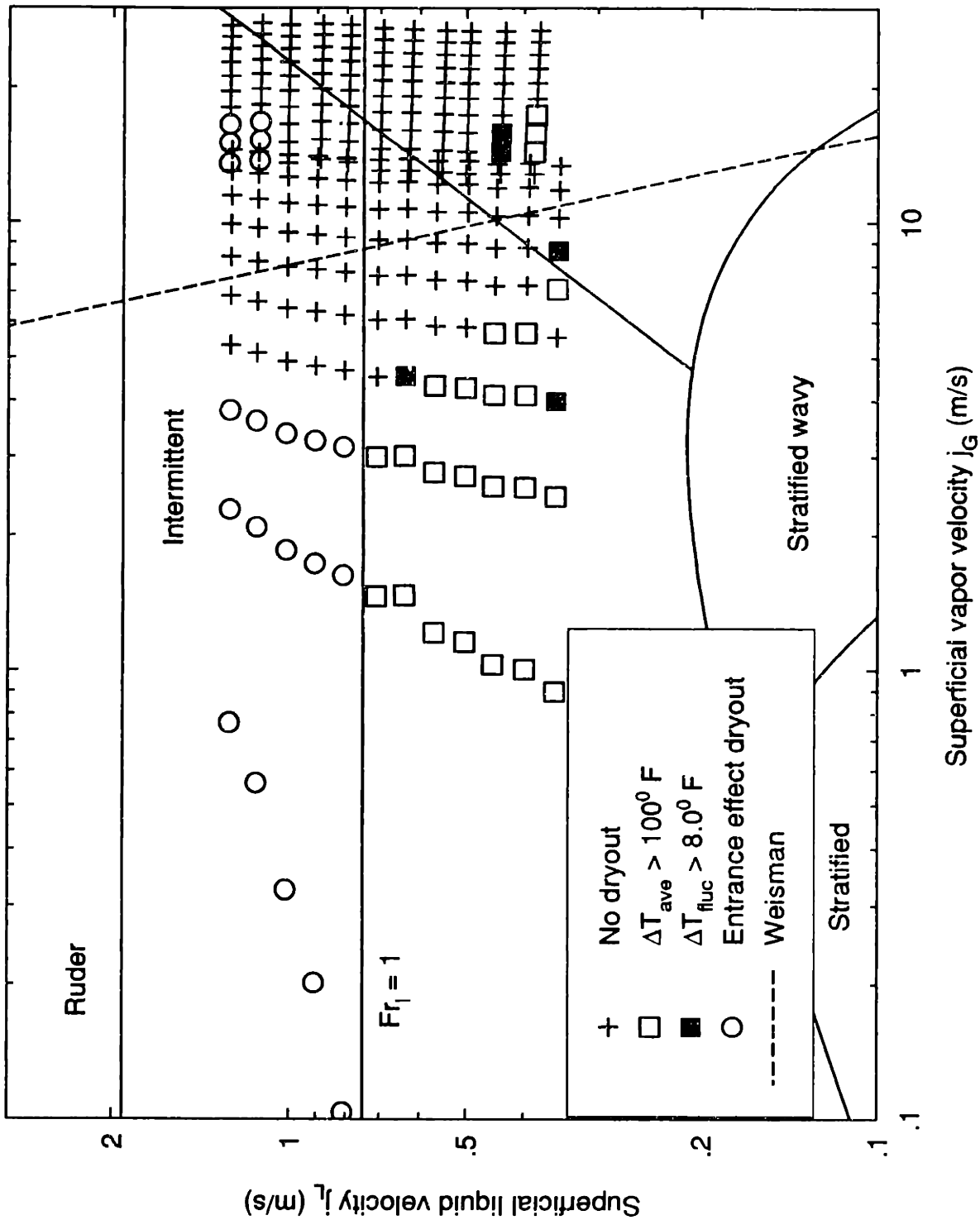

Figure 4.4: Dryout map for q'' = 146 kW/m^2

resulting from flow stratification occurs. The criterion for these points is that the time averaged temperature difference from top to bottom (ΔT_{ave}) exceeds 100^0F. Although somewhat arbitrary, it is clear to sustain a temperature difference of this magnitude, the rewetting of the tube must be so infrequent, that the the flow is effectively stratified. No information about temperature fluctuations was used for these points.

The solid squares are points where it is believed *intermittent* dryout is occurring. Though ΔT_{ave} is small or often negative the magnitude of the total fluctuation in ΔT exceeds a threshold. Because the periodicity of the slug flow produces a varying heat transfer coefficient at the top of the tube, one would expect temperature fluctuations in all cases of intermittent flow. However, the presence of a transient dry wall would be expected to increase the amplitude of this fluctuation. Thus, the onset of intermittent flow dryout is inferred when ΔT_{fluc} exceeds the defined threshold value. The threshold was chosen to be a minimum value that left a contiguous region of map points. This threshold value was scaled linearly with heat flux because the temperature oscillation amplitude will scale linearly with heat flux to first order, all else constant. Thus, to detect the *onset of dryout* , the amplitude of oscillation (ΔT_{fluc}) should scale with heat flux. A more critical assessment of the choice of temperature threshold was explored with two specific approaches. First, the temperature oscillations were predicted by simulating the transient heat conduction problem in the pipe wall. Second, the effect on the dryout region of changing the threshold value was explored. The results of these studies are given in Appendixes A & B.

The fourth type of state is shown by the open circles which indicate dryout resulting from an adverse condition at the test section inlet. They are characterized by a

large ΔT_{ave} ($\Delta T_{ave} > 100^0F$), but occur at mass velocities that are too large to be explained by a simple Froude number argument for stratified flow. This will be discussed in more detail later. In addition to the flow regime boundaries, the $Fr_l = 1$ line is given, as well as the peak value of Ruder's[14] semi-analytic boundary and the Weisman onset of annular flow bound.[3]

4.2. Discussion of Results

The stratified operational limit has been given[12] by $Fr_l = 1$ or in this case $j_l = 0.75$m/s. Referring to Figure 4.1, the stratified or high ΔT dryout occurs for qualities less than about 1% and for j_l less than about 0.7 m/s which supports the use of this operational limit. Though the fluctuation in ΔT is substantial, the large ΔT is indicative of an essentially dry wall.

For qualities between about 1% and 3% and below j_l of about 0.5 m/s exists the intermittent dryout region (also referred to as the *dome).* The peak of this dome is of chief concern and lies at about 0.45 m/s. For this relatively low heat flux, this peak, or the minimum superficial liquid velocity ($j_{l_{min}}$) to avoid dryout is less than the limit given by low quality or stratified dryout. These points lie in the region of the annular flow transitions given by Taitel & Dukler[1] and by Weisman.[3] At the lowest heat flux, the Weisman onset line coincides well with the termination of the intermittent dryout region.

The remaining maps (Figures 4.2-4.4) indicate the same basic structure. The low quality dryout region appears in approximately the same location. The liquid limit for this region varies somewhat but is always less than Fr_l=1. The peak of the intermittent

dome is nearly constant at about 0.45 m/s and less than both the low quality dryout limit, and the Ruder peak. For increasing heat flux, the intermittent points move slightly to the right to higher qualities, encroaching on the Weisman boundary for annular flow onset[5] as shown on the maps.

It should be noted that there is a region between the stratified and intermittent dryout regions where the tube is wet. Because ΔT_{ave} is smaller, the flow is no longer stratified but the slug flow apparently has not developed to the point where dryout results. Also the termination of the dome on the right side does not imply the termination of slug flow. The flow was verified at the test section exit to be intermittent in these runs, so the termination of the intermittent dryout precedes the termination of slug flow. Clearly, the intermittent dryout region is a subset of the slug flow region.

Based on the extrapolation of Ruder's model, the slug flow peak was expected to be the limiting dryout boundary for two-inch pipe at these heat fluxes. This result confirms Ruder's observation that the semi-analytic thermal bound is conservative particularly at high heat flux and requires some refinement. Because the low quality bound also bounds the intermittent region, slug flow dryout takes on diminished importance.

The dryout points toward the upper part of the map which have an associated high ΔT could not at first be explained, because the mass flux is too large to support a stable stratified flow. It was observed that the physical location of all these points was near the pipe inlet extending in some cases down the entire pipe length. It was noted that there was a 1/4 inch step *increase* in diameter at the junction of preheater and test section (See Figure 3.1) which was perhaps a sufficient disturbance to separate phases.

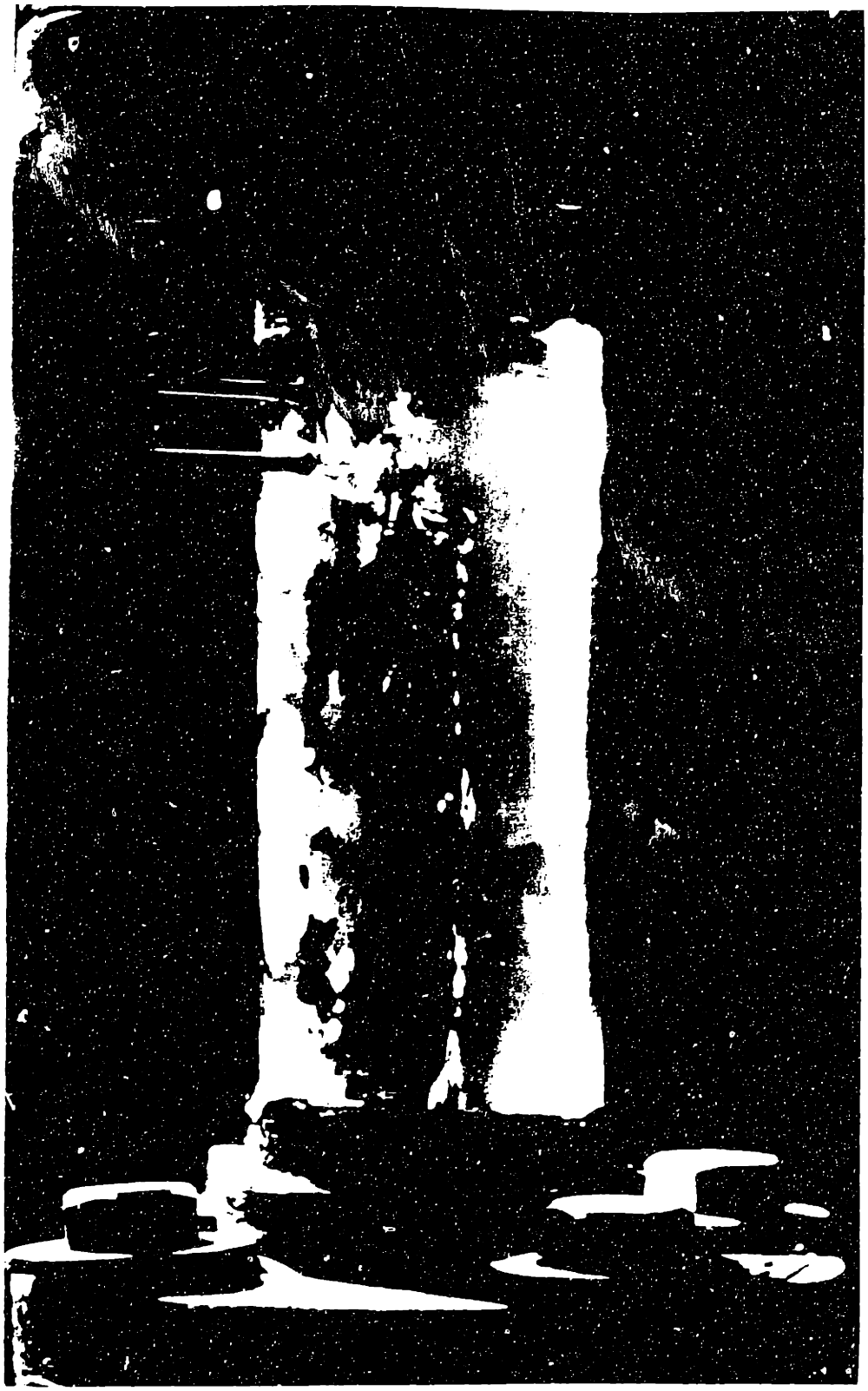

Figure 4.5: Photograph of stationary vapor pocket. Flow is from left to right

To visualize the problem, a short transparent pipe section having the same ID as the test section, was inserted between the preheater and test section. When the system was run at high single phase velocities near the saturation temperature, it was found that the flow stratified such that a long vapor pocket trailed off the junction and into the test section. Figure 4.5 shows a photograph of such a pocket. The flow, with $Fr_l > 1$, is from left to right. The appearance of condensate on the upper half of the lexan tube indicates that an extended time period has elapsed since the surface was wetted. The observation of this vapor pocket confirms the cause of the unexpected dryout. The vapor pocket was relatively stable, but could not be systematically reproduced. This is consistent with the fact that not all the maps show this type of state. An important conclusion to draw is that the fabrication details of a piping system can have a marked impact on the local thermal behavior.

For such inlet effects, Ruder[5] recommended a limit of $Fr_l = 2$. This entrance dryout was experienced at flows approaching, but not exceeding this limit, so the merit of this recommendation cannot be evaluated. The next chapter attempts to modify the present prediction for intermittent flow.

CHAPTER 5

Modeling of Intermittent Dryout

5.1. Introduction

Understanding the physics behind intermittent flow dryout is essential to construct predictive models useful to designers for ensuring steam generating tube life. Essentially no detailed models for dryout with industrially important pipe parameters have been constructed. Typically, liquid mass flux is kept at a level well above that which gives detrimental pipe behavior. However, since pumping power is proportional to the cube of the flow rate, one must not be too liberal in the choice of minimum mass flux.

First attempts at physically based models have been made principally by Ruder[5] and Coney.[11] The approach of both researchers is essentially the same but disagreement arises in the emphasis of important dryout components. Essentially, slug flow is treated as a periodic phenomena and the characteristic period is balanced with the time to dryout based on the combined effects of the relevant mechanisms. Ruder considers two effects tending to remove liquid from the wall, namely the post-slug liquid film drainage down the tube wall and evaporation of this film driven by the imposed heat flux. These effects are considered as acting separately, but as will be shown are

coupled. The total contribution due to drainage was shown to be small compared to evaporation and was neglected. However, a needed parameter in the analysis, the initial value of the post-slug film thickness, was taken from Fisher & Yu[9] to be 50μm and appears to be quite dubious. It will be shown that the initial film thickness is quite different but, in fact, does not strongly influence the problem if large values are assumed. Ruder then balances the time to evaporate the film with an empirically determined slug frequency correlation for fully developed, adiabatic slug flow. This bounding model has been shown in the data of Chapter 4 to be very conservative with respect to the present data and thus his model is being analyzed.

The work of Coney[11] is certainly more detailed but was not presented within the context of dryout data. An in-depth fluid mechanical analysis is given where emphasis is placed on the initial post-slug film thickness and the inertial effects in the falling film. Heating is incorporated in the model, but the simulation results are compared solely with adiabatic drainage data.

The foregoing analysis will show that the added complexity to account for axial momentum of the film, inertial effects in the falling film and precise determination of the initial film thickness are not justified for the time scales important in this problem. Therefore, a simpler model is adopted incorporating drainage, evaporation, and measured slug frequencies for both adiabatic and diabatic flow in a pipe of typical (not necessarily fully-developed) length. The effects of bubbles in the film are discussed.

5.2. Intermittent dryout model

The model put forth basically considers film drainage, evaporation, and bubble nucleation within the film as effects that remove liquid from the wall as a bubble passes (between slugs) and the slugging (or rewetting) frequency acts as a restoring force. Dryout occurs if these depletion effects succeed during the time interval that the bubble requires to pass the given point. The mechanisms will be discussed separately.

5.2.1. Evaporation

Consider a liquid layer left after a slug passes a point with thickness δ_0 as shown in Figure 5.1. The mass removal by change of phase is given by thermodynamic considerations. The rate of film loss is:

$$\frac{d\delta}{dt} = \frac{-q''}{\rho_l h_{fg}} \tag{5-1}$$

This encompasses vaporization at the free surface and formation of bubbles within the film at the wall. The secondary effects of these bubbles will be discussed in section 5.2.3.

5.2.2. Drainage

Solving the drainage characteristics of the liquid film shown in the sketch requires solution of the momentum equation. The following assumptions are employed:

- The film is thin, i.e. $\delta/R \ll 1$, so that streamwise coordinates can be used.
- Surface tension effects exist, but are negligible.
- The flow is 2-D; axial momentum is unimportant; $\frac{\partial}{\partial z} = 0$.

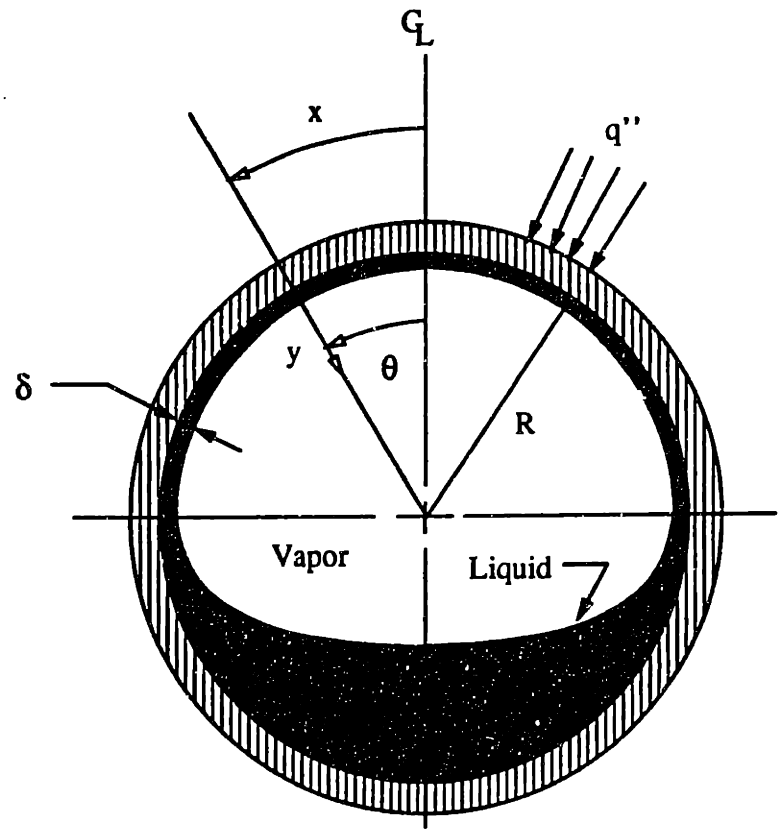

Figure 5.1: Sketch of pipe cross section with draining film

- There is symmetry about the vertical centerline.
- The moving vapor produces negligible effect on the film.
- The bubble is isobaric.

Using these assumptions, the momentum equation is:

$$\frac{\partial u}{\partial t} + u\frac{\partial u}{\partial x} + v\frac{\partial u}{\partial y} = g_x + \nu_l\left[\frac{\partial^2 u}{\partial y^2} + \frac{\partial^2 u}{\partial x^2}\right] \tag{5-2}$$

subject to the no-slip condition,

$$u(x,0,t) = v(x,o,t) = 0, \tag{5.2-a}$$

the zero shear condition,

$$\frac{\partial u}{\partial y}(x,\delta,t) = 0, \tag{5.2-b}$$

and the initial condition:

$$u(x,y,0) = v(x,y,0) = 0 \tag{5.2-c}$$

This governing equation can be simplified by checking the time scale for inertially dominated flow. Far from the wall (large y), the fluid immediately undergoes free fall. To an order of magnitude, the time duration for free fall is:

$$\tau_{inert} \simeq \sqrt{2R/g} \tag{5-3}$$

which is on order of 0.1 sec. Compared to the periodic time scale of the slug flow (several seconds), this is small. Only liquid that is within the developing boundary layer (near the wall) is not subject to free fall. The thickness of the boundary layer is approximately given by:

$$\delta_{bl} \simeq 4\sqrt{\nu_l t} \tag{5-4}$$

or about 1.0 mm for water at room temperature or 0.6 mm at T = 212^{0}F. This thickness, by definition of the boundary layer, is affected by viscous forces and although

inertia is not necessarily small, will be neglected for thicknesses less than calculated by equation 5-4. By a length scale argument, it can be shown that

$$\frac{\partial^2 u}{\partial y^2} \gg \frac{\partial^2 u}{\partial x^2}$$

Then, the momentum equation reduces to:

$$g_x + \nu_l \frac{\partial^2 u}{\partial y^2} = 0 \tag{5-5}$$

subject to:

$$u(x,0) = 0 \tag{5.5-a}$$

$$\frac{\partial u}{\partial y}(x,\delta) = 0 \tag{5.5-b}$$

where $g_x = g\sin\theta$ using the coordinate system shown in Figure 5.1. Solution of this equation at any θ is given by:

$$u(y) = \frac{g\sin\theta}{\nu_l}\left(\delta y - \frac{y^2}{2}\right) \tag{5-6}$$

The magnitude of u (the tangential velocity) is a function of θ,y and δ. To find the thickness over time, the film continuity equation is introduced:

$$\frac{\partial \delta}{\partial t} + \frac{1}{R}\frac{\partial}{\partial \theta}\int_0^{\delta} u(y)dy = 0 \tag{5-7}$$

Substitution of equation 5-6 into equation 5-7 gives:

$$\frac{\partial \delta}{\partial t} + \frac{g}{\nu_l R}\left(\delta^2 \sin\theta \frac{\partial \delta}{\partial \theta} + \frac{\delta^3 \cos\theta}{3}\right) \tag{5-8}$$

subject to the initial condition,

$$\delta(0) = \delta_0, \tag{5.8-a}$$

and the symmetry condition at the tube top:

$$\frac{\partial}{\partial\theta} = 0 \qquad \text{(5.8-b)}$$

Solution of the above PDE can be done numerically, however in the context of this work, the location where the film is thinnest is most important. If one looks at the tube top ($\theta = 0$) where the film will be thinnest, equation 5-8 becomes:

$$\frac{d\delta}{dt} + \frac{g\delta^3}{3\nu_l R} = 0 \qquad \text{(5-9)}$$

with the same initial condition. The solution is given by:

$$\delta = \left[\frac{2gt}{3\nu_l R} + \frac{1}{\delta_0^2} \right]^{-1/2} \qquad \text{(5-10)}$$

Several observations about the above can be made. The thickness is asymptotic to zero as is the rate of thinning. Also, as the value of the initial thickness is increased, the contribution to the thickness for long times diminishes; initially the film thins very rapidly. Realistically, the velocity is limited by the free fall speed. The solution for various values of δ_0 are exactly the same except that the time between each solution is offset. Thinner initial films simply have a "head start" but evolve through the same thickness history.

If one considers only the tube top, an evolution equation can be obtained with the combined effect of heating and drainage. This has been considered in the work of Gardner[16] The thickness rate of change due to evaporation and drainage are additive yielding:

$$\frac{d\delta}{dt} = \frac{-q''}{\rho_l h_{fg}} - \frac{g\delta^3}{3\nu_l R} \qquad \text{(5-11)}$$

subject to the initial condition. The solution $t(\delta)$ is[17]

$$t = \frac{-\alpha}{3a}\left[\frac{1}{2}\ln\left(\frac{(\delta+\alpha)^2}{\delta^2-\alpha\delta+\alpha^2}\right) + \sqrt{3}\,\mathrm{Arctan}\left(\frac{2\delta-\alpha}{\alpha\sqrt{3}}\right)\right]_{\delta_0}^{\delta} \qquad (5\text{-}12)$$

where

$$\alpha = \left(\frac{3q''\nu_l R}{\rho_l g h_{fg}}\right)^{1/3}, \quad a = \frac{q''}{\rho_l h_{fg}} \qquad (5.12\text{-a,b})$$

To obtain δ explicitly as a function of time, it was necessary to invert the coordinates numerically. Use of this evolution equation will be discussed subsequently.

5.2.2.1. General solution

It is important to know the uniformity of thickness along θ to know how large an expected dry patch might be. This requires numerical solution of the PDE (equation 5-8). Defining

$$\hat{\delta} = \delta/R$$

$$\hat{t} = \frac{gRt}{\nu_l},$$

the non-dimensional form of equation 5-8 is:

$$\frac{\partial\hat{\delta}}{\partial\hat{t}} + \hat{\delta}^2\sin\theta\frac{\partial\hat{\delta}}{\partial\theta} + \frac{\hat{\delta}^3\cos\theta}{3} = 0 \qquad (5\text{-}13)$$

with

$$\hat{\delta}(0) = \hat{\delta}_0 \qquad (5.13\text{-a})$$

and

$$\frac{\partial\hat{\delta}}{\partial\theta}(0) = 0 \qquad (5.13\text{-b})$$

Equation 5-13 was solved using an explicit finite difference scheme. The initial film thickness was assumed to be uniform at a value of $\hat{\delta}_0 = 0.1$ corresponding to

approximately 2.8 mm. The results of the numerical simulation can be used to check for film profiles along θ and compare to adiabatic thickness measurement traces. For the diabatic case, it was simply necessary to subtract from the thickness at all θ, a value corresponding to the imposed heat flux, i.e

$$\Delta\hat{\delta} = \frac{q''\nu_l}{\rho_l h_{fg} g R^2}\Delta\hat{t} \tag{5-14}$$

Using this more general formulation allows for solving the film thickness field in the case of circumferentially non-uniform heat flux which is encountered for example, in FBC's.

The numerical drainage curve was compared to equation 5-10 for the case of no heating (at the top) to verify accuracy of the scheme and are in fact indistinguishable when plotted together. In addition, conservation of mass was verified using the numerical scheme.

5.2.2.2. Measurement of film drainage

To test the physical result for the drainage evolution derived in the previous section, the thickness-time characteristics were measured experimentally. For this comparison, it was sufficient to carry out the measurement using an air-water, two component flow at room temperature. The same system used for the thermal experiments was plumbed for the addition of air by substituting a tee for the 90^0 elbow before the preheater (see Figure 3.1). The stainless steel test section was replaced with a two inch ID clear PVC pipe. The air rate was measured using a standard ASME orifice meter.[18]

Several techniques are available to measure thickness of liquid films over time. The most popular of these is the use of a flush conductance probe which is described by Hewitt.[19] A schematic of the measuring probe is shown in Figure 5.2. Essentially, the film bridging the two electrodes acts as a linear resistor dependent on film thickness, so the current passed under a constant voltage is an indication of thickness. The probe was fabricated by drilling two 0.125 inch diameter holes into the PVC tube wall ½ inch apart along the tube axis. Conducting probes were inserted into the flow conduit and glued. The inner surface was abrasively machined to insure flushness that is essential to prevent the probe from interfering with the flow and for measurement accuracy.

It is preferable to measure voltage rather than conductance, so a circuit was constructed for this purpose. The accompanying (simplified) circuit is shown in Fig. 5.3. Simple circuit theory will show that the voltage across the reference resistor is linearly related to the film thickness up to some limit, which depends directly on the probe spacing. A tradeoff exists between the degree of localization and the extent of linearity. For this geometry and size, the probe response is linear up to about 2 mm. Beyond about 2 mm, the response becomes non-linear and saturates; the conductance remaining constant with increasing thickness. In principle, one could use a circuit equation to extract the film thickness from a measured voltage. However, this requires an accurate knowledge of the fluid conductivity and source voltage. Instead, the probe can be calibrated continuously with a reference probe. The reference probe consisted of two flat, non-conducting plates separated by shims of known thickness which contained the metallic probes arranged in the same geometry. Fluid continuously flowed

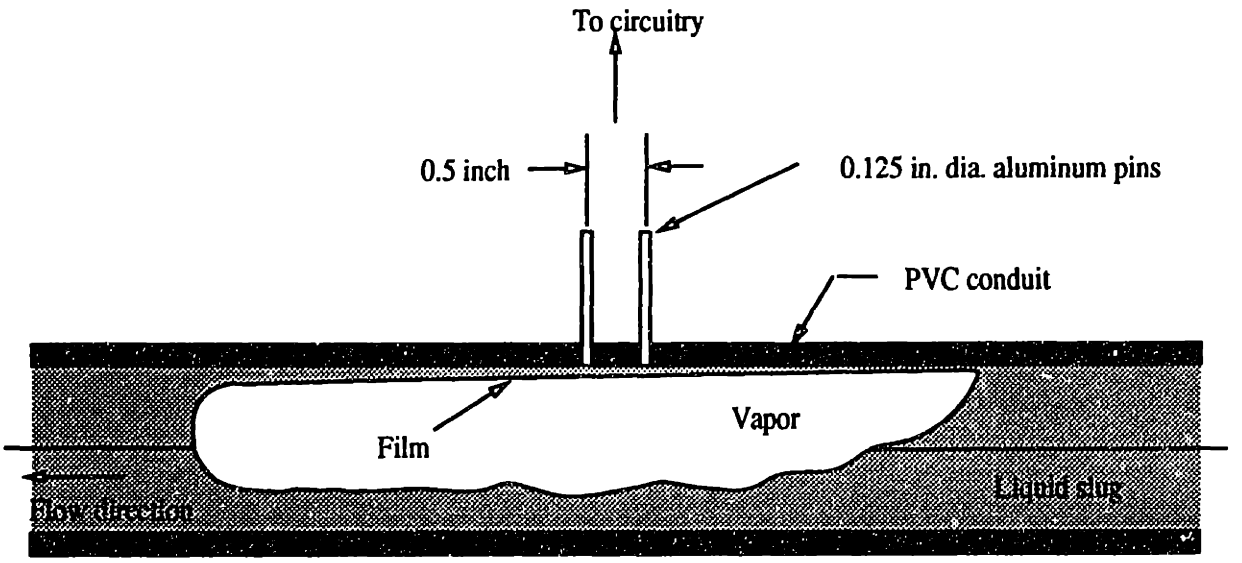

Figure 5.2: Sectional view of flush conductance thickness probe

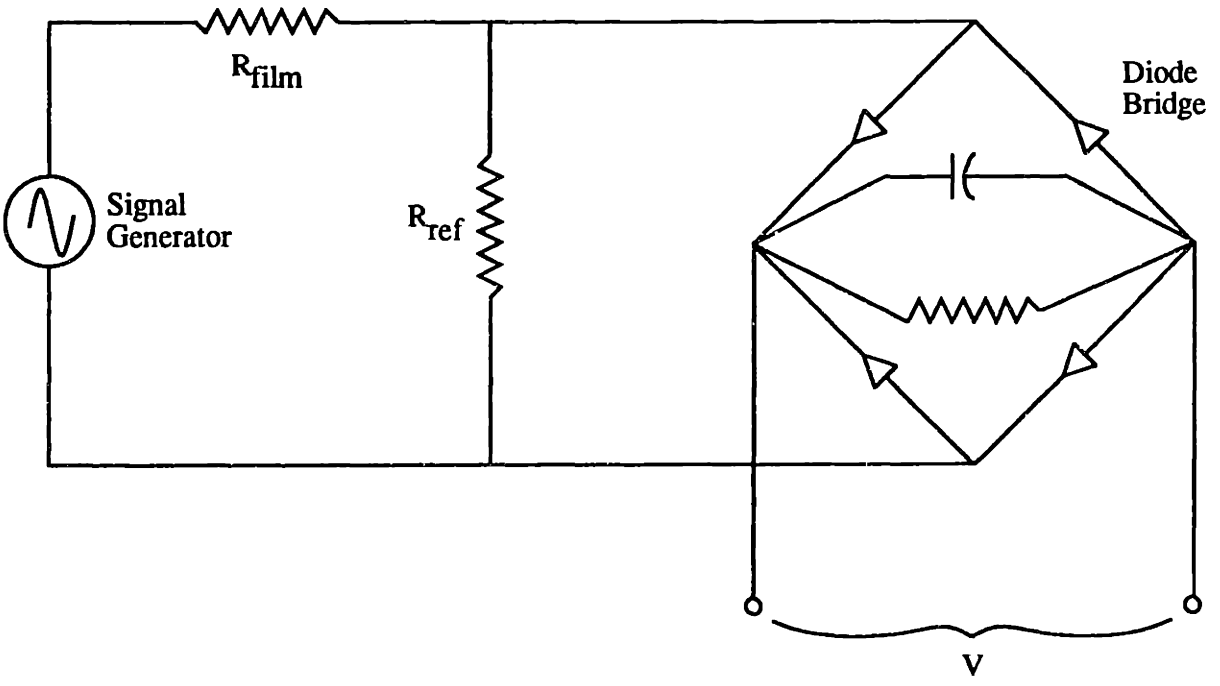

Figure 5.3: Circuit used to measure thickness of draining film

from the system into the reference probe which gave an essentially constant output voltage from the reference resistor when the circuit was connected. The thickness of the draining film, up to the linear limit is then found from:

$$\delta = \left[\frac{V}{V_{ref}} \right] \delta_{ref} \tag{5-15}$$

For the purposes of data analysis, the output from across the reference resistor was input to the data acquisition system.

5.2.2.3. Results of the film measurement

Sampling at a relatively low frequency of 10 Hz allowed recording of the gross behavior of slug flow. Shown in Fig 5.4 is a ten second trace of voltage vs. time. As seen, the voltage plateaus during probe saturation as a slug is passing. Next is a rapid fall-off during free fall of the film followed by a knee and a slow decay toward zero. The cycle then repeats as another slug passes. It is clear that this data is useful for the purposes of slug counting and will be discussed again in a subsequent section on slug frequency measurements.

A more detailed look at the characteristics of drainage requires a higher sampling rate. Using a 100 Hz data rate, drainage curves were recorded. For these measurements, it was also necessary to switch the circuit to the reference film branch and record the voltage for the sampled fluid. Using the calibration procedure previously described, a typical drainage curve of thickness vs. time is shown in Fig 5.5.

The trace saturates at about 2 mm. So, the initial film left after slug passage, is at least 2 mm thick. The film thickness rapidly falls for about 0.05 seconds until

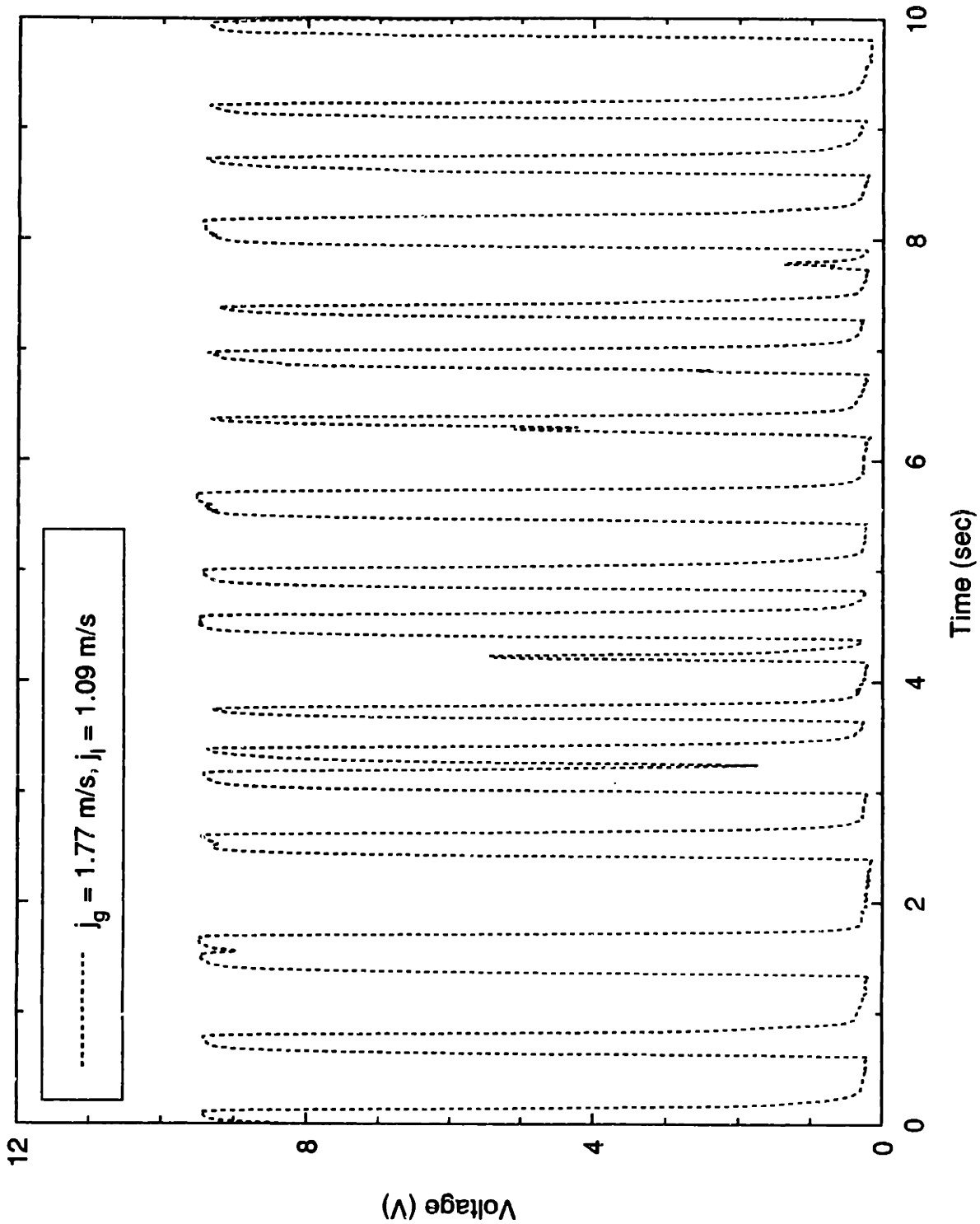

Figure 5.4: Voltage - time response from conductance probe in slug flow

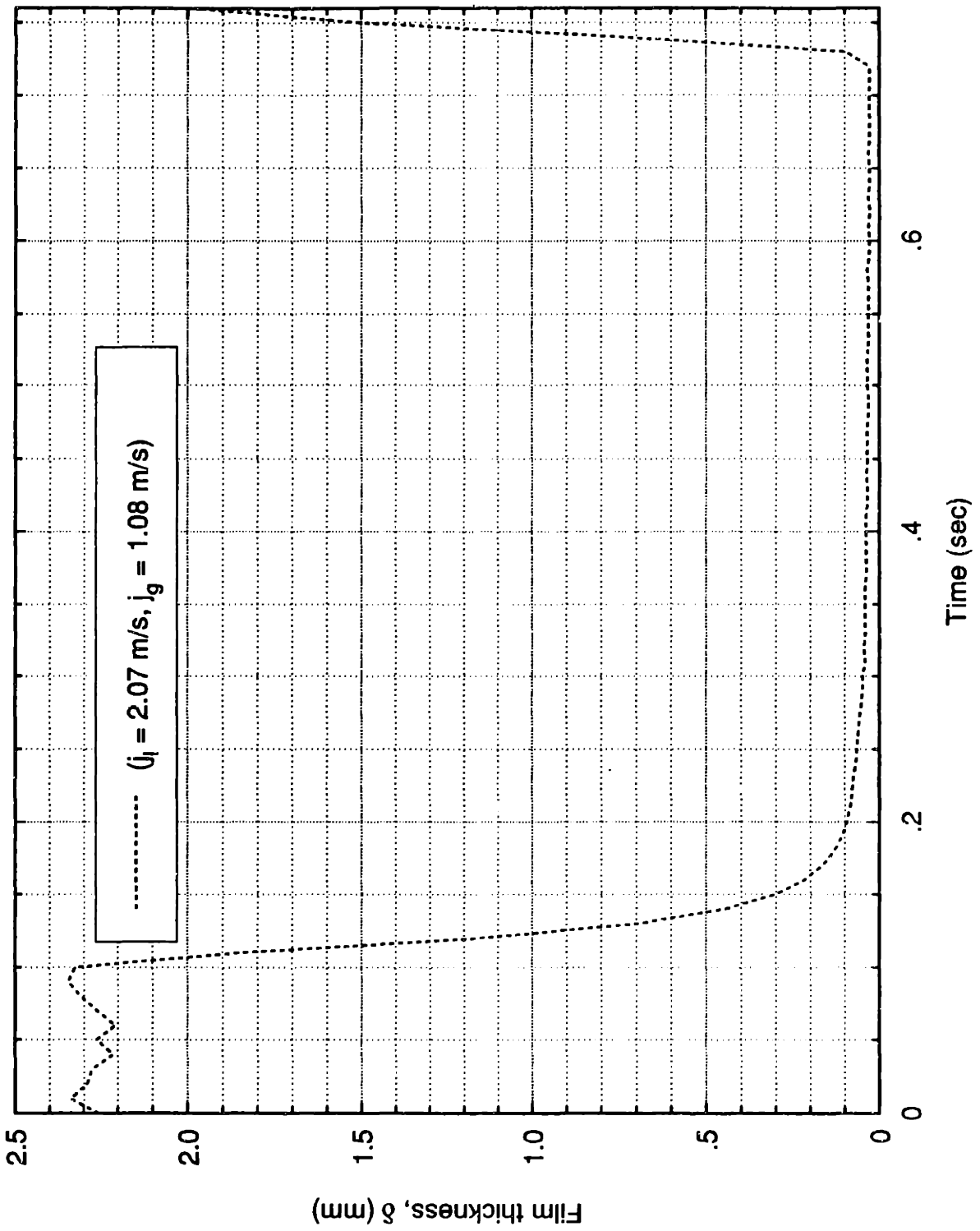

Figure 5.5: Film thickness data vs. time at the tube top

draining slows substantially at the knee. Finally, the thinning is very slow on the tail of the curve approaching a value of about 0.03 mm before another slug passes. These drainage results are quite typical and did not appear to depend on the specific slug flow conditions.

5.2.2.4. Comparison of data and model

To compare the analytical model to the drainage data, the program used to generate numerical data was altered to allow offsetting the time axis in conjunction with the chosen initial film thickness condition so that both curves "start" at the same place. The starting point was chosen as the termination of the free fall regime.

The approximate time to free fall was calculated to be 0.2 seconds. This compares well with the time that the knee is encountered. Because the thinning rate drops dramatically there, it is expected that viscous forces are beginning to affect the entire thickness of the film remaining. Equation 5-4 gives this thickness as

$$\delta_{bl} \simeq 4\sqrt{\nu_l t} \simeq 1.0 \text{ mm} \qquad (5\text{-}16)$$

As seen, this is slightly thicker than expected but the free fall time calculation was only approximate. Using this initial thickness and the proper time offset, the corresponding traces for a measurement at $\theta = 45^0$ are shown in Figure 5.6. The agreement is very good initially; the curves track together very well. However, as the low asymptote is entered, the curves diverge and over the full range of asymptote, there is about a factor of two discrepancy in the thickness shown by the model and data. On the plot, two starting points for the model are used: one corresponding to the calculated starting point and one at a very thick value. It is clear that the two will

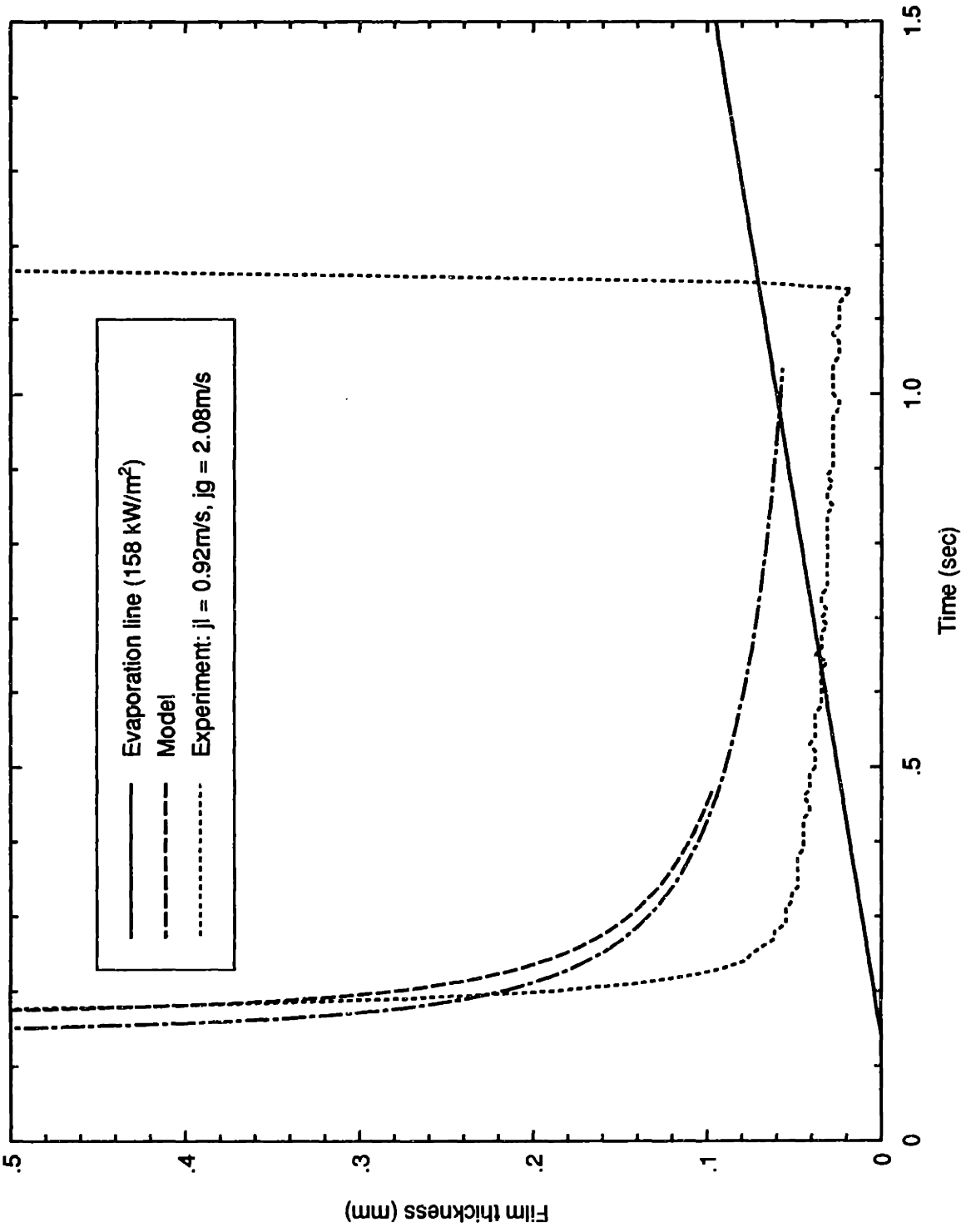

Figure 5.6: Film thickness 45^0 from tube top after slug passage

converge, so the exact starting thickness is unimportant if large. Other thickness traces were checked and the data is typically a factor of two to three thinner than the model prediction.

Though the discrepancy is large on a percentage basis, the absolute thickness difference is less than 0.05 mm. To appreciate what this means in a dryout study, the effect of heating should be included. On Figure 5.6, a straight line is shown from the time that drainage begins with slope dictated by the heat flux level. This, termed an evaporation line, represents the thickness loss over time of the film due to the imposed heat flux. Assuming the drainage and evaporation components to act independently (not strictly true), the point of intersection of the heating line and drainage curve(s) gives the time at which dryout is expected. As seen, a small discrepancy in thickness gives a large difference in dryout time. Particularly troublesome in this case, is that the thickness data is always less than the model's prediction. Had this been reversed, the discrepancy could be absorbed into a safety factor and the model safely used in practice. A discussion of this difference follows.

5.2.2.5. Discussion of physical model

The shortcomings of the model was the initial focus in explaining the discrepancy between the experiment and theory. Among the possible issues are omission of the inertial terms, turbulence in the flow, surface tension effects, interfacial shear on the film, and the presence of surface waves.

To discuss the first two, a calculation of the film Reynolds number is in order.

$$Re = \frac{4\Gamma_\theta}{\nu_l} = \frac{4}{\nu_l}\int_0^\delta u dy \,, \tag{5-17}$$

which for the calculated velocity profile is

$$Re = \frac{4g\delta^3 \sin\theta}{3\nu_l^2} \tag{5-18}$$

At the tube side, Re vs. time as calculated from the simulated data, is shown in Fig 5.7. Clearly, the initial Reynolds number is large supporting the fact that inertial terms are important early on. In fact, Reynolds numbers greater than about 2000 imply turbulence. However, for the regime of interest, i.e., thin films, Re is small; the flow collapses to a gravity-driven viscous flow. Attempts at comparing the model and data only for long times, that is using an initial condition corresponding to a very thin layer, were not fruitful. No matter where the simulation is started on the experimental trace, divergence occurs immediately leading to the same magnitude of error. To strengthen this argument, solution of the momentum equation including the temporal acceleration was performed. The results and discussion of this is given in Appendix C.

Turbulence must exist in the film early after slug passage; for that matter it is turbulent when actually part of the slug's boundary layer. A turbulent film has a much larger effective viscosity than its laminar counterpart. However, larger viscosity, even if it were to persist as the film thins, would not allow explanation of a film that is actually *thinner* than predicted. The sign of the error is wrong. Furthermore, at low Re, it must be that the film re-laminarizes and viscosity dominates.

Other issues in the modeling concern the possible effects of surface tension in the film, shear induced by the gas phase, or waves on the surface. If the film remains

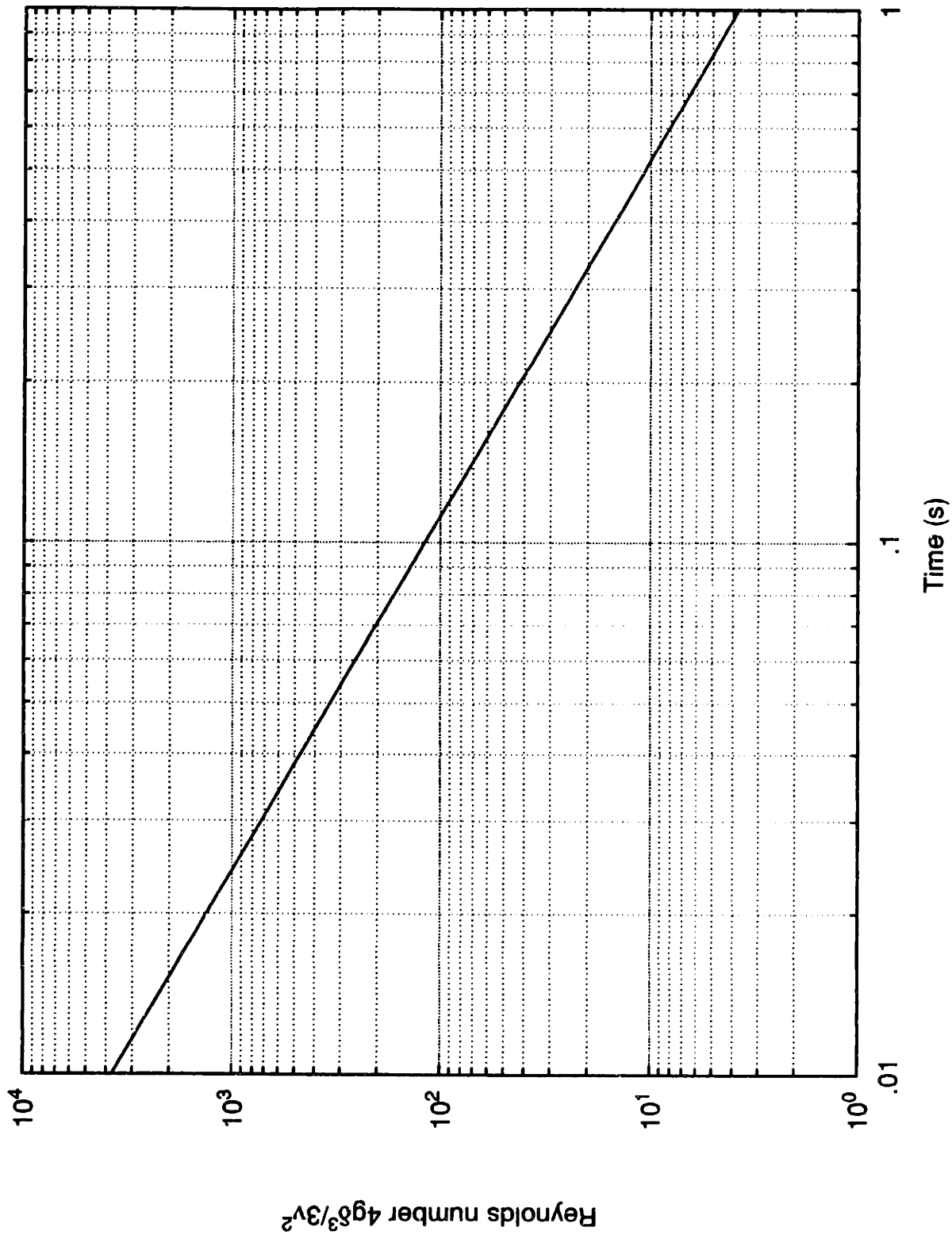

Figure 5.7: Film Reynolds number vs. time after slug passage

continuous, surface tension cannot be a strong force because the film curvature is small, unless there is a surface tension gradient. There is little basis for saying that a surface tension gradient exits so this was dismissed. The vapor velocities in slug flow are quite small so the effects of shear on the film are considered too small to have a measurable impact. Waves, however do exist on any flowing free surface film and the effect of these may not effect the modeling as much as interpretation of the measurement.

The thickness measurement with the flush conductance probe is not truly local. The ability of the probe to give an effective thickness depends on whether the current lines can conform well to the fluid's irregular surface. Coney[10] discusses this problem. Clearly if the probe spacing is much less than the wavelength of the surface irregularity, then it won't be a problem. If not, then there will be some error. Generally, the probe will underestimate the thickness since the current may not "see" the peaks of the liquid surface.

Thickness measurements were also made with a probe scaled down in length by a factor of four such that the spacing was 0.125 inch. Unfortunately, the results were identical with the 0.5 inch probes; the measured thickness is about half of that predicted. The discrepancy has not been explained but perhaps very short wavelength disturbances are responsible for biasing the measurement.

5.2.3. Bubble nucleation

At the relatively high heat fluxes in question here, it is not known whether all phase change takes place at the film surface, i.e. evaporation, or whether some takes

the form of growing bubbles at the heated wall. In the latter case, the effects on film depletion are not known. Several effects may include a) liquid loss due to droplet entrainment into the vapor when bubbles burst, b) de-wetting due to surface tension if the bubble bursts and forms a true discontinuity in the film, c) resistance to the drainage process since the bubbles may be considered as obstacles, d) Displacement of the surrounding film as bubble growth proceeds, thereby increasing the local film thickness, *enhancing* drainage.

5.2.3.1. Prediction of bubble nucleation

To determine if bubble nucleation is in fact occurring, it is necessary to determine the wall superheat at a given heat flux. This requires knowledge of the inside heat transfer coefficient. Using a calculated heat transfer coefficient, if the wall superheat exceeds the incipient wall superheat required for nucleation at the given heat flux, then nucleation occurs. The approach used here employs a heat transfer coefficient for vertical falling films. Although not a vertical geometry, one would expect the essential physics to be the same. Shmerler and Mudawar[20] have proposed the following for a vertical free falling film:

$$h = 0.0038\left[\frac{k_l g^{1/3}}{\nu_l^{2/3}}\right] Re^{0.35} Pr_l^{0.95} \tag{5-19}$$

for the Reynolds number range ($6000 < Re < 25000$), where the Reynolds number is defined as $Re = 4\Gamma_\theta/\nu_l$ and Γ_θ is the film flow rate. Then,

$$Re = \frac{4g\delta^3 \sin\theta}{3\nu_l^2} \tag{5-18}$$

For $\sin\theta = 1$, a plot of Re vs. t using the numerically calculated $\delta(t)$ is given in Fig

5.8. Also shown is the heat transfer coefficient and the conduction coefficient k/δ. As seen, k/δ exceeds the convective coefficient almost immediately after the initial fall of the film. Clearly, for smaller θ this will be more pronounced since Re is smaller and the film is thinner. The ability to suppress nucleate boiling by film conduction only, will depend on the heat transfer coefficient and the incipient wall superheat. Marsh & Mudawar[21] have correlated the incipience condition for vertical falling films. It is a modification of the standard pool boiling correlation given by:

$$q_i = \frac{1}{3.5}\frac{k_l h_{fg}}{8\sigma T_{sat} v_{fg}}(T_{wi} - T_{sat})^2 \qquad (5\text{-}20)$$

where the 3.5 is a factor that accounts for turbulent eddies in the film and waviness of the surface. For example, if $q_i = 146$ kW/m^2, $\Delta T_i = 9.8^0$C, the minimum k/δ is shown on the plot. So, one would conclude that nucleation in the film will be suppressed after 0.6 seconds under atmospheric conditions.

5.2.3.2. Experimental visualization of bubble nucleation

The above gives an estimate of the time frame during which nucleation occurs. However, the possible effects on the film dryout are not so easily deduced. To get a qualitative view of these effects, nucleation within the film was visualized experimentally.

Since the flow hydrodynamics and heat transfer characteristics are essentially the same for a film flow on the inside or outside of a curved conduit, an experiment was built to study the film flow on the outside of a two inch pipe. A one foot sample of the same pipe used for the test section was connected to the DC power source (in series with the test section) with provision made for a continuous shower of water

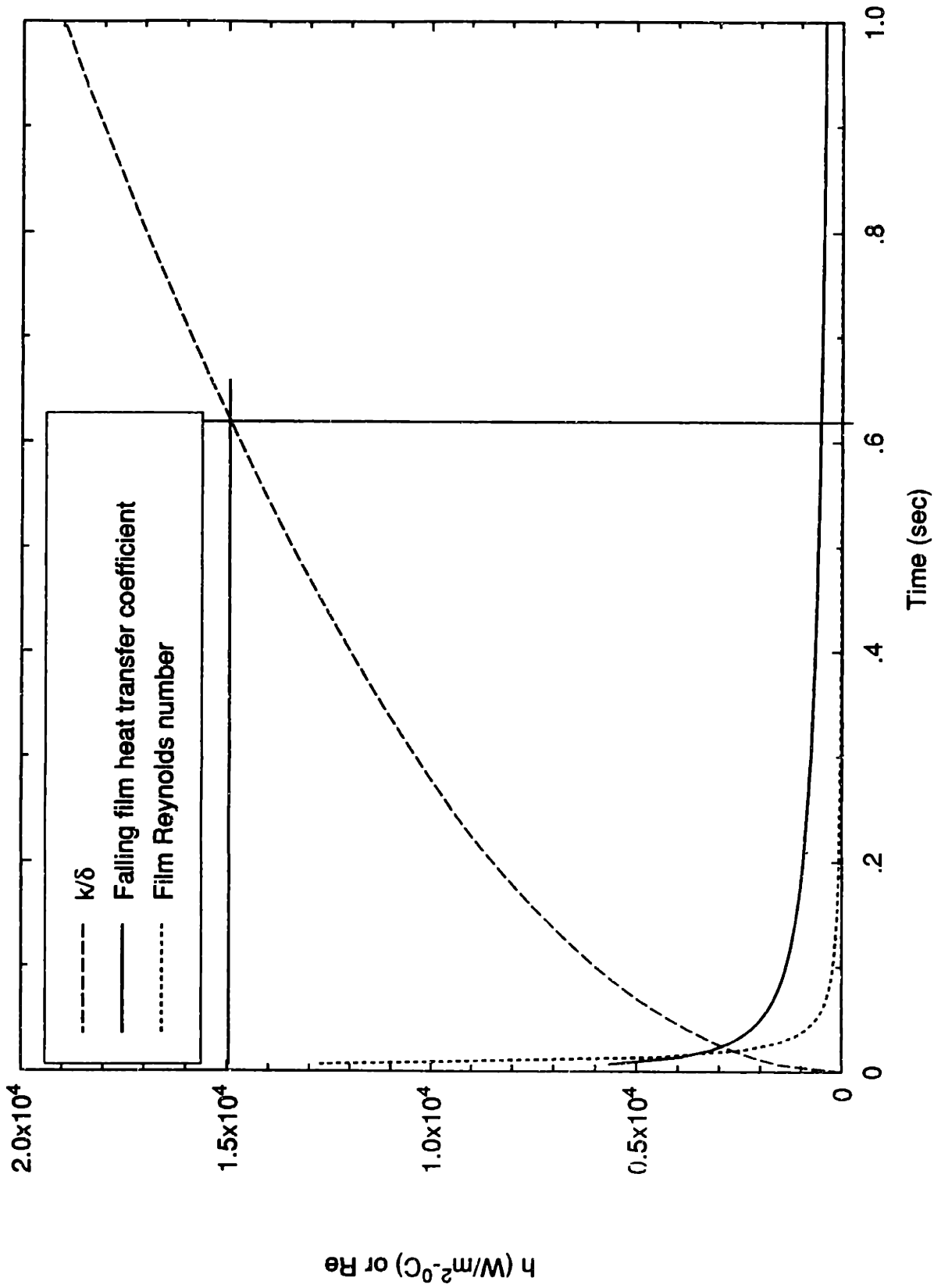

Figure 5.8: Calculated Reynolds number and heat transfer coefficients for falling film

along the length. The water, supplied directly from the system pump (see Figure 3.1), was near the saturation temperature. The assembly was surrounded with transparent lexan sides and top to allow visualization yet keep a steam environment around the boiling film. A high intensity lamp was used to maintain one of the lexan panels hot enough to suppress condensation to ease viewing.

The system was run at operating temperature with heat flux as a parameter. Refering to Figures 5.9-5.11 which are photographs of the liquid film draining down the tube, the following was observed: Nucleation first occurred at a heat flux of about 60 kW/m^2 and this took the form of a very few small bubbles forming along the seam of the pipe where it is presumed that many nucleation sites exist. At a heat flux of 71 kW/m^2, nucleation could be seen sparsely in the region of $\theta<45^0$ with more pronounced bubbling along the seam. The density of sites was greater for the lower half perhaps due to the sensible heating of the water as it flowed downward. At $q'' = 106$ kW/m^2, the nucleation was becoming more apparent, where much of the bubbling appeared in lines parallel to the pipe axis. It is suspected that directionality of the surface texture was responsible for this. It is estimated that there were three to four times as many bubble sites in this case as in the previous case. It was noted that there was some droplet entrainment from the bursting bubbles, but neither the bubbles nor droplets achieved substantial size and thus, the mass of liquid driven from the film was small.

At the highest heat flux of 146 kW/m^2, there was considerable bubbling on the pipe surface, although it still only constituted a small percentage of the pipe surface area. It was estimated that the bubble population density was another factor of three

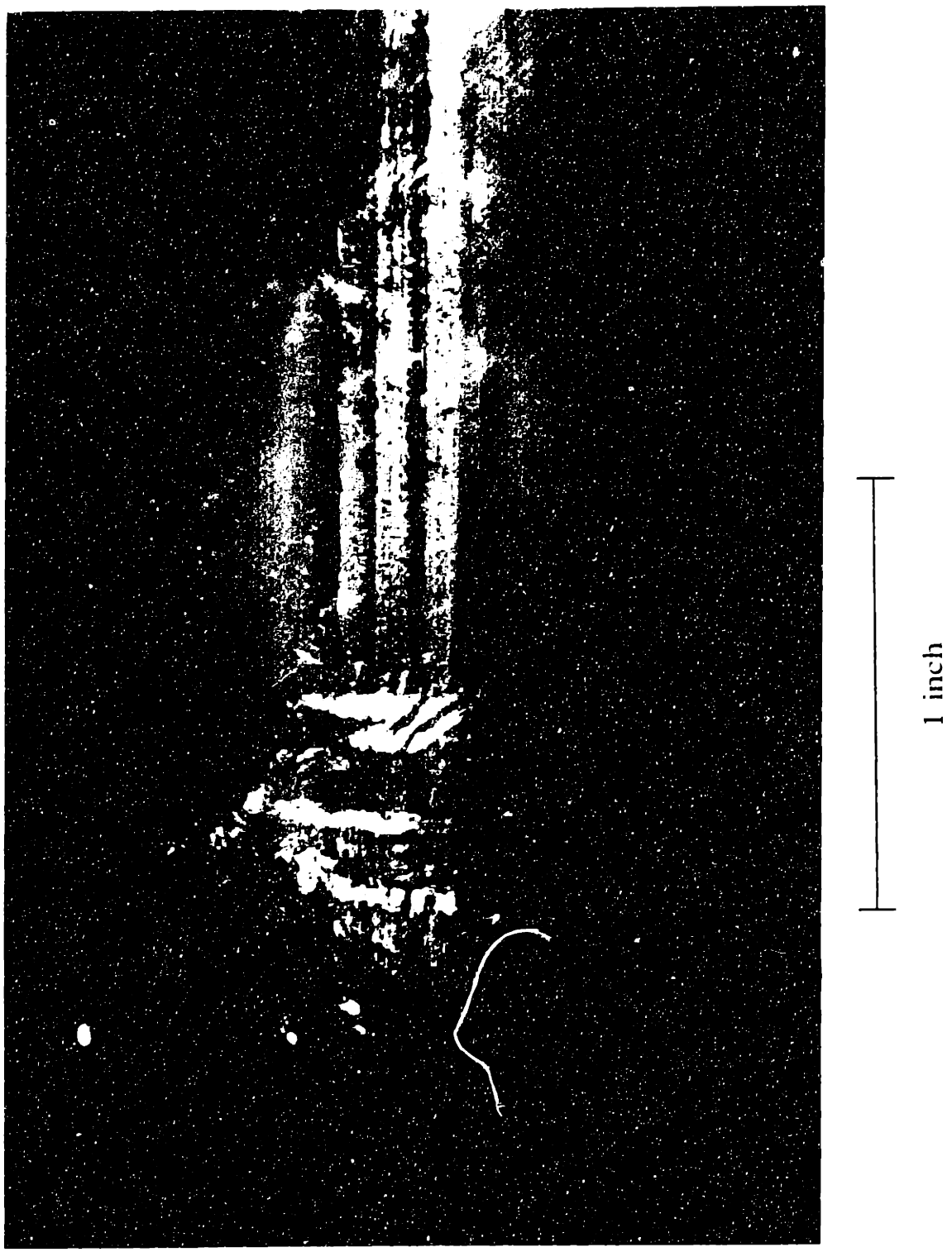

Figure 5.9: Photograph of bubble nucleation ($q'' = 71 kW/m^2$)

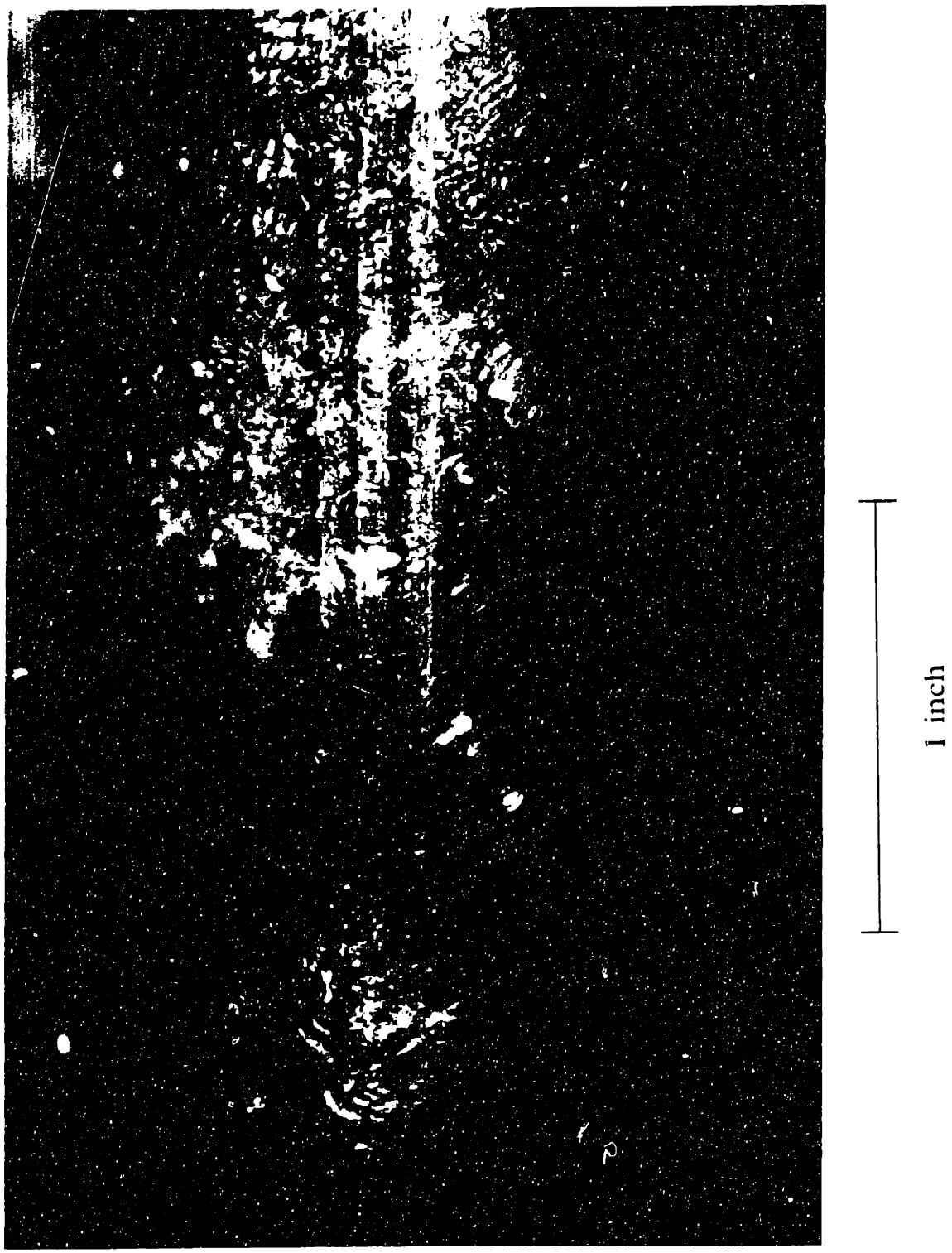

Figure 5.10: Photograph of bubble nucleation ($q'' = 106 kW/m^2$)

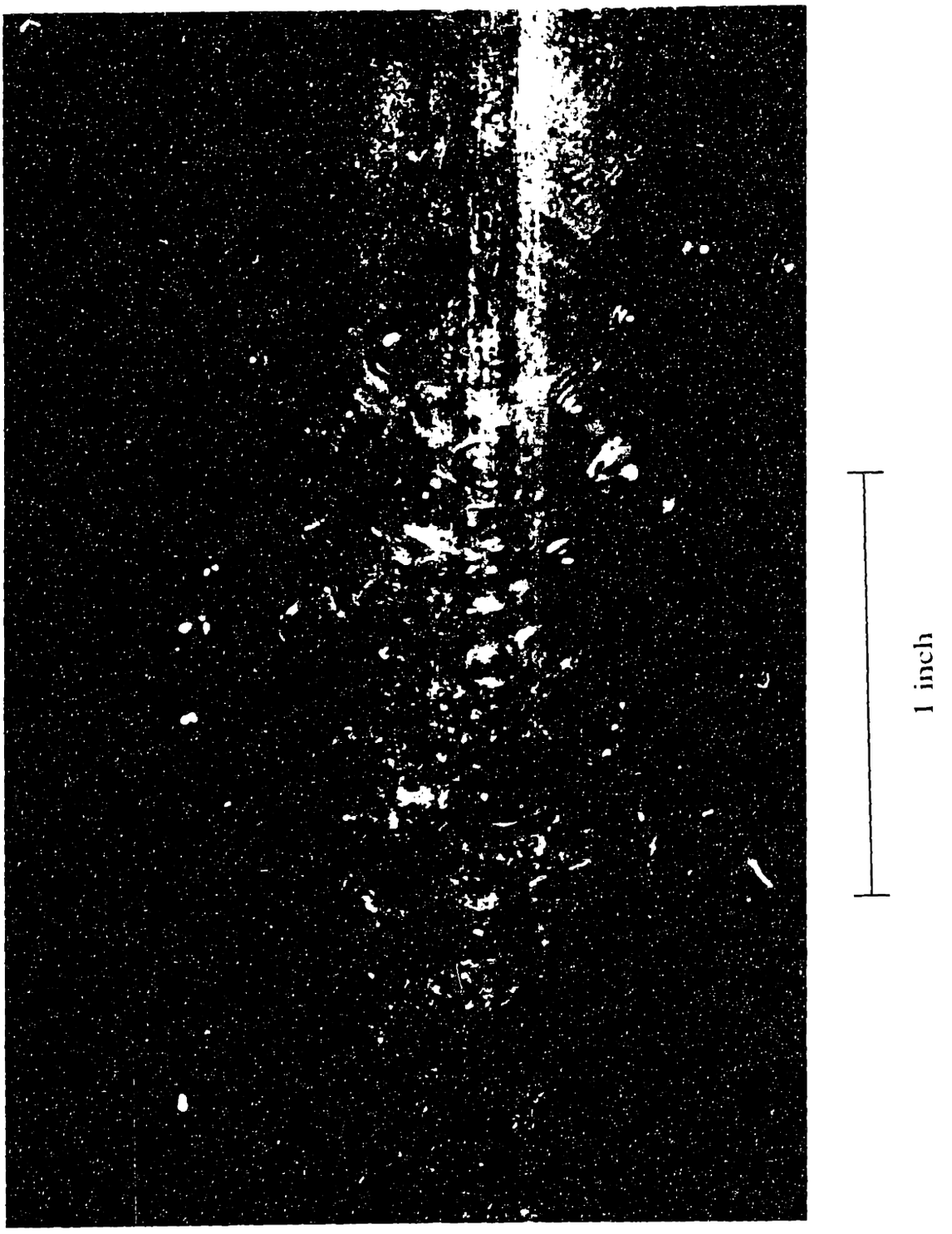

Figure 5.11: Photograph of bubble nucleation ($q'' = 146 kW/m^2$)

greater than the previous heat flux. Spitting due to bubble bursting was estimated in the 100's per second yet the total mass did not appear to be significant. Streaks in the stream direction were observed to be detached bubbles that convected downward. Of course, this contributed to apparent increase in the bubble population with increasing θ.

With a continuous flow of liquid, there was no difficulty in maintaining a continuous film even when the bubble population was at its highest. Intermittently stopping the flow of liquid was useful to simulate the behavior inside of the pipe during an intermittent two-phase flow. Removal of the flow was followed by termination of bubble nucleation within a fraction of a second, consistent with the calculations of section 5.2.3.1 (see Figure 5.8). The rapid thinning of the film allows the wall superheat to drop below the incipience value and suppress nucleate boiling. Dryout of the film usually occurred at a few small locations after a short time; a time which depended on the heat flux. This was followed by a rapid dryout of the complete upper half of the tube shortly thereafter, indicating that as the film thins, it becomes very uniform. It may be expected then, that if dryout occurs, large dry patches result.

Although the existence of nucleate boiling in the film was confirmed for a range of heat fluxes, it appears that its effect is rather benign with respect to dryout. The boiling sites only covered a small part of the pipe area, did not lead to rupturing the film, and did not produce a large mass of entrained droplets. In addition, the nucleate boiling was suppressed rapidly during film drainage, eliminating its effect.

5.2.4. Slug Frequency

The mechanisms depleting the liquid film from the wall are connected to dryout by the frequency of slugging. The dryout boundaries represent equilibrium of these competing effects, so in order to calculate the necessary rewetting frequency, the time required to dry the post-slug film is needed.

The measurement of film thickness was rather inconclusive but both Coney[11] and Fisher & Yu[9] claim to have good agreement between measured and predicted drainage behavior. The theoretical drainage will therefore be used from here forward. It was concluded that bubble nucleation was present but did not contribute to film removal at these heat fluxes. Consequently the dryout time can be computed from the simultaneous action of drainage and evaporation using the result of equation 5-12. The drainage curves and time to dryout is shown for the four heat fluxes in Figure 5.12. With this information, the final factor in the model will be discussed. Slug frequency is a kinematic variable depending on the superficial velocities of the two-phase mixture. Prescribing the necessary frequency gives the necessary minimum liquid velocity $j_{l_{min}}$. Slug frequency has been experimentally studied by Gregory & Scott[15] and Greskovich & Shrier.[22] In these studies, the flows were fully developed (L/D ≥ 300) and typically for sizes of pipe smaller than 2 inches. The form of the correlation given by,

$$v_s = 0.0226\left[\frac{j_l}{gD}\left((j_l + j_g) + \frac{19.75}{j_l + j_g}\right)\right]^{1.2}, \qquad (5\text{-}21)$$

came from three observations of the frequency data: a) The slug frequency increases directly with j_l and inversely with D, b) A frequency minimum exists with respect to the slug velocity, and c) The slug velocity is proportional to the "no-slip velocity",

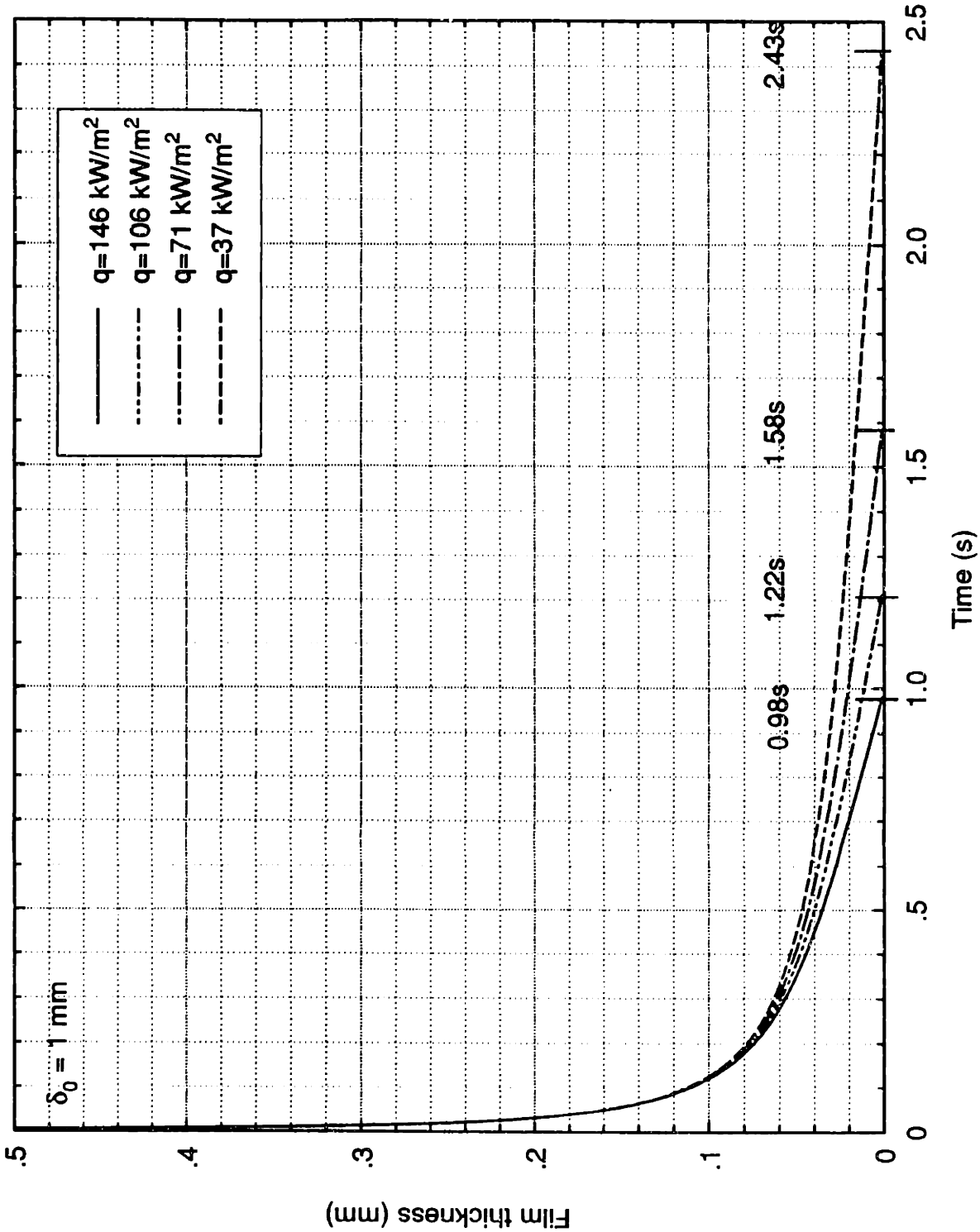

Figure 5.12: Film drainage characteristics at tube top with imposed heat flux

$j_l + j_g$. Curve fitting gave the three constants. The correlation was used by Ruder[5] to construct the previous dryout model but its applicability for 2 inch pipes shorter than the developing length with an imposed heat flux is questionable. This motivated measuring slug frequencies in the present system for comparison to the above correlation and for use in modifying Ruder's thermal bound.

5.2.4.1. Experimental determination of slug frequency

To check the applicability of the fully-developed, adiabatic slug frequency correlation, the slug frequency was measured for the range of superficial velocities encountered in the diabatic experiments. The two-phase flow was produced by both direct steam injection without application of heat and also by boiling single phase liquid with a heat flux of $q'' = 146 kW/m^2$. The method employed the flush conductance probes discussed in section 5.2.2.2. Referring to Fig 5.4, a slug corresponds to a high value of voltage, thus when the voltage exceeds an established baseline, one may count this event as a slug passage. It is this idea that was used in computing slug frequency from the voltage-time traces. For each two-phase condition, voltage-time traces were recorded for four minutes at 20 Hz. For each trace, nine threshold values, ranging from 30-70% of the total voltage range were used for counting. The resulting average of these nine counts (number of slugs), is used to compute the frequency.

For the purpose of this dryout study, it is actually more appropriate to determine the average bubble passage time rather than the slug period, since dryout cannot occur when a slug is present. In the process of correlating the data, the average bubble passage time was computed to be on order of 10% less than the total period. So, the total

period was used as the relevant time scale and any discrepancy adds to the safety factor.

The data was correlated to the same form as that used by Gregory & Scott with empirical constants adjusted. This procedure is justified because the same underlying physics are believed to apply. Figures 5.13 and 5.14 show the result where the frequency is plotted against the correlation function where the constants were evaluated by a least squares fit. Therefore, the best fit straight line has unity slope and nearly intersects the origin as expected. For the unheated two-phase mixture, the data gather fairly well around the line but for the heated case there is more scatter. It will be observed that the constants for the heated case are all larger than for the unheated indicating a larger frequency for the same conditions, as suspected. Also, it is seen that the constants vary considerably from those found in equation 5-21, but it is not clear which case produces higher frequency by inspection. Instead Table 5.1 gives a comparison of computed slug frequency for the Gregory & Scott correlation and the two correlations given here for some typical superficial velocities.

Referring to the table, the Gregory correlation gives lower frequencies than those measured for the present case with no heat addition. This may be explained by the fact that the developing length for this flow exceeds the system length. Therefore, the slugs are still developing and have not reached a spacing large enough such that consecutive slugs don't interact. Slugs shorter than a typical turbulence entrance length would not survive, since one bubble in the wake of another upstream would have the tendency to coalesce with that bubble, making long slugs and bubbles, thereby decreasing the frequency.

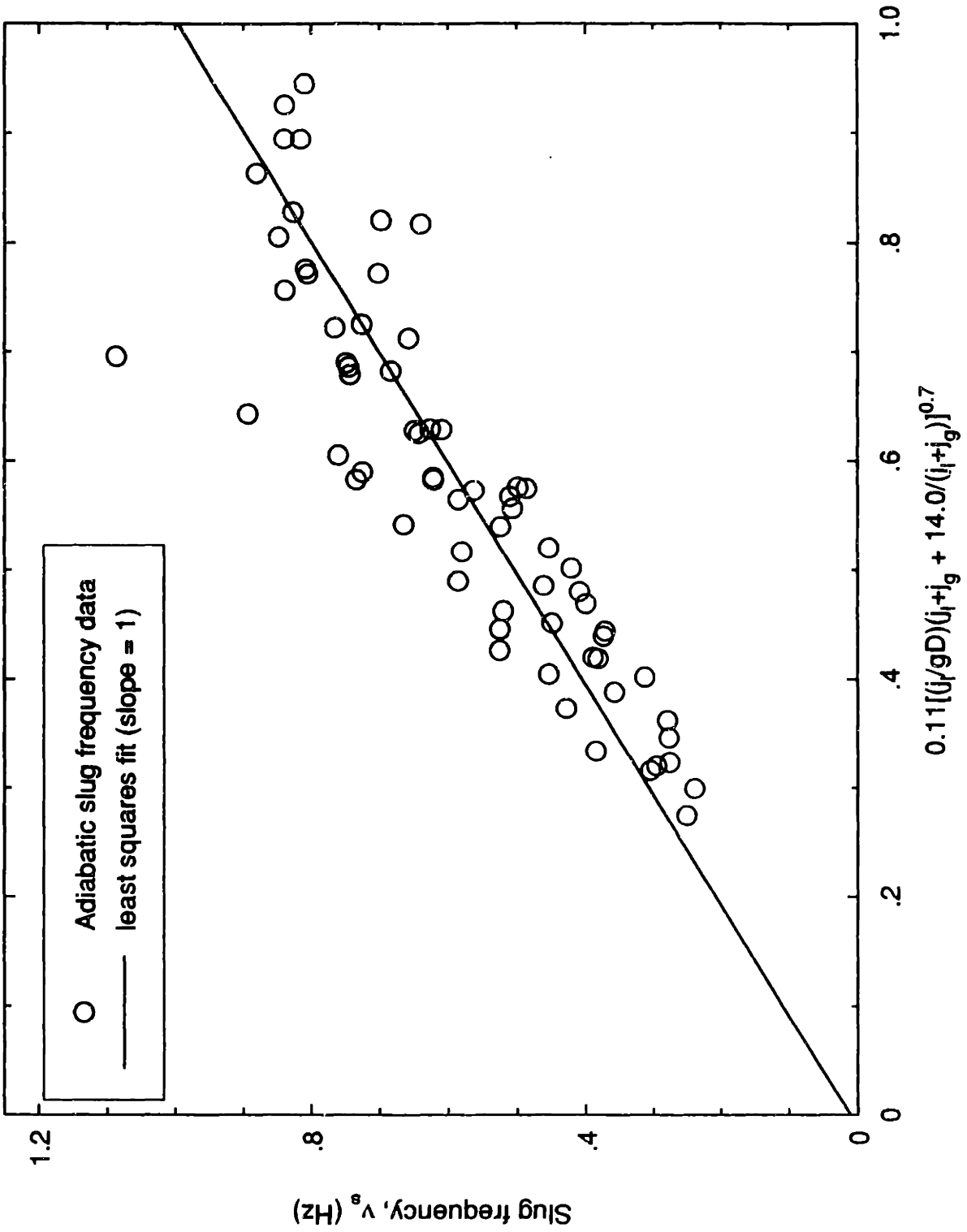

Figure 5.13: Adiabatic slug frequency vs. correlation function

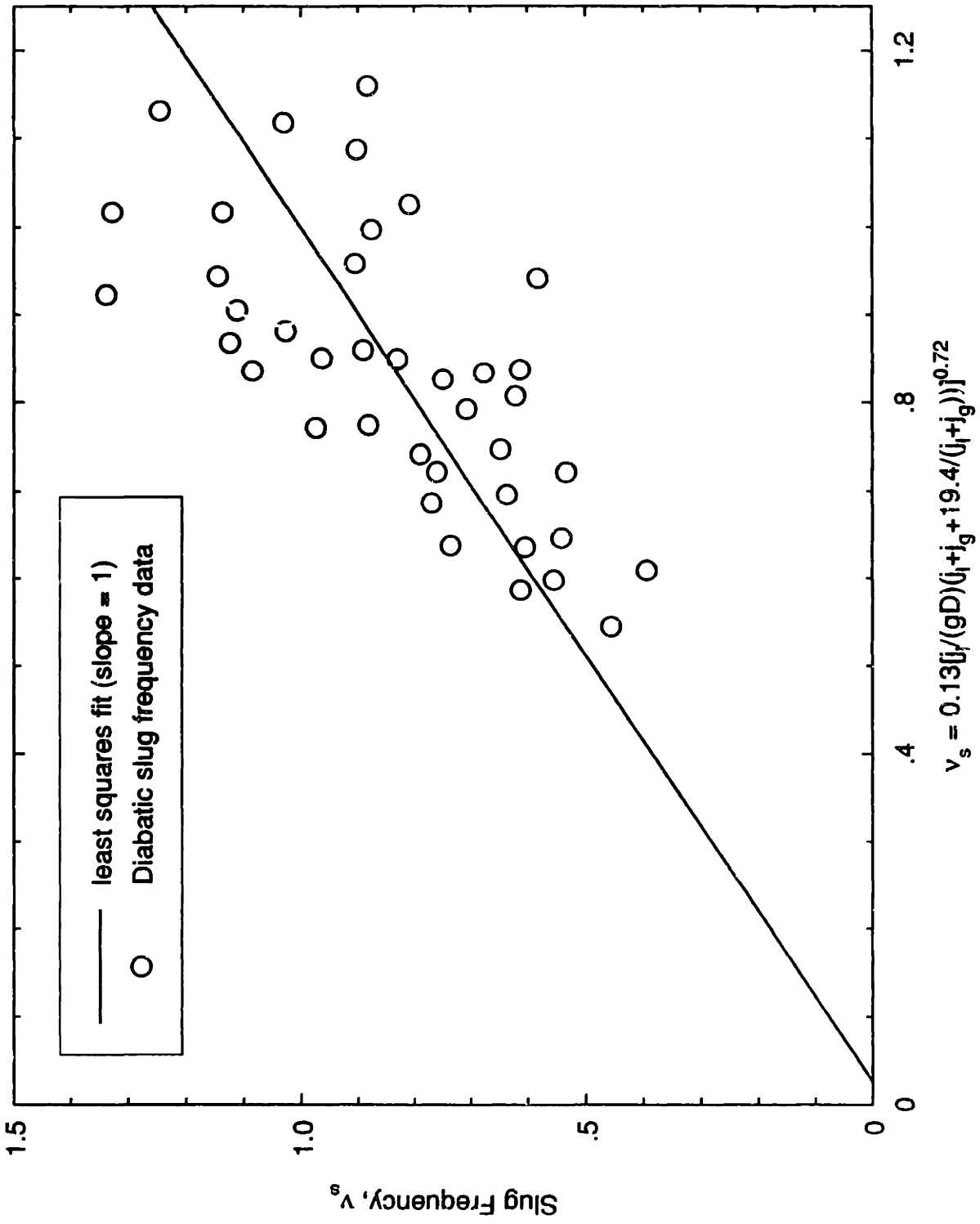

Figure 5.14: Slug frequency vs. correlation function for q'' = 146kW/m^2

Flow conditions		Slug frequencies ν_s (Hz)		
j_g (m/s)	j_l (m/s)	Gregory et. al	Adiabatic	$q'' = 146 kW/m^2$
2.000000	0.250000	0.153310	0.279427	0.405861
2.000000	0.500000	0.328292	0.439876	0.641204
2.000000	0.750000	0.505317	0.571099	0.830967
6.000000	0.250000	0.126733	0.279837	0.364206
6.000000	0.500000	0.295933	0.460720	0.605933
6.000000	0.750000	0.489734	0.620331	0.819925
10.000000	0.250000	0.172673	0.348502	0.439476
10.000000	0.500000	0.404692	0.573543	0.732673
10.000000	0.750000	0.671498	0.771622	0.992877

Table 5.1: Calculated slug frequencies for typical slug flow conditions

The table also indicates that there is frequency augmentation with an applied heat flux. The cause of the increased frequency is not known but can be hypothesized. When the flow is heated, it is expected that higher void exists in the liquid slugs making the *apparent* liquid rate higher, which gives higher frequency (see eqn. 5-21). To substantiate this, the void fraction in the liquid phase can be roughly calculated using the approach of Taitel & Dukler[23] for flow regime transitions in the case of flow boiling. The superficial velocity of the liquid, taken as a mixture of liquid and vapor bubbles, can be found from

$$j_m = \frac{j_l}{1-\alpha} \tag{5-22}$$

According to Taitel & Dukler,[23] the void fraction within the liquid phase depends on heat flux but cannot exceed 0.25 because the bubbly configuration cannot prevail for higher void. For the heat flux in question here, the limiting value is appropriate, so that equation 5-22 yields an apparent superficial liquid velocity 33% higher than actually present. Roughly speaking, this translates to 20-25% higher slug frequencies. Table 5.1 indicates reasonable agreement although the enhancement can be as large as

50%. Since the heated measurements were conducted only at the highest heat flux, it is possible to compare thermal bounds only for this case. The next section addresses this.

5.2.4.2. Comparison of thermal bounding lines

Three bounding loci for intermittent flow dryout will be shown:

1) The bound derived by Ruder which considers evaporation of the liquid film only, where the initial thickness is taken to be 50 μm, balanced by the Gregory & Scott slug frequency

2) The present bound which considers drainage and evaporation simultaneously balanced by the measured frequency for the unheated flow

3) The present bound which considers drainage and evaporation simultaneously balanced by the measured frequency for the application of 146 kW/m^2

Figure 5.15 shows the three loci on superficial velocity coordinates. Each line represents a line of constant slug frequency. The computed bound for adiabatic flow and the Ruder bound are not greatly different, but in the range of gas velocities where slug flow is expected, Ruder's model requires larger liquid rates. This may be due to two effects. The assumption of a 50 μm initial film thickness implies a short time until dryout; for these conditions $\tau = 0.74$ sec.

The more striking result is the lowering of the thermal bound by using the measured frequencies for heated flow. The time to dryout for this case and the adiabatic case was $\tau = 0.98$ seconds computed from equation 5-12 using an initial film thickness of 1 mm. The ratio of peak liquid velocity (i.e j_{l_o} to avoid dryout completely) for this

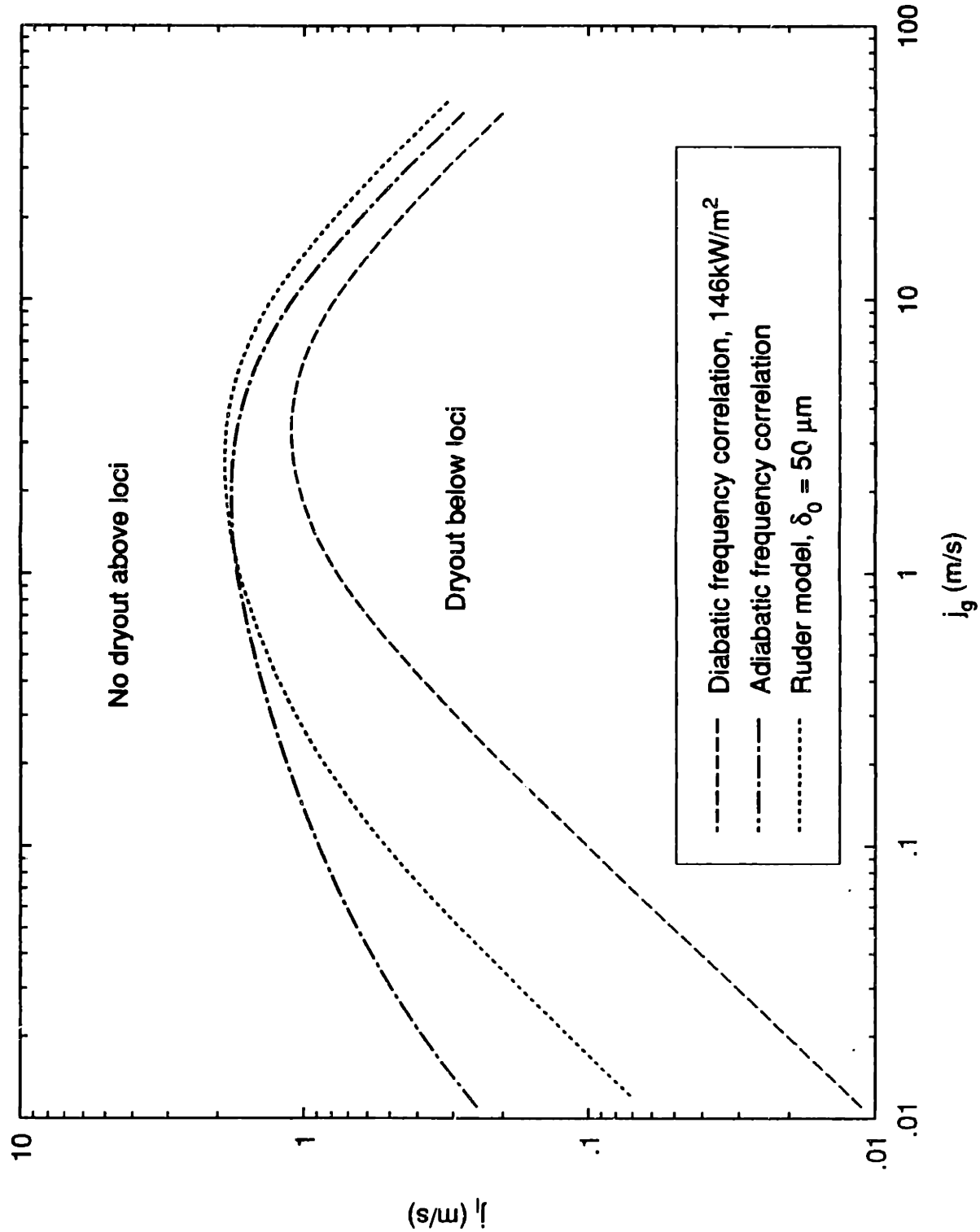

Figure 5.15: Comparison of three intermittent thermal bounds for q″ = 146 kW/m^2

case to that of Ruder's model is 0.58. This may be the chief explanation for the conservative estimates given at high heat flux. The next section compares these bounds with the intermittent dryout data.

5.3. Intermittent dryout data and computed thermal bounds

The four dryout maps for low-moderate quality are revisited here with the addition of the computed thermal bounds. These are shown in Figures 5.16 through 5.19. It should be noted that only the highest heat flux has a comparison of the dryout bound derived from the diabatic frequency correlation. At the lowest heat flux of 37 kW/m^2, the computed thermal dome is wider than the dryout area that is associated with slug flow as well as being situated to the left somewhat. The quality levels are so low that small errors in a heat balance may account for most of this discrepancy. This should not be disturbing since the chief concern is the peak of the dryout dome or minimum velocity required to prevent dryout. For this heat flux, this predicted peak is very close to that measured. For the next higher heat loading, the peak is shifted up considerably exceeding the $Fr_l = 1$ line. Again the dome is to the left of the measured dryout region. The calculated bound is wider than for the lower heat flux, as might be expected, while the dryout shows the opposite effect. It may just be that increasing the ΔT_{fluc} threshold above which dryout is defined is filtering out points that are actually in a dried out state. Reiterating, the enhanced frequency with heat flux is not accounted for here which partially explains the conservative nature of the prediction. The trend continues for $q'' = 106$ kW/m^2, where the dome envelopes all the dryout points present. Finally, at the highest heat flux, the peak associated with unheated fre-

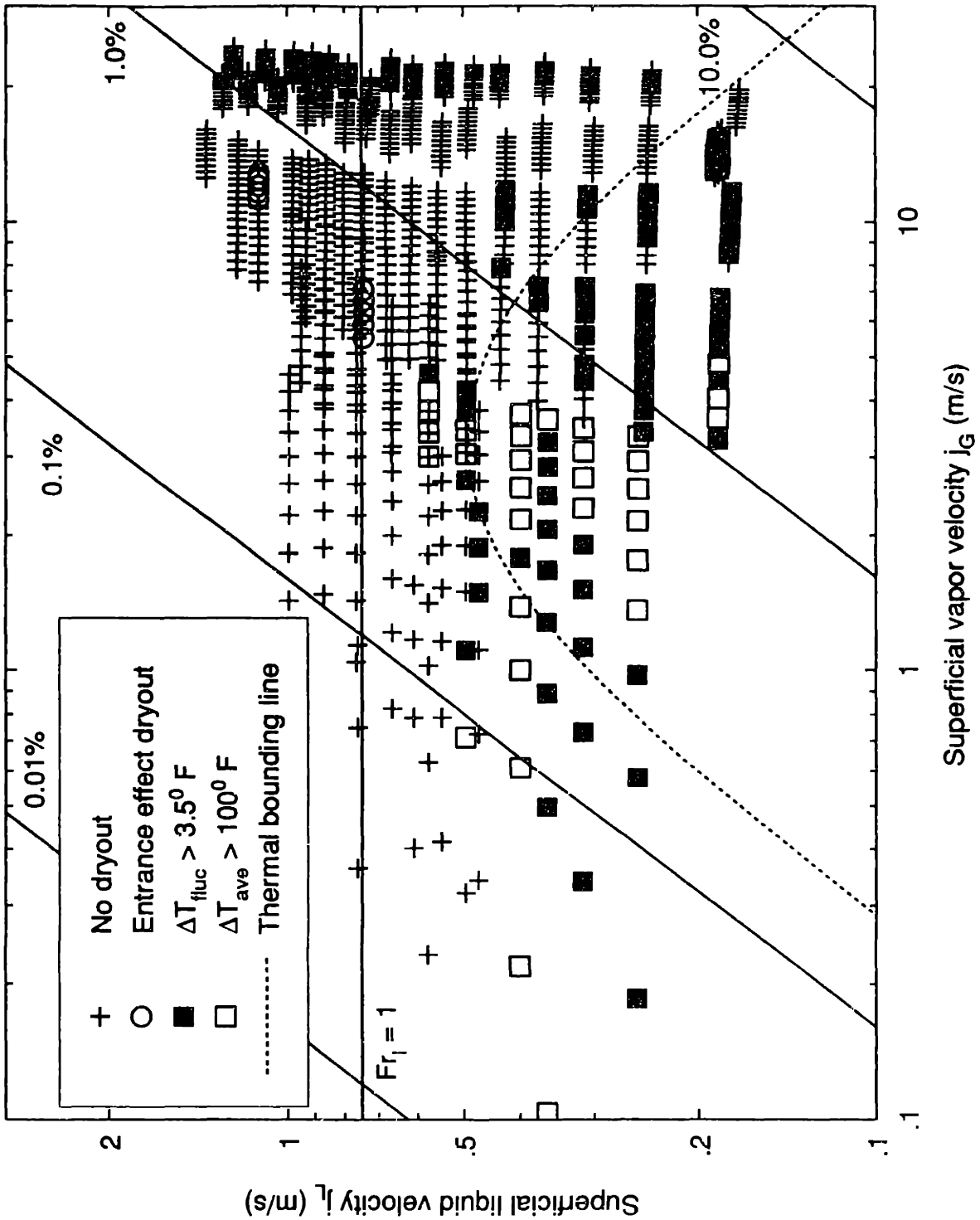

Figure 5.16: Comparison of predicted thermal boundary and dryout data ($q'' = 37$ kW/m^2)

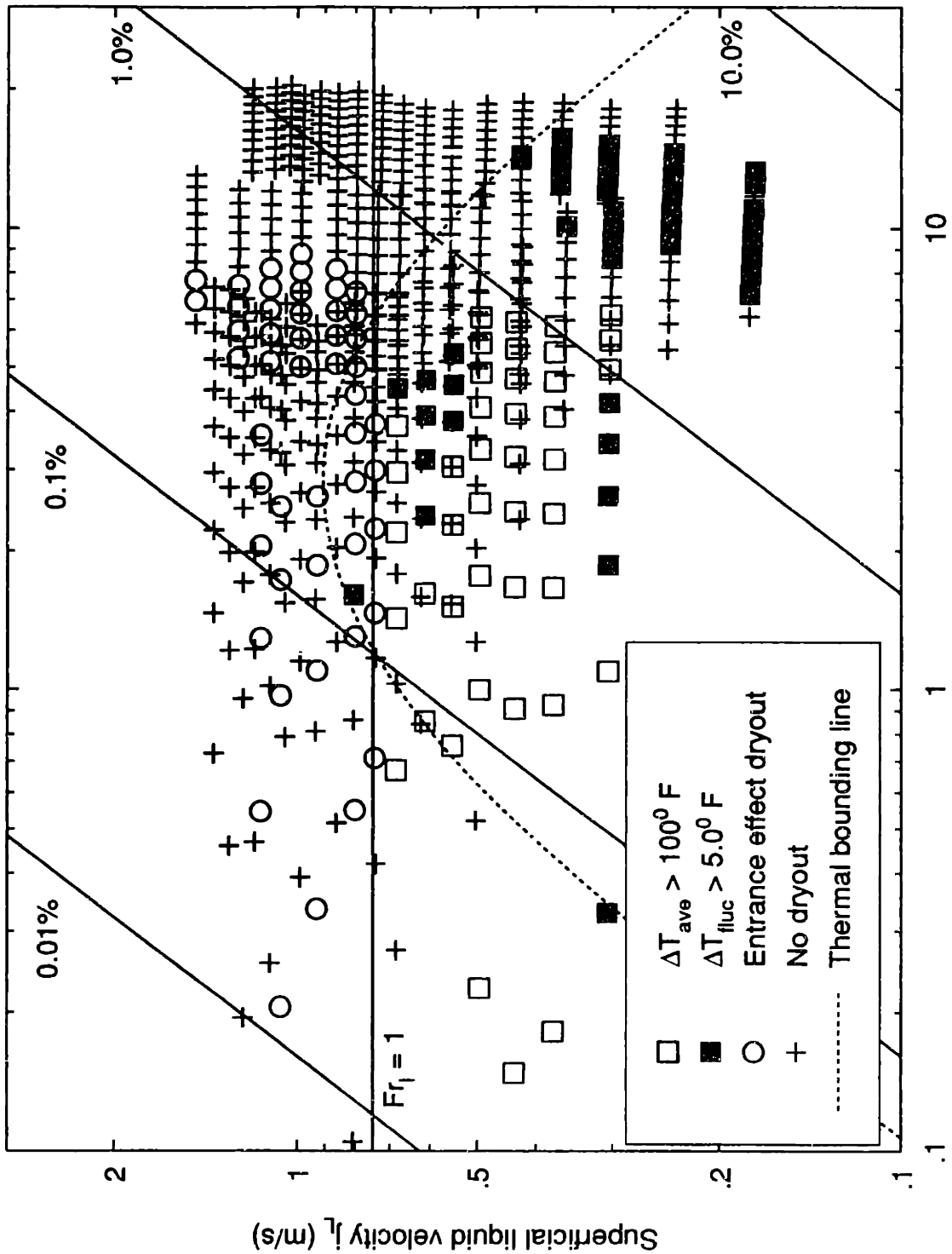

Figure 5.17: Comparison of predicted thermal boundary and dryout data ($q'' = 71$ kW/m^2)

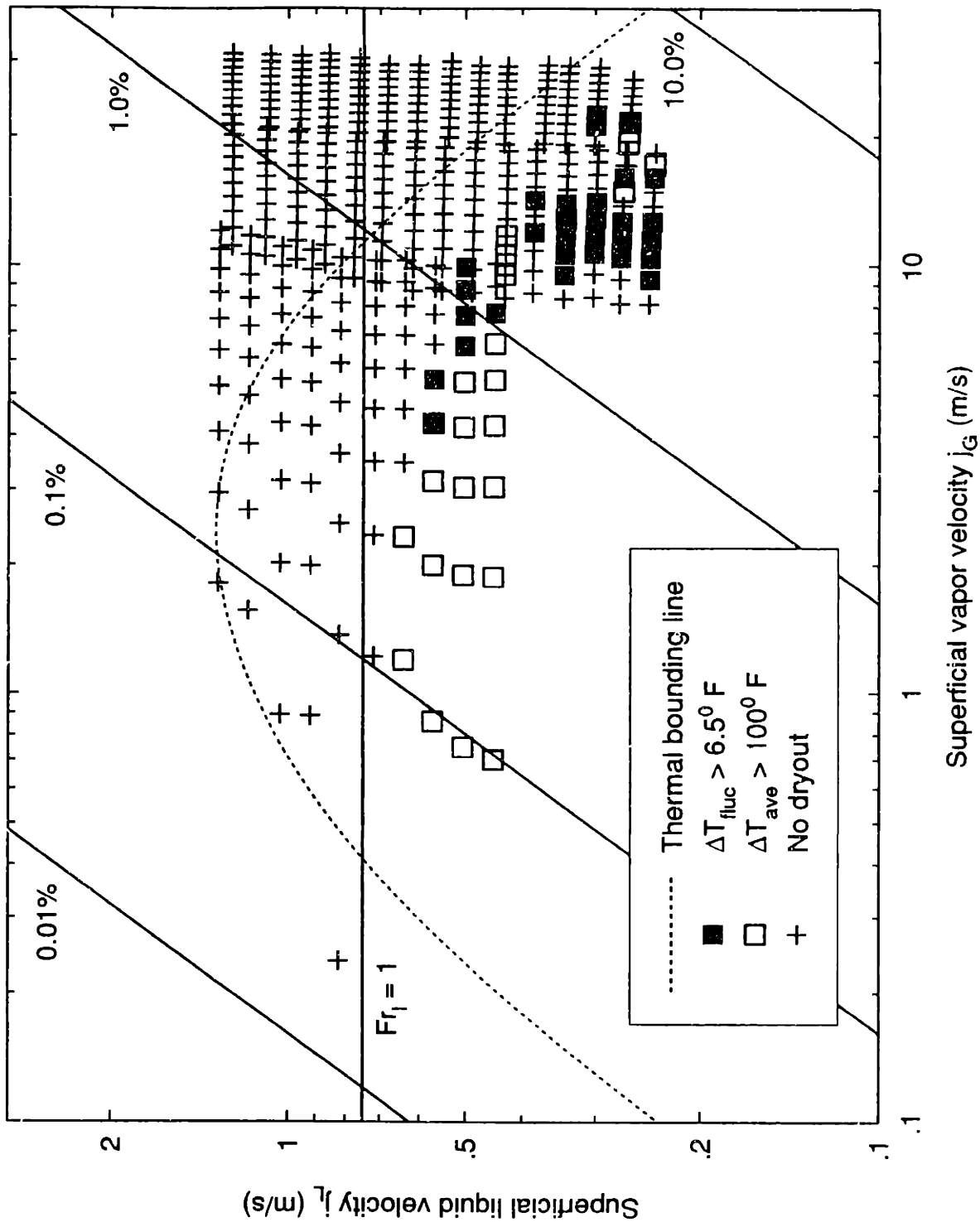

Figure 5.18: Comparison of predicted thermal boundary and dryout data (q'' = 106 kW/m^2)

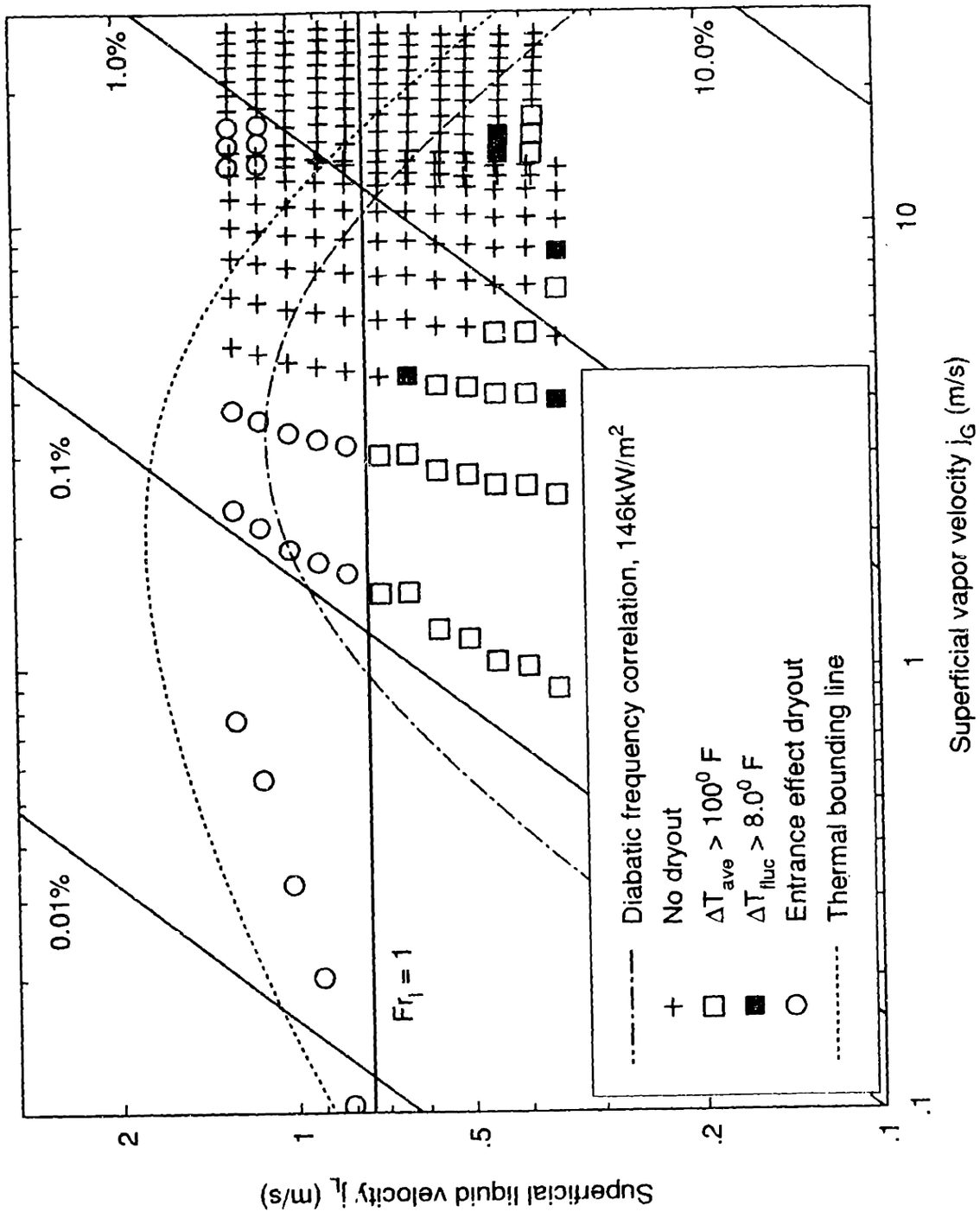

Figure 5.19: Comparison of predicted thermal boundary and dryout data (q'' = 146 kW/m^2)

quency model is nearly 2 m/s and is extremely conservative, in agreement with the findings of Ruder. The locus computed from the heated frequency correlation is substantially lower but still much higher than the points defined as intermittent dryout.

It is difficult to conclude much at this point except that under diabatic conditions, increased frequency of slugging is beneficial in the prevention of dryout. However, higher heat flux still requires greater liquid velocity because the evaporation rate increases faster than rewetting frequency according to the model assembled here. It is not obvious what is missing from the physics that would bring the experimental results and prediction into closer agreement. However, the inference of dryout from measurement of external pipe temperatures is rather indirect and may be somewhat misleading. Appendix B discusses the sensitivity of the experimentally found aniisothermal region to changes in the temperature oscillation amplitude threshold used.

5.4. Recommendations for the moderate quality region

Since the effects of bubble nucleation in the post-slug film were dismissed for any practical operating conditions, the film depletion mechanisms are confined to the drainage and evaporation. The time required for film dryout at the tube top can be calculated using equation 5-12 by supplying the initial film thickness. Using any value in excess of that calculated with equations 5-3,4 is recommended. The location of thermal bounding line should be calculated using the inverse of the time to dryout in the fully-developed, adiabatic slug frequency correlation (equation 5-21). The peak of this dome gives the minimum required liquid superficial velocity. This was done by Ruder,[5] where the only difference here is the time to dryout. Using the same approach

employed by Ruder the critical liquid velocity is:

$$j_l = 2.65gD\ t_{dryout}^{-0.833} \tag{5-23}$$

or in terms of the liquid Froude number,

$$Fr_l = 2.65\sqrt{gD}\ t_{dryout}^{-0.833} \tag{5-24}$$

This criterion gives the recommended minimum liquid velocity that should be used when encountering intermittent flow in horizontal steam generating tubes. Since the slug frequency correlation is not dimensionally consistent, the user must supply mks units for the above two relations. It suggested that increased slug frequency associated with developing flow and diabatic conditions be accepted as a safety margin. In addition, since the slug period is greater than the actual time for bubble passage, an additional safety margin is gained.

A specific recommendation concerning entrance effects cannot be given. The presence of adverse inlet conditions to a large extent invalidates the preceding recommendation. The presence of fabrication defects, piping junctions, etc., should be considered at all times and evaluated for the specific system in question. It cannot be ascertained that Ruder's recommendation of $Fr_l = 2$ will be sufficient to maintain isothermal pipe behavior when entrance conditions are present. It is quite possible given the nature of these entrance effects, that increased velocity will never rectify the problem. It is suggested to address these problems locally.

CHAPTER 6

Mechanisms of Annular Flow: High Quality Dryout Investigation

6.1. Motivation

Annular flow is one of the four major flow regimes encountered in horizontal pipes and occurs at relatively high quality. Because of its prevalence in horizontal evaporator tubes, it is important to understand this flow regime and be able to calculate its properties. Presently, little is known about annular flow except for some general guidelines for determining the conditions under which it is present and correlations for pressure drop and heat transfer. Much of the information concerning its characteristics, such as liquid film thickness, film flow rate, and drop entrainment flux come from experimental data. In order to calculate, quantities of interest like pressure drop, heat transfer, and dryout limits, it is desirable, if not essential to know the liquid distribution in the flow. Presently, the reasons why annular flow can exist in horizontal pipes is still somewhat mysterious and predictive models to determine liquid distribution for use under more general flow conditions is beyond the state of the art. Typically, practical quantities are found through the use of more global parameters like the Martinelli Parameter and use of the experimental data.

The scope of this work concerns liquid distribution for the prediction of dryout limits. A by-product of this study, it is hoped, will be further insight into the mechanisms driving annular flow. This, then may contribute to more physically based models for calculation of heat transfer and hydrodynamic quantities of interest to the engineer.

Dryout in horizontal tubes comes in three varieties. The stratified or low quality dryout and the slug flow or intermediate quality dryout have been discussed in detail. The results of the previous chapter show that the intermittent dryout peak is not limiting but is significantly lower than the $Fr_l = 1$ limit at atmospheric pressure. The question arises, is there a minimum water side velocity to avoid annular flow dryout in once-through heat exchangers? Also, is there a quality (or minimum gas velocity) boundary that delineates pipe isothermal operation from a dryout condition? Because the pipe will ultimately run out of liquid in a once-through boiler, dryout is inevitable and is expected realistically at qualities less than 100% and this limit is therefore useful.

Dryout in the annular flow regime occurs when there is a discontinuous annular film. To predict high quality dryout under various conditions, it is necessary to know which mechanisms producing annular flow have failed at the dryout boundary. For example, has the annulus become discontinuous before a significant amount of droplet interchange has occurred, or has the once-sufficient droplet entrainment become depleted?

Another issue is the role of heat flux. Presently, it is believed that the onset of annular flow is a purely hydrodynamic boundary but this has not been confirmed. In addition, the mechanisms driving annular flow have been essentially proposed and

described qualitatively. One goal of the present study is to begin quantifying the annular flow mechanism of *circumferential secondary gas flow*. As will be seen, secondary flow and the associated shear stress are important factors in keeping the tube top wet. Until now, no one has had an explanation for why the secondary flow is up at the wall, much less its magnitude.

Finally, it would be useful to put the work in a more general context. The liquid distribution and locations of high quality dryout in more complex geometries such as rod bundles or eccentric annuli is not intuitive. Understanding the nature of secondary currents in these flow domains could prove to be useful in predicting the flow patterns and liquid distribution. This chapter will give some background on the problem at hand together with a review of previous work and finally a description of the present experimental study.

6.2. Background and Literature Review

To orient the reader, it is useful to refer to the superficial velocity flow regime map reintroduced in Figure 6.1 which shows the adiabatic boundaries for two inch pipe using atmospheric steam-water. This study will focus on the annular flow (A) region shown to the right of the stratified-wavy (SW) region. The annular flow region has two dryout boundaries. These are the SW-A transition and the high quality dryout bound.[24] However, it is not clear how the SW-A transition has been defined in previous work on flow regime boundaries. Pseudo-annular flow, where the structure is essentially annular with a discontinuous annulus at the tube top, is the likely interpretation. However, this is a condition of dryout. If the annular flow definition requires a

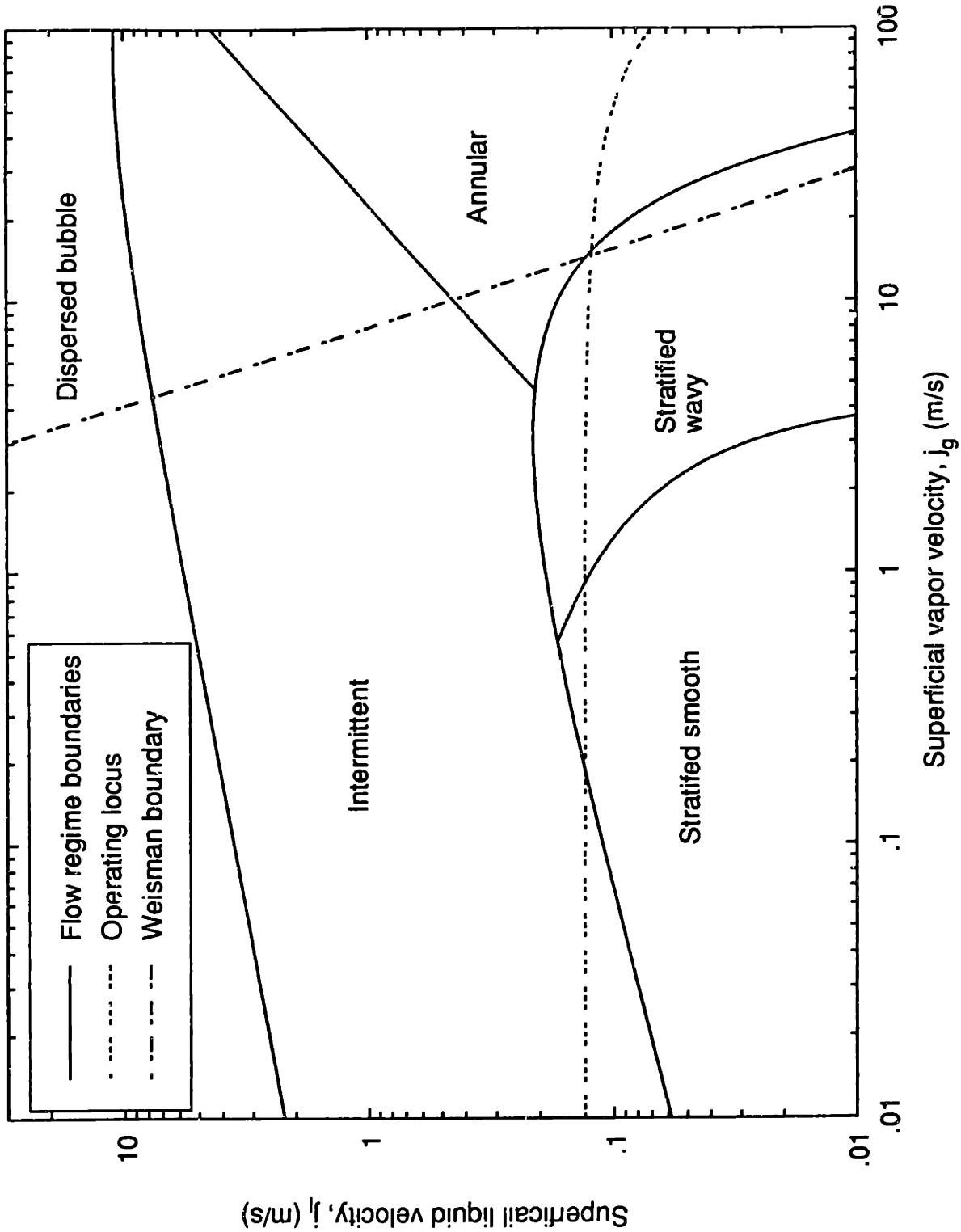

Figure 6.1: Flow regime map for two-inch horizontal adiabatic flow

continuous annulus, then dryout is precluded by the definition. This study's goal is to find the dryout bound associated with the SW-A transition experimentally. and to determine how heat flux affects this boundary. A simple physically based model containing the most important mechanisms for predicting this bound will then be developed. The background and literature review will be given topically.

6.2.1. Flow Regime Boundaries

Taitel & Dukler[1] gave a theoretical boundary for the onset of annular flow. Numerical solution of the transition criterion yields the SW-A boundary in Figure 6.1. Weisman[3] compared the Taitel & Dukler transition to a large number of data sets and the results indicate that this boundary did not predict the data as well as the onset proposed by Weisman which is:

$$\frac{j_g}{\sqrt{gD}} = \left[\frac{1.9(j_g/j_l)^{0.125}[g(\rho_l - \rho_g)\sigma]^{0.05}}{\rho_g^{0.1} j_g^{0.2}} \right]^{2.78} \tag{6-1}$$

This is the commonly accepted boundary.

6.2.2. Film Thickness

Annular film thickness has been measured as a function of circumferential position, θ and flow conditions by many workers using conductance probes or needle contact devices, notably Laurinat[25] and Butterworth.[26] The same trend is always present. The top of the tube has a thin, slightly wavy film which increases in both thickness and wave amplitude as one moves toward the bottom where a rather thick, wavy layer resides. Figure 6.2 shows some typical values for a two inch pipe. The wave amplitude can be on the order of five times the average thickness and the instantaneous

thickness can vary up to a factor of 30 depending on the circumferential position, θ. A good review of this literature is in Hewitt & Hall-Taylor.[27]

The mechanisms commonly held to drive horizontal annular flow[26] are illustrated in Figure 6.2 which is a sketch of annular flow in detail in a pipe. Each mechanism will be discussed in the following sections.

6.2.3. Surface Tension

Although surface tension is usually mentioned as a force holding liquid at the top, it is not a principal player for industrially important pipe sizes. The importance of surface tension compared to gravity is dictated by the Bond number, $\rho_l g \delta R/\sigma$, which is much larger than unity for the systems discussed here.

6.2.4. Droplet Interchange

Droplet interchange is the net effect of entrainment of liquid drops from the film into the core and re-deposition of these drops from the core onto the film. At high enough vapor velocities, momentum transferred from the vapor core to the wavy film results in stripping of droplets from the annulus and into the core. Within the core, they are under the influence of gravity and turbulent eddy motion. This is commonly known as entrainment and only occurs to a measurable extent if the core average velocity exceeds a threshold. Deposition of the entrained drops results when a drop trajectory intersects the annular film. The entrainment at the tube top (where the film is thin) is much smaller than at the bottom, whereas the deposition is nearly uniform around θ. Thus, there is a net *interchange* at the top because deposition exceeds entrainment. Conversely, the interchange must be negative at the bottom.

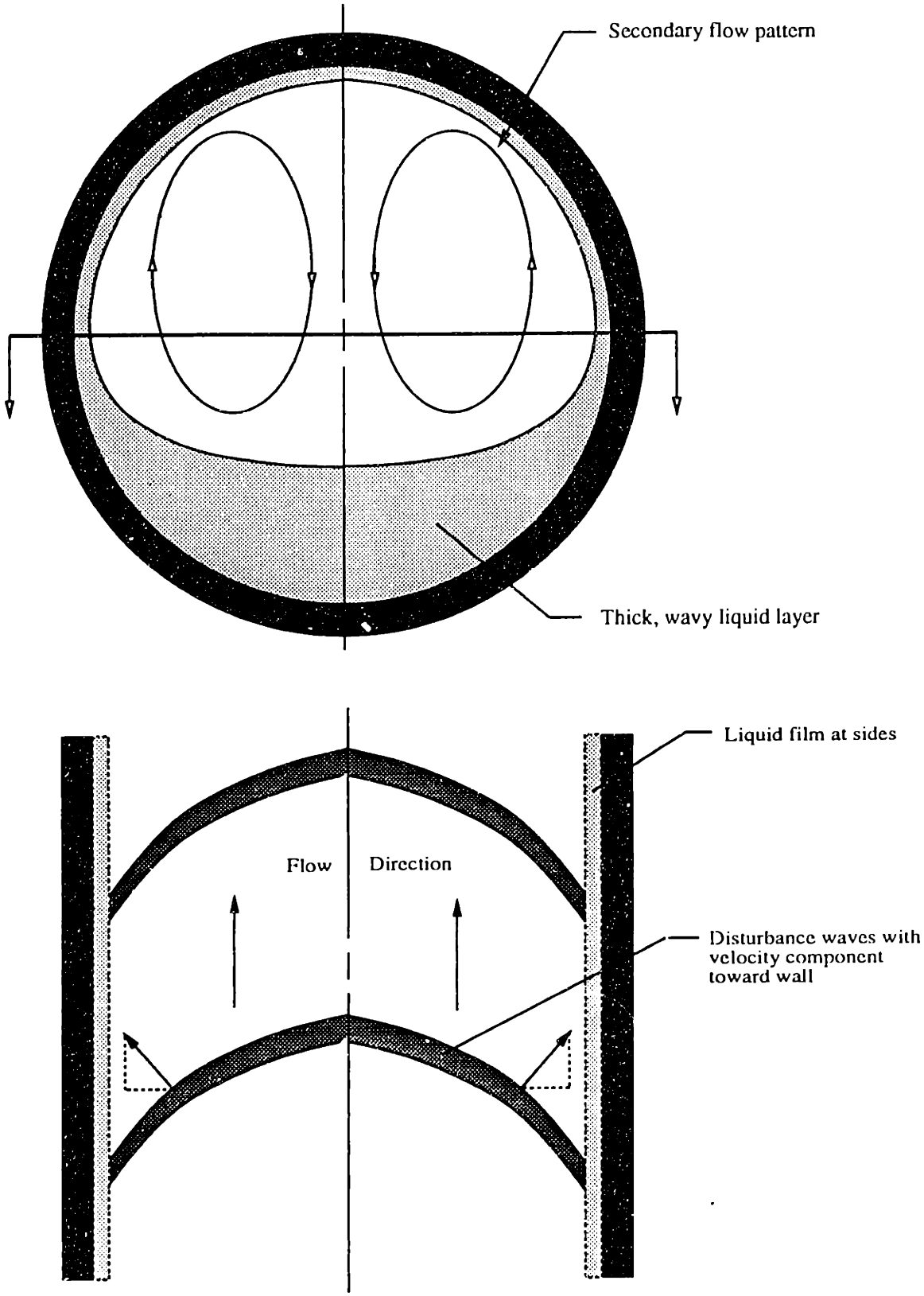

Figure 6.2: Sketch illustrating secondary flow and wave spreading mechanisms

The onset of entrainment has been correlated over a wide database by Hewitt & Hall-Taylor[27] as:

$$j_g = 1.5x10^{-4}\sqrt{\frac{\rho_l}{\rho_g}}\frac{\sigma}{\mu_g} \tag{6-2}$$

For air-water flow at atmospheric pressure, the critical velocity is about 70 ft/s. For increasing gas velocity, the entrainment flux increases as measured axially.

Anderson & Russell[28] measured droplet interchange rates and found that this data could be correlated in the form:

$$G_i = \frac{A}{1 + \cos\theta} - B. \tag{6-3}$$

A and B were extracted from fitting to the data. In contrast to this work, Butterworth[26] has used this correlation to determine a film thickness distribution if interchange and gravity are the only factors considered. The mass balance equation for the film yields the following thickness distribution:

$$\delta^3 = \frac{3\mu_l R}{(\rho_l - \rho_g)\rho_l g}\left[\frac{A\tan\theta/2}{\sin\theta} - B\right] \tag{6-4}$$

Based on film thickness measurements, he computes A and B and finds they are about one order of magnitude greater than Anderson & Russell found in their experiments. Consequently, Butterworth concludes that entrainment/deposition cannot be a major factor in supporting the films found in the experiments.

6.2.5. Wave spreading

Horizontal annular flow is always co-current where most of the liquid flows along the bottom of the pipe. This bottom layer is significantly thicker than the film on the sides or tube top and is quite wavy due to imposed shear of the high speed vapor core.

The speed of gravity waves in still water increases with depth. In a moving liquid, the fluid velocity contributes to the overall wavespeed. Both the depth and the fluid velocity are maximum at the very pipe bottom in a horizontal annular flow. Therefore, wavefronts in this thick bottom layer do not have a uniform speed. As a result, wavecrests oriented normal to the pipe axis initially, get tilted and have a component toward the wall (see Figure 6.2). With the force of the flowing gas on the wave, liquid can impact the pipe wall and be transferred up the wall in the same way that water moves up onto the beach as gravity waves approach the shore. This is known as *wave spreading,* and is generally accepted to aid in producing annular flow.

The concept of wave spreading in horizontal flow has been put forth by Butterworth,[26] and Butterworth & Pulling[29] More recently Jayanti et. al.[30] has attempted to validate its existence experimentally while Fukano & Ousaka[31] have tried to model it. Butterworth & Pulling argue the existence of circumferential transport based on experiments where dye was injected at $\theta = 90^0$. The dye shows a general downward flow (as well as axial) except intermittently when its direction is upward associated with passage of a disturbance wave. This general pattern has also been observed in the dye visualization studies of Flores.[32] These dye experiments show that liquid is intermittently transported at least to the $\theta = 90^0$ point, however there is no evidence, that this mechanism can take liquid all the way to the top.

Butterworth also supports the notion of wave spreading in horizontal flow from a comparison to vertical annular flow, where the other mechanisms don't exist. Butterworth introduces a spreading coefficient, k such that:

$$\Gamma_\theta = -\frac{k}{R}\frac{\partial \Gamma_z}{\partial \theta} \tag{6-5}$$

k is estimated from the data and is of the same magnitude as k for vertical flow so he concludes it is a likely force in film transport.

Recently Jayanti et. al.[30] measured the time-dependent behavior of annular films in a 32 mm diameter pipe as a function of flow conditions and circumferential angle θ. The premise of the investigation was that if the same dominant frequencies in the film thickness traces could be found at different circumferential locations, then it may be argued that liquid is transported between these locations. The film thickness was measured at several axial and circumferential locations using pin-type conductance probes. The autospectral density functions were computed for these film thickness traces and gave the dominant frequency at these locations. The results show that for low gas rates (annular flow prevailing), the dominant frequency at the pipe bottom is about 4-5 Hz, corresponding to disturbance waves, and is a major component up through 90^0 from the pipe bottom. At higher gas rates, the extent of the disturbance wave frequency is felt up to 135^0 from the bottom. At very high gas rates, the frequency spectrum is similar at all angles θ. It is concluded that at high gas rates there is circumferential spreading of liquid from the bottom, since the frequency characteristics appear to have come from the bottom.

The physical picture Jayanti gives of the transport is as follows: Until the flow is developed, the wave in the thicker bottom layer travels faster than in the film above. When the flow develops, and the wave becomes circumferentially coherent, (uniform speed) the bottom of the wavefront is ahead of the sides and top. Since the wavespeed

is larger than the liquid velocity in the annulus, the wave acts like a solid entity sweeping fluid up the wall much a like wedge would do. At high enough vapor speed. the top has a frequency content like the bottom which is dominated by disturbance wave frequencies. However, it should be noted that at these high flow conditions, the thickness variation around θ is less than in the low flow cases, and it may be expected that the frequency content is dictated by the film thickness and the gas velocity. There is no evidence that information (liquid) has traveled up to the top. The physical picture is interesting but unsubstantiated. In addition, the gas flow rates being referred to correspond to $j_g = 70$ m/s which are well beyond the scope of the present study.

Fukano & Ousaka[31] predict the film thickness distribution in a 26 mm diameter pipe using a model built around the *pumping action of disturbance waves.* Figure 6.3 which comes from directly from this reference[31] is shown for illustration. Essentially,

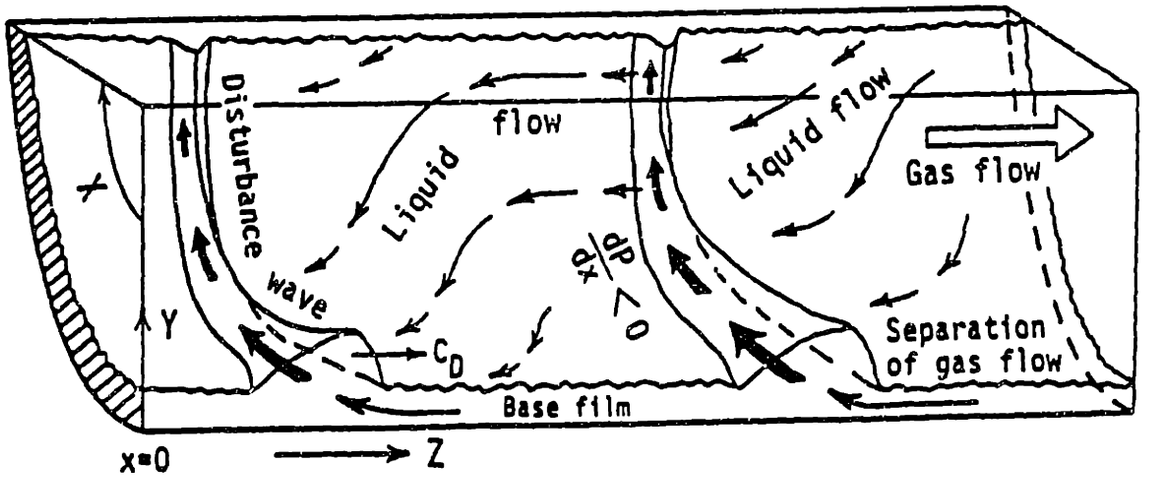

Figure 6.3 Flow model: Pumping action of the disturbance wave (from ref. 31)

the authors say that disturbance waves, which have spread to some extent up the pipe, are channels for an upward flow of liquid driven by a circumferential pressure gradient, the origin of which is not clearly explained. The wave sheds some fluid to the base film as it propagates only to be picked up by the next disturbance wave. The authors note that the pressure gradient will cause secondary flow but neglect its effect on film transport. Circumferential pressure gradients have been measured[32] in an asymmetrically roughened pipe which, as will be discussed, effectively mimics some aspects of an annular flow. Therefore, it would appear that disturbance waves are not essential for a top-bottom pressure gradient to develop. Nevertheless, the term in their analysis representing shear due to secondary flow is neglected.

The basic modeling equations are similar to those used by Laurinat[25] but since the secondary flow term is not included, there is one less undetermined constant. The one unknown constant in the model relates the normal circumferential stress τ_{xx}, in the film and the circumferential pressure gradient. It is determined by fitting the model to the data at $\theta = 180^0$ (bottom). The comparison of data and model is very good. The major objection to this work is that the secondary flow mechanism is excluded in favor of a new mechanism that is not clearly explained. However, it is based on a circumferential pressure gradient, which is now known to exist in asymmetrically roughened pipe and is linked to secondary flow. In addition, it seems doubtful that small circumferential pressure gradients could transport liquid against gravity in the envelope of a disturbance wave, because gravity should dominate for this thickness magnitude (see Figure 6.3).

6.2.6. Circumferential secondary flow

The role of secondary flow in the gas core in affecting annular flow is rather controversial. Though no one has denied its presence as a possible driver, no one has measured secondary currents in the core of an annular flow and several researchers believe they have negligible impact. Only in the present study has it been observed in a horizontal, annular flow.

The non-uniformity of film thickness in horizontal flow gives rise to circumferential dependence of film wave heights. Associated with the wavy film is an effective roughness. In fact, Wallis[33] correlates the film thickness in annular flow to a skin friction coefficient as:

$$C_f = 0.005\left[1 + 300\frac{\delta}{D}\right] \tag{6-6}$$

Due to the asymmetry of the pipe effective roughness, the axial velocity profile is skewed toward the smooth top. It is believed that secondary flow in the gas core occurs as the result of a) tilting and stretching of vortex rings known as *Prandtl's secondary flow of the first kind,* which occurs for example when a laminar flow goes through a bend. and b) anisotropy of the Reynolds stresses known as *Prandtl's secondary flow of the second kind,* which is strictly a turbulence phenomenon and has been measured in the corner regions of flow in non-circular cross sections.[34]

Hinze[34] has measured turbulent flow in rectangular ducts with asymmetric roughness and found that it satisfies a simplified turbulent kinetic energy relation. It essentially states that in regions where turbulent kinetic energy production exceeds viscous dissipation in a fully-developed flow, there must be an interchange of fluid from wall

zones to the core. The secondary flow will always be toward the corner along the bisectrix in the case of non-circular ducts or along the normal toward a rough wall. Both of these are regions of high turbulence production. As will be seen in annular flow, the pipe bottom where the liquid carpet is thick and wavy is such a "rough" region and secondary flow is toward this carpet and back up the pipe walls as shown in Figure 6.2. As depicted in the figure, the secondary flow takes the form of two counter-rotating axial vortices which can sweep liquid from the bottom (or sides) to the tube top.

More concretely, Darling & McManus[35] created an annular flow analog with an asymmetrically roughened pipe carrying a single phase air flow. Their four inch pipe was machined with an eccentric internal thread having a depth of 0.125 inch at the bottom diminishing to zero at the top. Hot wire anemometer measurements revealed the flow pattern previously described. This work is significant for two reasons. First, it was found that the secondary velocity along the circumference scaled with the axial velocity and $\sin\theta$, where θ is the circumferential angle measured from the tube top. The maximum was about 4% of the average throughput velocity. Secondly, a connection between annular flow and asymmetry of wall roughness is made. As will be seen, this connection is a starting point for modeling secondary currents in horizontal annular flow.

In Laurinat's[25] analysis, he incorporates the secondary shear as a boundary condition for the film using an unknown constant, 'C_5', to be evaluated from the data. Laurinat's analysis attempts to incorporate all mechanisms but is left with several constants to fit to the data. It is difficult to conclude from this which mechanisms are

important, however Laurinat concludes secondary flow is a significant force.

Butterworth & Pulling[29] inferred that an exclusively secondary flow mechanism would result in a film flow, $\Gamma_\theta = 0$ implying that the injected dye in their experiments would go neither up nor down. Since this was not observed, secondary flow was discounted although the $\Gamma_\theta = 0$ assumption is rather dubious.

Based on a laminar film flow assumption Butterworth[36] has determined the tangential shear required to hold up a film of thickness δ:

$$-\tau_\theta = \frac{2}{3}(\rho_l - \rho_g)g\delta\sin\theta \qquad (6\text{-}7)$$

The above assumes zero flow in the film, which according to Butterworth will be true if secondary flow acts alone and the following boundary conditions apply: $\Gamma_\theta = 0$ at $\theta = 0,\pi$. These boundary conditions may be incomplete because there is nothing to prevent a net upflow resulting in drops falling from the tube top, $\theta = 0^0$. For typical film thicknesses, it is shown that τ_θ can be on the order of 20% of the axial shear. Darling and McManus[35] measured shear ratios τ_θ/τ_w of about 6% but nevertheless Butterworth concludes secondary flow is not negligible.

A major reason for the present study is to shed some light on the secondary flow controversy. It seems that many of the previous studies assume away all but one mechanism for maintaining an annular film and the data is fit by adjusting a constant. In the general case, multiple mechanisms act and modeling as such provides more freedom in fitting to the data. The strategy in the present study is as follows: By studying the onset of annular flow, the vapor velocities are below the entrainment limit, or at least the entrained mass is small. At these vapor velocities, it is expected

that wave spreading, (although believed to be a factor in maintaining annular flow) is not responsible for bringing liquid to the tube *top*. The results of Jayanti[30] support this as do the flow visualization studies of Flores[32] where it was observed at the low gas velocities in question (< 70 ft/s) that wave spreading did not progress past $\theta=90^0$. It would seem, based on the preceding arguments, that for vapor velocities less than the critical entrainment velocity, the only mechanism controlling the existence of a continuous annulus (dryout limit), is the secondary flow. Studying annular flow in this range allows evaluation of the secondary flow mechanism. A description of the experimental program follows.

6.3. Experimental Program

The experimental program was divided into two parts. Flow visualization and measurement of secondary flow in an adiabatic air-water system constituted one study. The other involved location of high quality dryout in an atmospheric steam-water system with an imposed heat flux.

6.3.1. Air-Water annular flow studies

The air-water studies done by Flores[32] involved mapping the high quality dryout boundary by visually checking for a continuous annulus in a two inch clear PVC conduit at atmospheric pressure. Verification of the presence of secondary flow (or axial vorticity) was made using a twin vorticity meter, shown sketched in Figure 6.4. In addition, the approximate magnitude of the secondary flow was measured using the same vorticity meter apparatus in a single phase air flow where the lower half of the pipe was artificially roughened by adhering small beads or sandpaper to the inside surface.

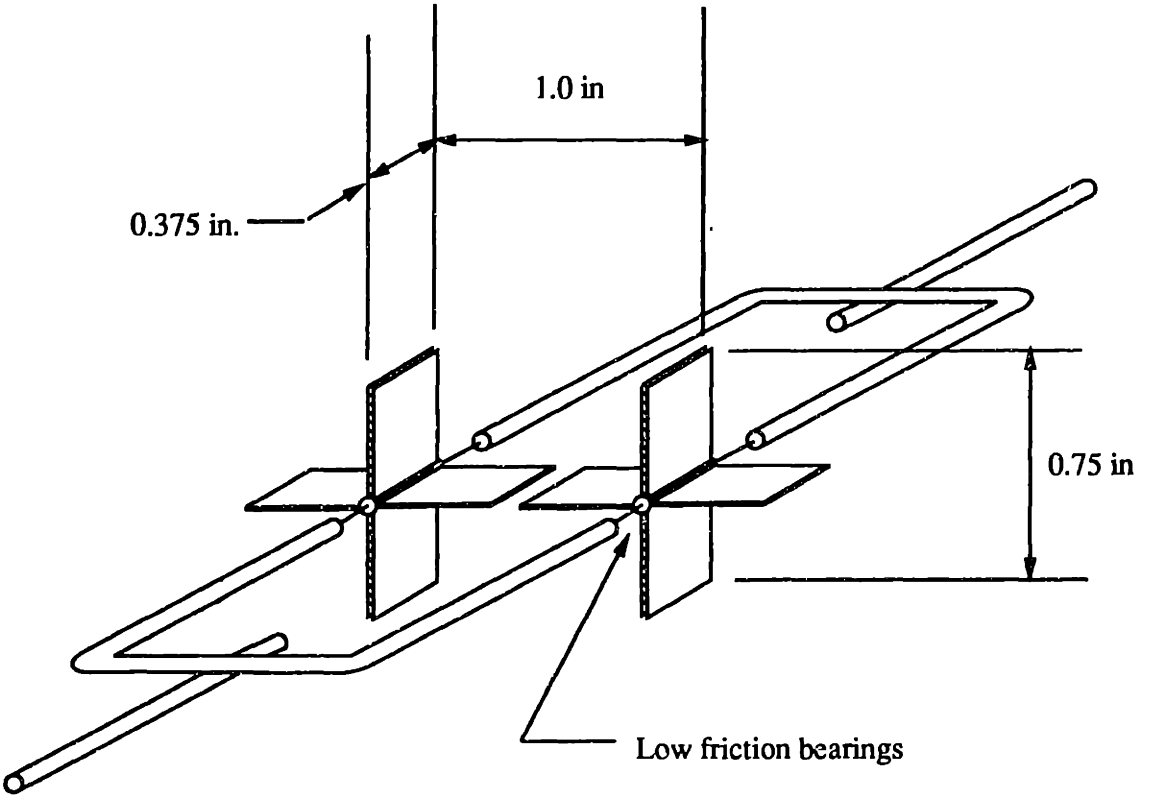

Figure 6.4: Sketch of the vorticity meter apparatus

The rotation rate of the vorticity meter was determined using a laser-detector combination as sketched in Figure 6.5. The air velocity and the surface roughness height were used as independent variables. The specific details of the experiments are given by Flores[32] and the results will be discussed in the next chapter.

6.3.2. Diabatic Annular Flow Experiments

The diabatic high quality experiments were conducted in the same system used for the intermittent dryout study. To achieve high quality, the saturated laboratory steam was piped directly into the system. A specially fabricated fitting to allow delivery of liquid as an annulus and vapor in the pipe center region was used as an inlet condition. This gave the annular flow a "head start" in developing. The flow developed for another 90 pipe diameters to the point of temperature measurement in the heated test section. For these high quality experiments, only one differential thermocouple, located at the midpoint of the test section, was used to determine the thermal state. A large steady state differential temperature or an unsteady differential temperature was interpreted as a dryout condition. For a fixed heat flux, the liquid rate was held fixed while the vapor rate (measured with a standard ASME orifice meter[18]) was changed (either an increase or a decrease) until a change of state was realized. This delineated the dryout boundary. The maximum liquid rate used corresponded to the onset of slug flow, since this was not the regime of interest in the present study. The lower limit was determined by when the vapor rate could no longer be increased and dryout prevailed. The dryout boundary was found at heat fluxes of 37 kW/m^2 and 146 kW/m^2.

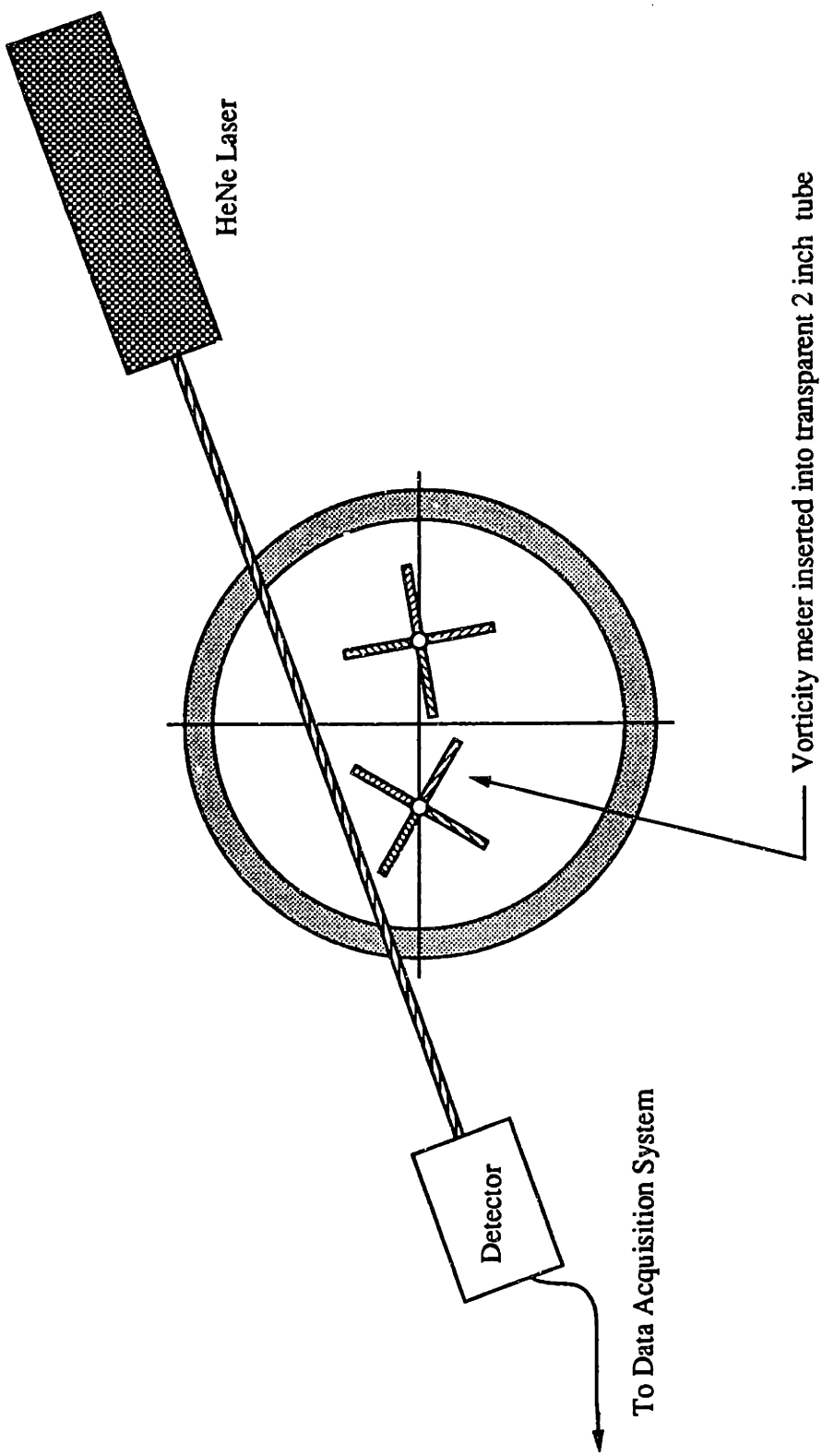

Figure 6.5: Optical system used with vorticity meter

CHAPTER 7

Experimental Results and Modeling of High Quality Dryout

7.1. Introduction

The range of vapor velocities encountered where the dryout boundary was located in the diabatic experiments suggest that the entrainment/deposition mechanism does not play an important role in the maintenance of the liquid annulus near the dryout limit. Flow visualization did not show an appreciable concentration of droplets in the core. Consequently, it is believed that the secondary flow is the only mechanism available to keep the tube top wet and is the only factor that need be considered in dryout modeling.

The results of Darling & McManus[35] suggest that the asymmetry of the pipe wall roughness gives rise to secondary flow. The resulting flow pattern indicated two counter-rotating axial vortices where the flow was up at the walls and down through the vertical centerline. The net result was a nominal secondary flow velocity of about 4% of the average throughput velocity. These results would seem to imply that this flow pattern is related to the roughness distribution. The connection to annular flow is made in that surface waves induced by the high speed vapor core have a larger

amplitude where the film is thicker. In other words, the Darling & McManus experiment essentially mimics annular flow. Because in that the experiment, the walls are stationary, it may inferred that the relative motion of the annular film (where the bottom moves most rapidly) is not a principal effect producing the secondary flow. Typically, the slip ratio between the gas core and the liquid film in an air-water, atmospheric pressure, annular flow is on the order of six, so the liquid may be treated as stationary in an analysis such as this.

There are numerous complex factors involved in predicting the liquid distribution in horizontal annular flow. Two turbulent phases are present with a free wavy interface between them for which a boundary condition is not well defined. The geometry is asymmetric. Turbulence modeling for each phase will be required. Neither the film thickness distribution, nor the relation between "effective" roughness and film thickness is known in this problem. Many modeling assumptions will thus be employed in order to simplify the problem and give a result which captures the most important physical aspects of the problem and depends on the most tangible parameters.

7.2. Analysis of the core flow

The overall approach taken will be to divide the two phase flow into two single phase flows. First, the vapor core flow will be analyzed, the goal being to determine the interfacial shear in the circumferential direction, τ_θ on the liquid film. The effect of this shear on the flow rate of the liquid film will then be analyzed.

Due to the asymmetry of the gas core flow (induced by the roughness distribution), the turbulence equations are 3-D with many intractable terms present. However,

it is known from direct visualization of annular two-phase flow that nearly all of the liquid in the pipe resides at bottom. For example, Butterworth[26] has found the film thickness ranging from about 3.5 mm at the pipe bottom to less than 0.2 mm at the top in a 31.8 mm diameter pipe. The pipe diameter and precise flow conditions will of course affect these numbers which are only given to illustrate. Then, in order to make the problem more tractable, the pipe is essentially nodalized into upper (smooth) and lower (rough) halves. This nodalization removes any resemblance of a pipe geometry and the scheme is essentially 2-D. It is argued that the sharp difference in surface characteristics between the top and bottom will give rise to the secondary flow, so that solution of the the entire field is unnecessary.

Given the two nodes with their differing properties, it is desirable to form the secondary flow calculation as a difference in some quantity between the top and bottom. However, it is desired to a have a parameter that is physically based as well. For example, the difference in average velocity, ΔU_{ave} might be used. This way, as the roughness difference approaches zero, the flow field approaches a symmetric type and no secondary flow results.

Associated with each half pipe, is a turbulence intensity, which is a measure of the magnitude of the velocity fluctuation. Considering the y-component (normal to the wall) of the velocity fluctuation, v', one might argue that net motion in the core of the pipe may be dictated by the difference in the magnitude of these fluctuations. This statement gives no indication of the direction of motion but this was discussed in section 6.2.6 of the last chapter. Then let us postulate that the secondary velocity (at least in the core) is proportional to the difference in the fluctuation magnitude of v'. That

is,

$$v_{sec} = \text{Const}(|v'_b| - |v'_t|) \tag{7-1}$$

It is essential to relate the unknown fluctuating quantities to knowns in the problem. Typically, the y-component (radial) fluctuation is of the same order as the x-component (axial). So,

$$|v'| \simeq |u'| \tag{7-2}$$

Now, the friction velocity is related to these,

$$u_* \simeq \sqrt{|u'v'|} \simeq \sqrt{v'^2} = |v'| \tag{7-3}$$

where u_* is the friction velocity defined by $\sqrt{\tau_w/\rho_g}$. Therefore, we hypothesize that the secondary flow may be expressed as

$$v_{sec} = C_*(u_{*_b} - u_{*_t}) \tag{7-4}$$

This formulation has the desired characteristic that it goes to zero as the roughness difference goes to zero. Also, the friction velocity is typically on the order of a few percent of the average axial velocity, so one might expect a constant, C_* on the order of unity based on the measurements of Darling & McManus.[35] The value of this constant is to be extracted from fitting to the data.

The calculation of the upper and lower friction velocities comes from the turbulent pipe flow relations. Associated with each half pipe is a sand roughness, k_s an average velocity, U_{ave}, a corresponding Reynolds number, Re and a friction factor, λ. With these inputs, the approximate velocity profile in each half can be calculated using turbulent pipe flow relations while the centerline velocities are matched.

For a 2-D channel flow, as is essentially modeled here, it is known that the maximum of the axial velocity profile will be biased toward the smooth wall.[18] A sketch

of what this profile might look like is shown in Figure 7.1. The top and bottom halves act independently, with the exception of the common centerline velocity. So, taking the centerline velocity as the maximum is not strictly true, but given the degree to which the problem has been simplified to this point, it is inappropriate to calculate the velocity field more precisely than this. The velocity distributions for each half are calculated iteratively with initial specifications of the roughness and centerline velocity, and a guess of the friction factor.

The turbulent pipe flow relations are now presented. The friction factor λ, is a function of both the roughness and the Reynolds number given by the Colebrook[37] correlation, which is based on data over the roughness range up to $k_s/R = 0.015$:

$$\frac{1}{\sqrt{\lambda}} = 1.74 - 2.0 \log\left[\frac{k_s}{R} + \frac{18.7}{Re\sqrt{\lambda}}\right] \tag{7-5}$$

The use of this correlation for roughnesses much larger than this limit is questionable.

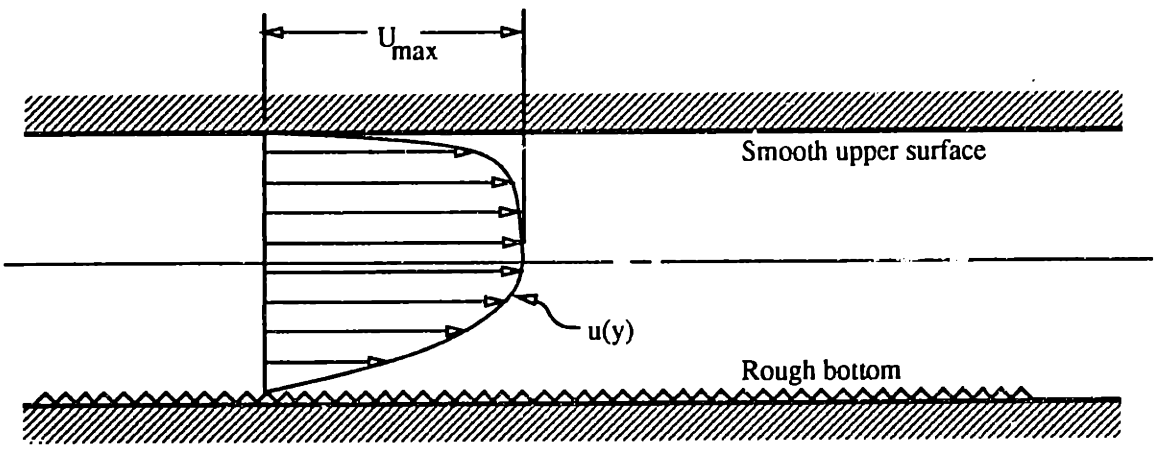

Figure 7.1 Asymmetric turbulent velocity profile in half rough pipe

The Reynolds number above is based on the full pipe diameter:

$$Re = \frac{U_{ave}D}{\nu_g} \tag{7-6}$$

where the calculation of U_{ave} requires integration of the universal velocity profile for pipes:

$$u(y) = U_{cl} - \frac{u_*}{\kappa}\ln\frac{R}{y} \tag{7-7}$$

The result of this integration and averaging is[38]

$$U_{ave} = U_{cl} - 3.75u_* \tag{7-8}$$

where u_* is the friction velocity which is defined through the wall shear stress by the following:

$$u_* = \sqrt{\frac{\tau_w}{\rho_g}} \tag{7-9}$$

From a force balance between pressure drop and wall shear, it can be shown that:

$$u_* = \sqrt{\frac{\lambda}{8}}U_{ave} \tag{7-10}$$

Finally, combining 7-10 and 7-8 gives

$$U_{ave} = \frac{U_{cl}}{1 + 3.75\sqrt{\lambda/8}} \tag{7-11}$$

So, for a given wall roughness and centerline velocity, one makes an initial guess at the friction factor and iteratively calculates the average velocity, Reynolds number, and friction factor. Typically, this algorithm converges rapidly, achieving sufficient accuracy within five iterations. Upon convergence, one calculates u_* from equation 7-10 for use in equation 7-4. This procedure was applied to the half roughened pipe experiments described in the previous chapter, the results of which are presented next.

7.3. Results for the half roughened pipe

The results of the secondary flow measurements found from the half roughened pipe[32] are plotted in Figure 7.2 as the normalized secondary flow vs. roughness. Also shown is the secondary flow prediction using equation 7-4 and the algorithm of the previous section after least squares fitting to obtain the constant. The model, using $C_* = 0.52$ works reasonably well. Data over a wider range of roughness might establish the credibility of this fit. However, in this range of roughness, the secondary flow will be taken as

$$v_{sec} = 0.52(u_{*_b} - u_{*_t}) \tag{7-12}$$

7.4. Model for annular flow

7.4.1. Roughness specification

To implement this approach, a value for k_s has to be assigned. For the single phase air experiments described in the last chapter, k_s is given the value of the sand roughness used and the procedure in the previous section is straightforward.

In the case of two-phase flow, true sand roughness does not exist, and the liquid distribution must be indirectly connected to k_s. Two approaches have been attempted: The surface perturbations (waves) are given an equivalent sand roughness value through the amplitude. The amplitude of the waves is not known, but Wallis[33] makes the assumption that it is proportional to the liquid level, h. Therefore it is assumed that:

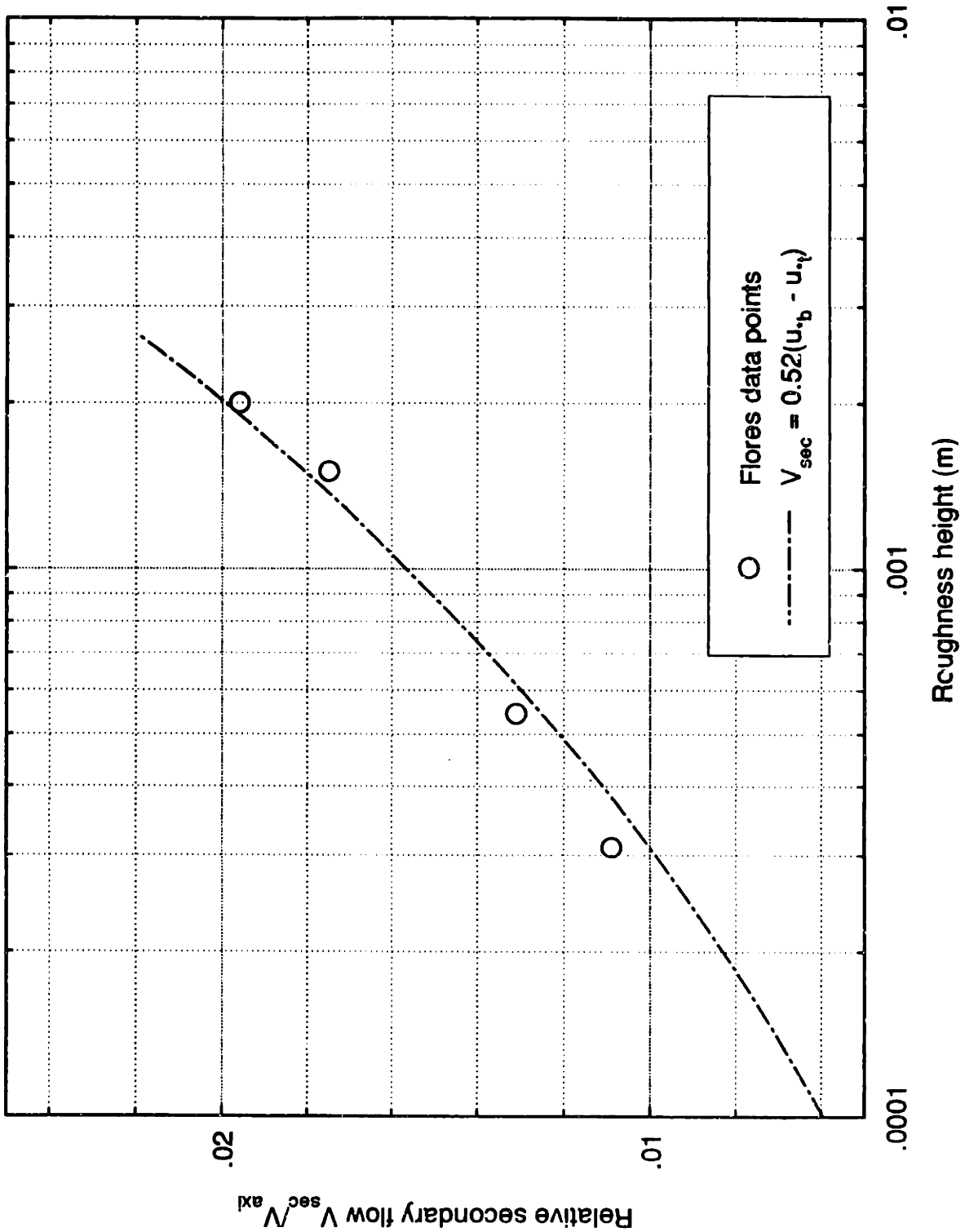

Figure 7.2: Relative secondary flow vs. roughness height

$$k_s = \text{const}(h) = C_h\left[\frac{h}{D}D\right] \tag{7-13}$$

where h/D is the normalized liquid level and is a parameter in the problem. Here, it is assumed that all the liquid resides at the pipe bottom. The roughness is then used in the Colebrook correlation for friction factor.

The second method is to circumvent the use of of k_s and calculate the friction factor directly. Wallis[33] has successfully correlated film thickness in annular flow with friction factor by the following:

$$C_{f_i} = 0.005(1 + 300\delta/D) = 0.005(1 + 75(1 - \alpha)) \tag{7-14}$$

where C_{f_i} is the interfacial friction factor related to lambda by $\lambda = 4C_{f_i}$ so that

$$\lambda = 0.02(1 + 300\delta/D) \tag{7-15}$$

The above correlation has been successful for many data sets which include horizontal flow where δ is not uniform, so it may be well founded to use this here. The thickness δ is then taken as h.

7.4.2. Induced circumferential shear

The relationship between the induced force and the film flow is needed. The next part of the problem to be addressed is the connection between the secondary flow and the *force* holding up liquid or bringing it to the tube top. It is tempting to say that the core imparts a shear stress on the film in the form:

$$\tau_i \approx \rho_g v_{sec}^2 \tag{7-16}$$

However, this is incorrect because the stress is intimately coupled to the axial velocity. Referring to Figure 7.3, it is seen that the direction of the shear force is in the direction of the vapor velocity, which is the vector sum of the axial and secondary

components. The magnitude of this stress is given by:

$$\tau = \tfrac{1}{2}C_f\rho_g U^2 \tag{7-17}$$

The component of this shear force in the circumferential (secondary) direction is scaled by the factor v_{sec}/U so that,

$$\tau_i = \tfrac{1}{2}C_f\rho_g U\, v_{sec} \tag{7-18}$$

Since it is expected that the secondary velocity is a small fraction of the axial velocity, the small angle approximation may be employed such that,

$$\tau_i = \tfrac{1}{2}C_f\rho_g \bar{u}_{axial} v_{sec} = \tfrac{1}{2}C_f\rho_g \bar{u}_g v_{sec} \tag{7-19}$$

7.4.3. Dryout criterion

Under flow conditions where the tube top is now depleted of fluid, insufficient film flow rate is responsible. Therefore, the dryout criterion is a condition on the film flow rate. The required film flow rate up the tube wall will be dictated by the applied heat flux. From an energy balance, it can be shown that the necessary film flow rate (up the wall) is given by:

$$\Gamma_\theta = \frac{q''D\theta}{2\rho_l h_{fg}} \tag{7-20}$$

where θ is measured from the tube top. As discussed in the previous chapter, visual observations indicate an ample supply of liquid up to the $\theta = 90^0$ point (tube side) due to the action of wave spreading. The region of concern where the heat flux is liable to dry out the liquid film is in the upper half. Thus, the maximum flow rate required is at $\theta = 90^0$ and equation 7-20 becomes

$$\Gamma_\theta(\theta=90^0) = \frac{q''D\pi}{4\rho_l h_{fg}} \tag{7-21}$$

This flow requirement must be met under the given flow conditions to prevent dryout.

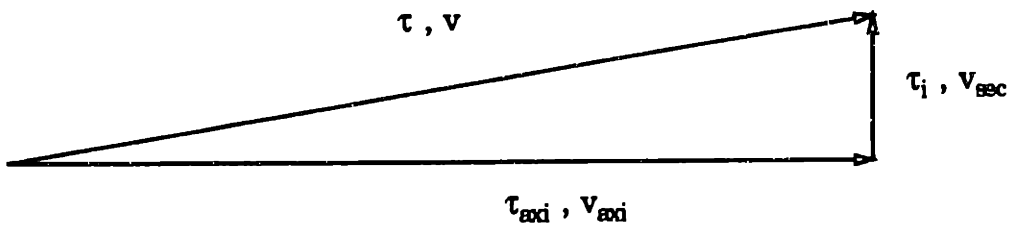

Figure 7.3: Relation between circumferential shear and secondary flow

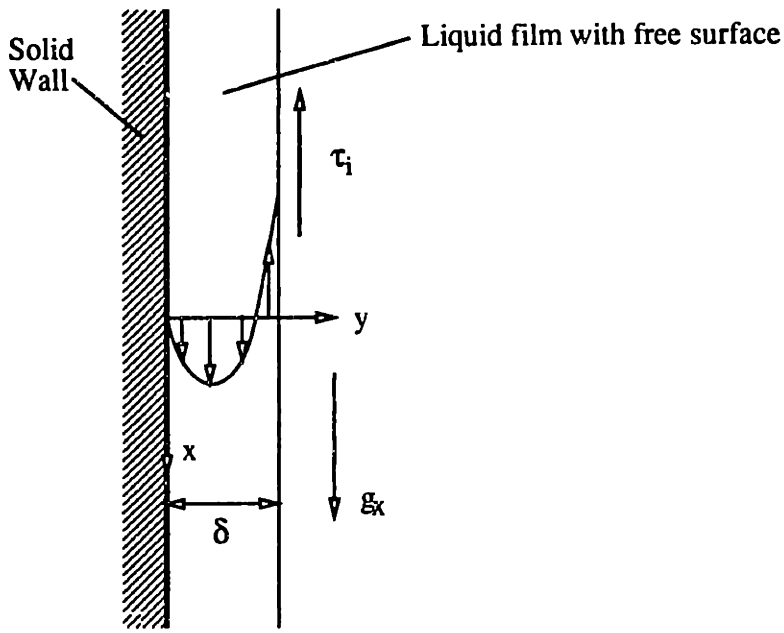

Figure 7.4: Nomenclature for laminar and turbulent film flow analysis

7.4.4. Laminar film analysis

Consider the sketch shown in Figure 7.4 which shows a free surface film on a vertical surface under the influence of gravity and interfacial shear. The positive x direction is down while y is measured from the solid surface. For the moment, only the vertical is considered where this essentially represents the side of the pipe, $\theta=90^0$. The problem can be generalized by generalizing the magnitude of the gravity force, the interfacial shear stress and the film flow requirements. This is addressed in Appendix D. The following assumptions are made:

a) The flow is steady.

b) Inertial effects are negligible.

c) The free surface is smooth; the thickness, δ is uniform.

d) There is no streamwise pressure gradient.

The momentum equation reduces to:

$$g_x + \nu_l \frac{d^2u}{dy^2} = 0 \tag{7-22}$$

Integrating this twice subject to the no-slip condition at y = 0 and the interfacial shear condition at $y = \delta$ gives the following:

$$u(y) = C_1 y - \frac{g_x y^2}{2\nu_l} \tag{7-23}$$

where

$$C_1 = \frac{g_x \delta}{\nu_l} - \frac{\tau_i}{\rho_l \nu_l}$$

The film flow rate is found from integrating the velocity profile:

$$\Gamma_\theta = \int_0^\delta u(y)dy \tag{7-24}$$

which becomes

$$\Gamma_\theta = \frac{g_\pi \delta^3}{3\nu_l} - \frac{\tau_i \delta^2}{2\rho_l \nu_l} \tag{7-25}$$

For thick films, the cube term dominates and the flow is positive (downward, in the direction of gravity) and for thin films, the flow is up. So, given an interfacial shear τ_i, the flow rate and film thickness are intimately related. For a fixed interfacial shear of $\tau_i = 1$ Pa, the flow vs. film thickness is shown in Figure 7.5. As seen, if the film is too thick, a positive (downward) flow results. The maximum upflow occurs at a certain thickness found from

$$\frac{\partial \Gamma_\theta}{\partial \delta} = \frac{g\delta^2}{\nu_l} - \frac{\tau_i \delta}{\rho_l \nu_l} \equiv 0 \tag{7-26}$$

or

$$\delta = \frac{\tau_i}{\rho_l g} \tag{7-27}$$

which says that for a given shear, the thickness to achieve maximum upflow is such that the interfacial shear exactly balances the film's weight. Thus, the wall shear (circumferentially) is zero and only upflow results. This is consistent with findings of Hewitt & Wallis[39] which show that simultaneous up and down flow within a vertical, free surface film is unstable.

Another way to justify the condition of maximum up flow can be made. If a large liquid flow is available at the pipe side ($\theta = 90^0$), then the interfacial shear stress will carry up only its maximum. Additional flow will result in fluid build up which will fall back (see Figure 7.5). Based on visualizing the wave spreading in annular

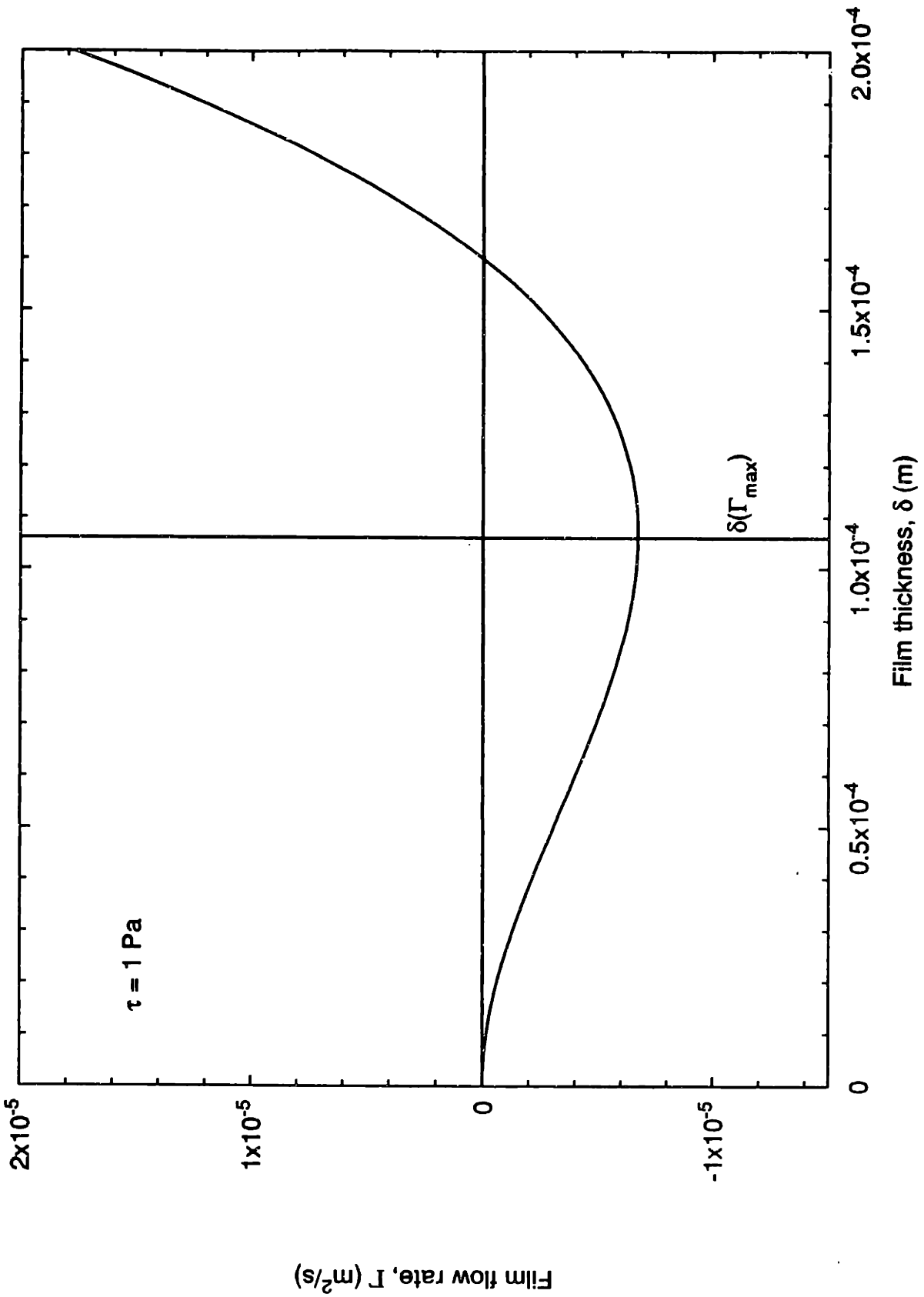

Figure 7.5: Film flow rate vs. thickness for laminar film

flow, it would appear more than sufficient fluid flow is supplied to the pipe side. Thus, the condition of maximum upflow and zero wall shear are consistent and physically realistic.

The laminar approach is a useful way to illustrate the problem. However, visual inspection of the film would support the case for a turbulence analysis which is given next.

7.4.5. Turbulent film analysis

Using the same sketch and set of assumptions (excluding the inertia free assumption) as for the previous analysis (Fig. 7.4), the momentum equation becomes,

$$g_x + \frac{\partial}{\partial y}\left[\nu_{eff}\frac{\partial \bar{u}}{\partial y}\right] = 0 \tag{7-28}$$

where the effective viscosity is given by:

$$\nu_{eff} = \nu + \nu_t \tag{7-29}$$

The turbulence modeling involves using an appropriate expression for the eddy viscosity, ν_t. Commonly, the film is treated as if it were part of a single phase pipe flow. Then the axial universal velocity profile applies;

$$w(y) = \frac{u_*}{\kappa}\ln\left[\frac{u_* y}{\nu_l}\right] + \text{const} \tag{7-30}$$

Then, the eddy viscosity can be expressed as:

$$\nu_t = u_* \kappa y \tag{7-31}$$

where u_* is the friction velocity associated with axial wall shear, and κ is the von Karman universal constant. Essentially, we are implying that the turbulence is isotropic by using the viscosity associated with $\partial\bar{w}/\partial y$ gradients for $\partial\bar{u}/\partial y$ gradients. Integrating

the momentum equation and multiplying by ρ_l gives

$$\left[-\rho_l g_x y + \rho_l C_1 = \mu_{eff}\frac{\partial \bar{u}}{\partial y}\right]_\delta = -\tau_i \tag{7-32}$$

where the integration constant is evaluated from the circumferential shear condition at the interface:

$$C_1 = g_x\delta - \tau_i/\rho_l \tag{7-33}$$

Integrating again gives:

$$u(y) = -\frac{g_x y}{u_*\kappa} + \frac{A}{u_*\kappa}\ln(\nu + u_*\kappa y) + C_2 \tag{7-34}$$

where

$$A = C_1 + g_x\nu/u_*\kappa \tag{7.34-a}$$

For the expected film thicknesses and the properties of water, it can be shown that C_1 is much larger than the second term in A above. Evaluating the constant C_2 from the no-slip condition at the wall gives,

$$C_2 = -\frac{A}{u_*\kappa}\ln \nu \tag{7-35}$$

so the turbulent velocity profile becomes:

$$u(y) = -\frac{g_x y}{u_*\kappa} + \frac{g_x\delta - \tau_i/\rho_l}{u_*\kappa}\ln\left[\frac{\nu + u_*\kappa y}{\nu}\right] \tag{7-36}$$

The film flow rate Γ_θ is given by:

$$\Gamma_\theta = \int_0^\delta u dy \tag{7-37}$$

Performing the integration yields:

$$\Gamma_\theta = -\frac{g_x\delta^2}{2u_*\kappa} + \frac{(\rho_l g_x\delta - \tau_i)\nu}{\rho_l u_*^2\kappa^2}\left[(1 + Re_\tau)\ln(1 + Re_\tau) - Re_\tau\right] \tag{7-38}$$

where Re_τ is the Reynolds number based on the friction velocity and the film

thickness:

$$Re_\tau = \frac{u_* \kappa \delta}{\nu} \tag{7-39}$$

The flow rate equation above cannot explicitly be solved for either the required interfacial shear stress τ_i or the thickness corresponding to maximum upflow because δ appears in the log term and because τ_i and u_* have dependency on δ that make the expression quite cumbersome. These dependencies will be discussed in the next section which describes the method of solution. However, all the necessary building blocks are present to calculate the high quality dryout bound which requires numerical solution.

7.5. Algorithm for solving high quality dryout boundary

To determine the dryout boundary, two quantities are used as parameters: the liquid level and the vapor core centerline velocity, U_{cl}. The secondary flow can be calculated using either the Colebrook formulation for friction factor requiring the iteration scheme given in section 7.2 or the Wallis approach which gives friction factor independent of Reynolds number. Thus,

$$\lambda_\tau = 0.02 \tag{7-40}$$

$$\lambda_b = 0.02(1 + 300h/D) \tag{7-41}$$

The corresponding friction velocities are computed from equation 7-10 and the circumferential vapor velocity is then found from equation 7-12.

With the average and circumferential velocities fixed, the maximum upflow from equation 7-38 can be found by sweeping through increasing film thickness. This affects both τ_i and u_* for the film The friction velocity is found from its definition:

$$u_* = \sqrt{\frac{\tau_w}{\rho_l}} \tag{7-42}$$

It is now assumed that the wall shear stress τ_w is equal to the axial interfacial shear, which is the case for a steady, fully developed, thin film.

$$\tau_{w_{axial}} = \tau_{i_{axial}} = \tfrac{1}{2} C_f \rho_g u_g^2 \tag{7-43}$$

The skin friction coefficient associated with a wavy annular film is function of the thickness as correlated by Wallis[33]

$$C_{f_i} = 0.005(1 + 300\delta/D) \tag{7-44}$$

Finally, the film flow is calculated from equation 7-38. The thickness, δ is increased until the maximum upflow is reached. This thickness and flow rate are the solutions for the given conditions. If the flow is insufficient based on the imposed heat flux (equation 7-21), then the vapor centerline velocity is incremented (which effectively increases j_g) and the process repeated. When the flow rate reaches that required, the annular transition point along that liquid level line has been reached.

For use on the superficial velocity map, the average core velocity and liquid level are converted to a j_g , j_l pair. Through the Martinelli parameter, X, (see Figure 2.2) the quality is found from the chosen h. The superficial vapor velocity is less than average velocity because the flow area is smaller than the pipe area. These are related by

$$j_g = \frac{u_g A_g}{A} \tag{7-45}$$

where A_g is a geometric function of liquid level, h:

$$A_g = \left[1 - \frac{1}{\pi} \text{Arccos}\left(1 - \frac{2h}{D} \right) \right] \frac{\pi D^2}{4} \tag{7-46}$$

Finally, the liquid velocity is found from thermodynamic considerations:

$$j_l = \frac{\rho_v}{\rho_l}\frac{1-x}{x}j_g \tag{7-47}$$

A new liquid level is then calculated and so on to give the dryout bound. For any quality, the necessary average vapor velocity can be calculated using the method outlined above. This defines the high quality dryout limit.

7.6. Results

7.6.1. Experimental Dryout Points

The bounding points for dryout associated with the SW-A transition, were determined using the diabatic system as described in the last chapter for heat fluxes of 37 kW/m^2 and 146 kW/m^2. The results are plotted in Figures 7.6 and 7.7. Also shown are the hydrodynamic boundaries computed from the Taitel & Dukler[1] analysis. For the lower heat flux (Figure 7.6), one can see a continuous boundary that lies essentially along the Taitel & Dukler stratified-annular boundary. The upper points, however have a positive slope and lie near the line of h = 0.5. Use of higher liquid rates than those shown resulted in a slug flow entering the test section and thus outside the range of interest. Limitations on the available steam flow prevented locating bounding points for lower liquid rates.

Switching to the data for the high heat flux, it appears there is more detail to the dryout bounds. The negative sloping bound is very nearly in the same location as for the lower flux and there is the same trend of slope reversal for higher liquid rates. This positive sloping dryout bound seems to lie along a constant quality line of x =

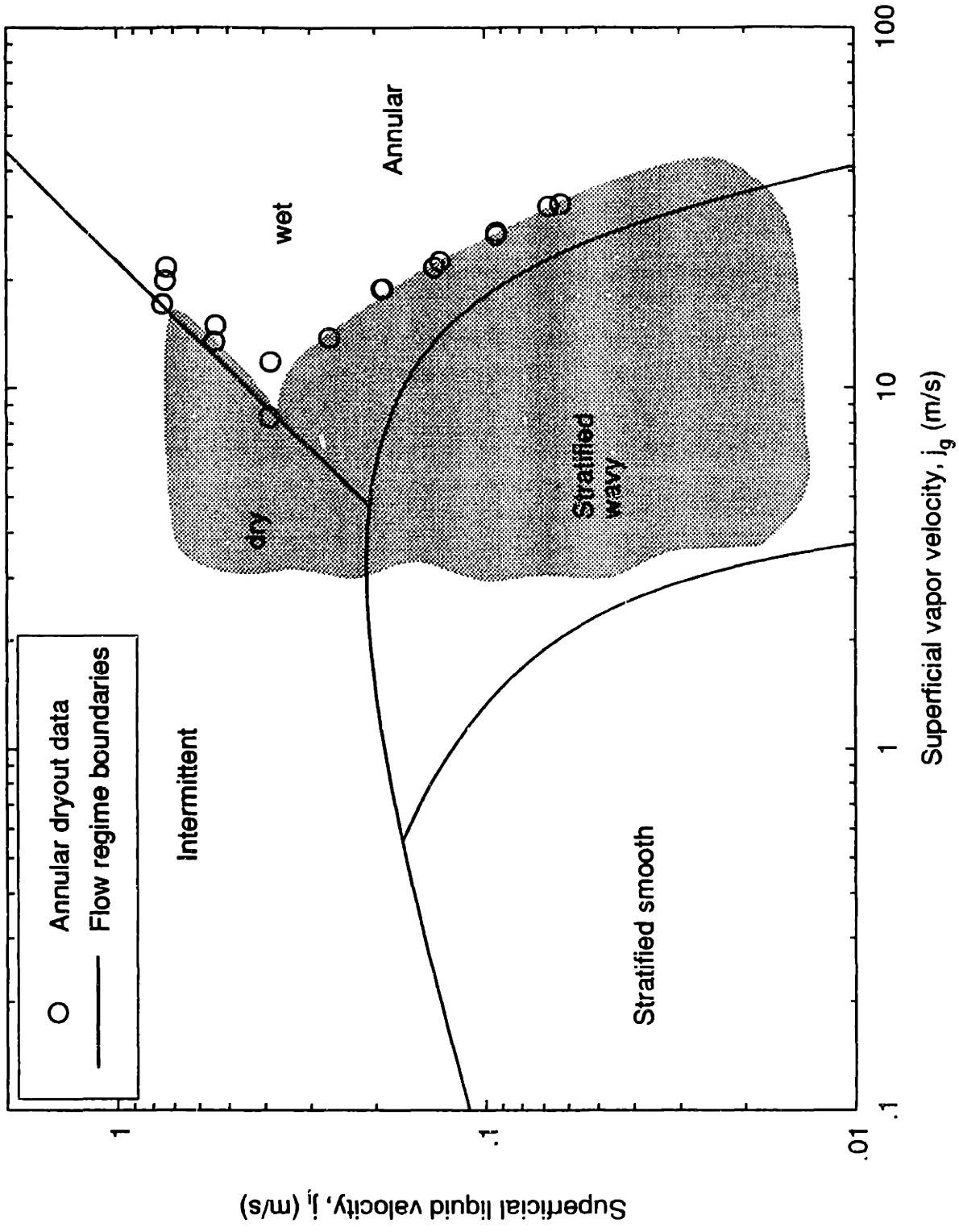

Figure 7.6: Stratified - annular transition for $q'' = 37$ kW/m^2

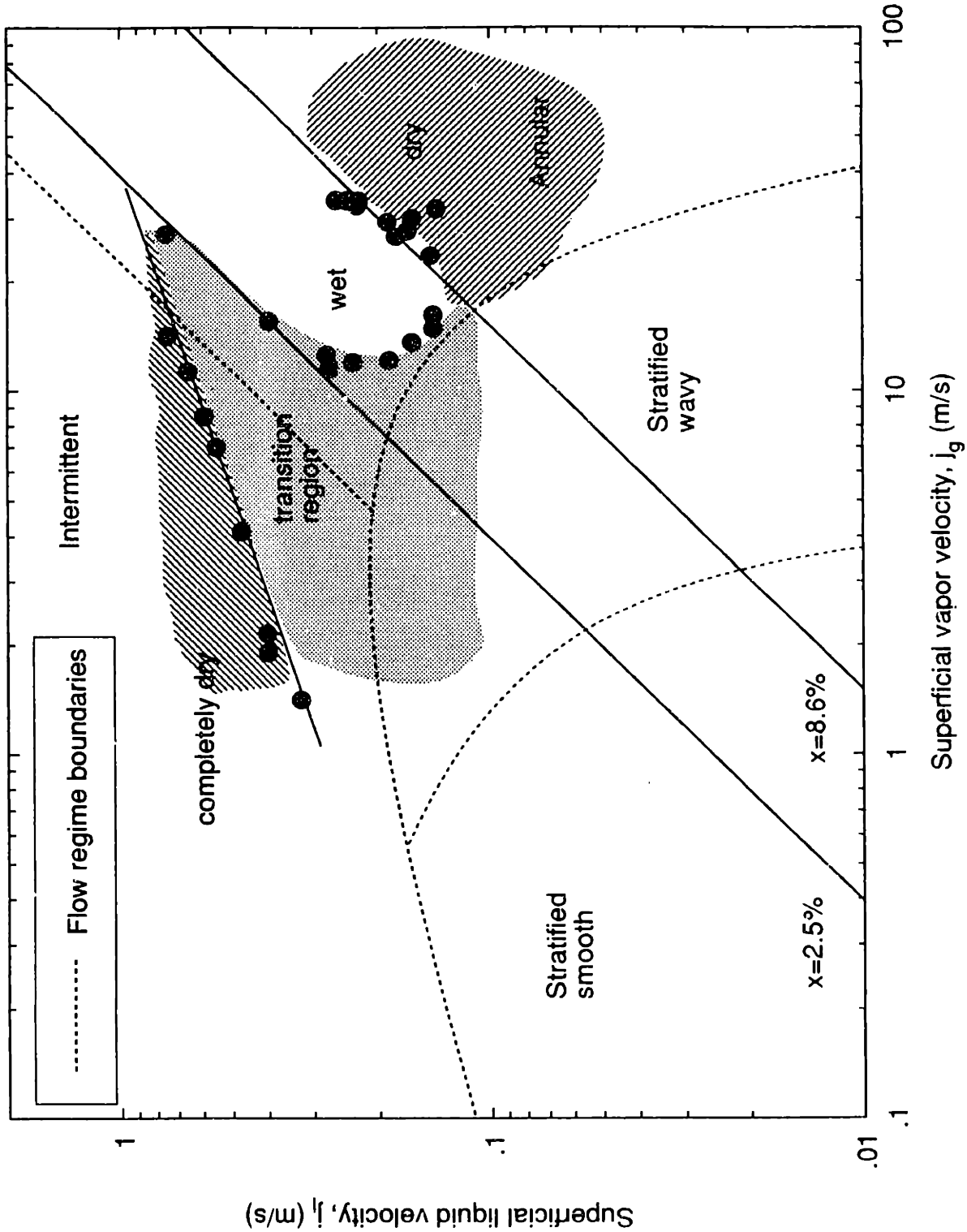

Figure 7.7: Stratified - annular transition for q" = 146 kW/m^2

2.5% which is close to value of h = 0.5 at atmospheric pressure. This line is the true bound and should not be confused with the bound to left. The region between these two bounds labeled "transition region" was characterized by temperatures that were generally low but showing occasional signs of a rapid rise. To the left of the left boundary the tube top temperatures were steadily high. The lower heat flux data apparently did not indicate this behavior. This might be because the lower heat flux makes the system respond less dramatically to hydrodynamic perturbations so temperature fluctuations are less detectable. The final bound in Figure 7.7 is the very high quality positive slope region along the line x=8.6%. Increases in vapor flow rate beyond this bound invited rather rapid temperature rises. This bound seems to be along a line of constant quality and is thought to correspond to a Biasi[24] type burnout, but for horizontal tubes. The physical mechanism responsible is unknown but at these vapor rates the liquid level in the pipe is quite low even though the liquid flow rate is fixed so, there may not be enough liquid to keep all of the tube top wet.

7.6.2. Predicted Dryout Boundaries

In Figure 7.8, the predicted dryout boundary for the case of turbulent film flow is shown. The vapor core flow is based on the Colebrook correlation for friction factor where C_h is a parameter (see equation 7-13). The secondary flow was calculated based on $C_* = 0.52$ (see equation 7-12). This method grossly overpredicts the superficial vapor velocity at the annular transition even for an equivalent sand roughness equal to four times the liquid level and was not used subsequently.

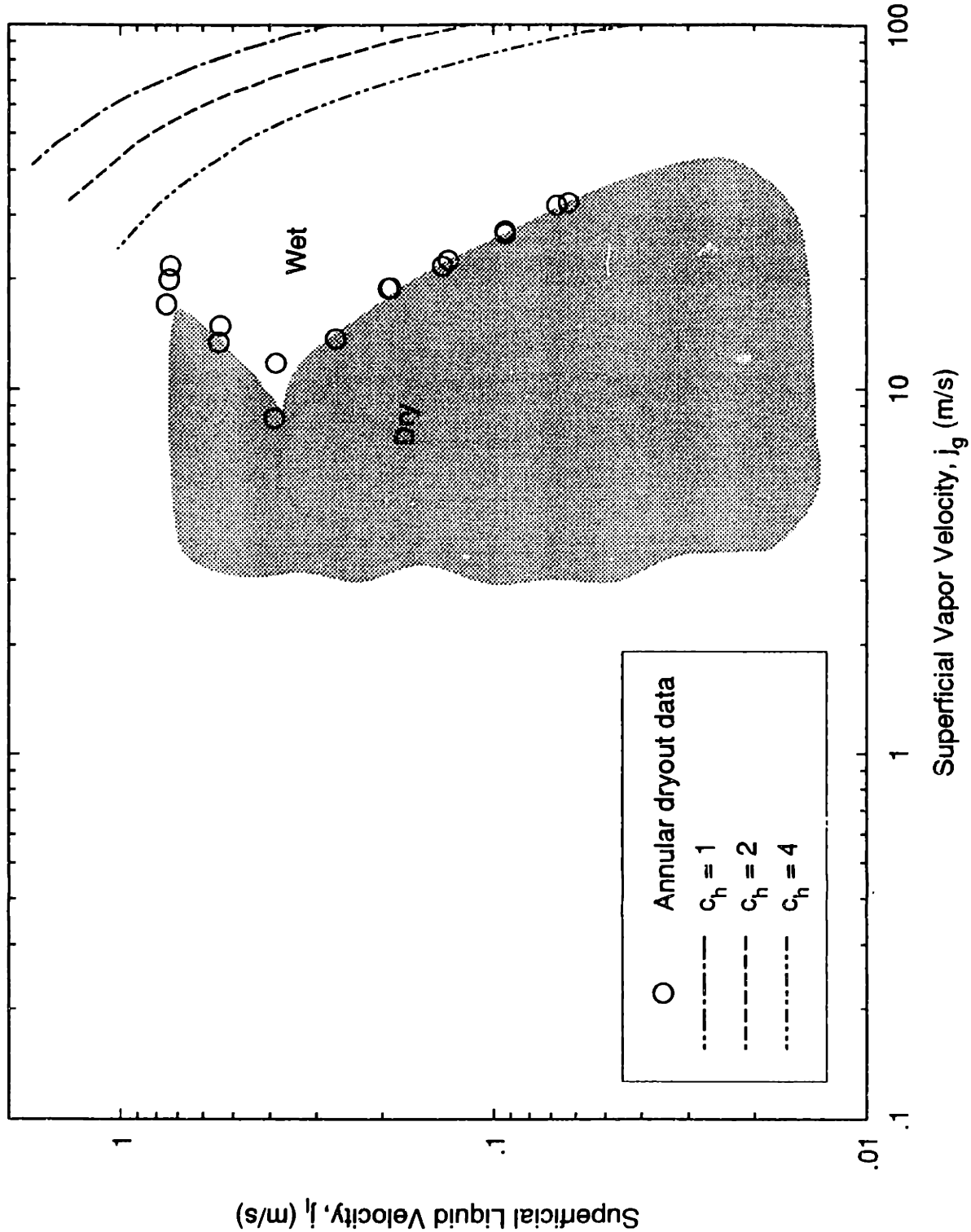

Figure 7.8: Comparison of annular transition model with $q'' = 37$ kW/m^2 data

In Figure 7.9, the predicted dryout boundaries for both the laminar and turbulent analysis are shown along with the dryout points for $q'' = 37\ kW/m^2$. The vapor analysis was the same for both models, employing the Wallis approach for top and bottom friction factors, where $C_* = 0.52$. The solutions were generated only up to a liquid level of $h = 0.5$ which according to Taitel & Dukler is the transition to slug flow. Both model curves have the correct general trend; possessing a negative slope of almost the correct magnitude. It will be recalled that $C_* = 0.52$ came from fitting to data obtained from a single phase air flow in a half roughened tube. Since it may be argued that this case is quite different in the roughness geometry and magnitude, one may make a case for fitting the laminar film model using a different constant. Figure 7.10 shows the results of this. Use of a constant, $C_* = 2$ brings the data and model more into alignment.

To check the generality of this fitted constant, comparison was made at the higher heat flux. The results for $q'' = 146\ kW/m^2$ are shown in Figure 7.11 where the Wallis friction factor was used and $C_* = 2$. Here the model boundaries overpredict the points associated with the SW-A transition even though the larger value $C_* = 2$ was used. Comparison of Figures 7.10 and 7.11 show that the model predictions move to the right for the higher heat flux, yet the data are essentially fixed. The model prediction has a heat flux dependence not seen in the data.

7.7. Discussion

Though good agreement was not obtained for any of the attempted modeling, some comments are in order concerning which model elements are most appropriate.

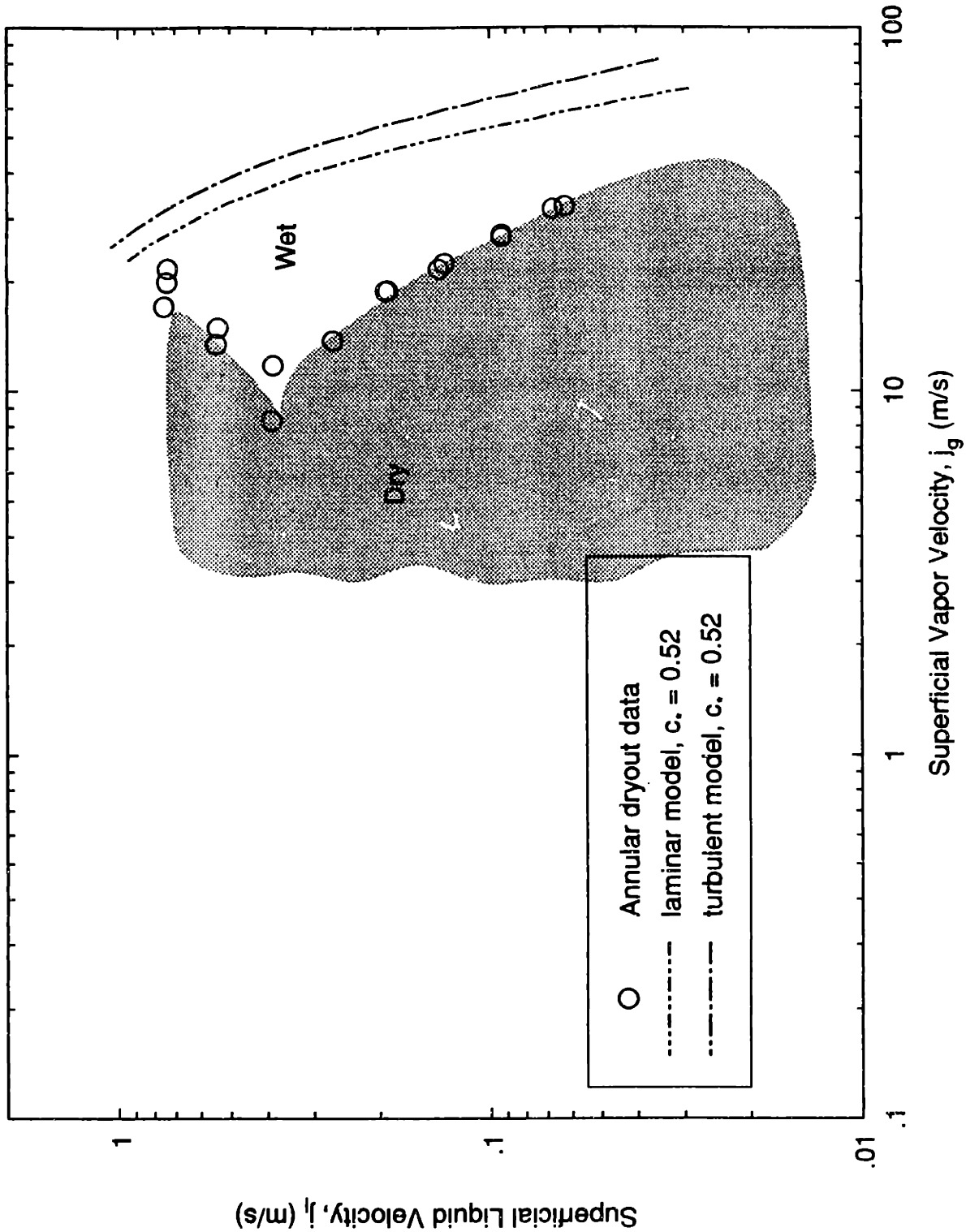

Figure 7.9: Comparison of laminar and turbulent models with $q'' = 37$ kW/m^2 data

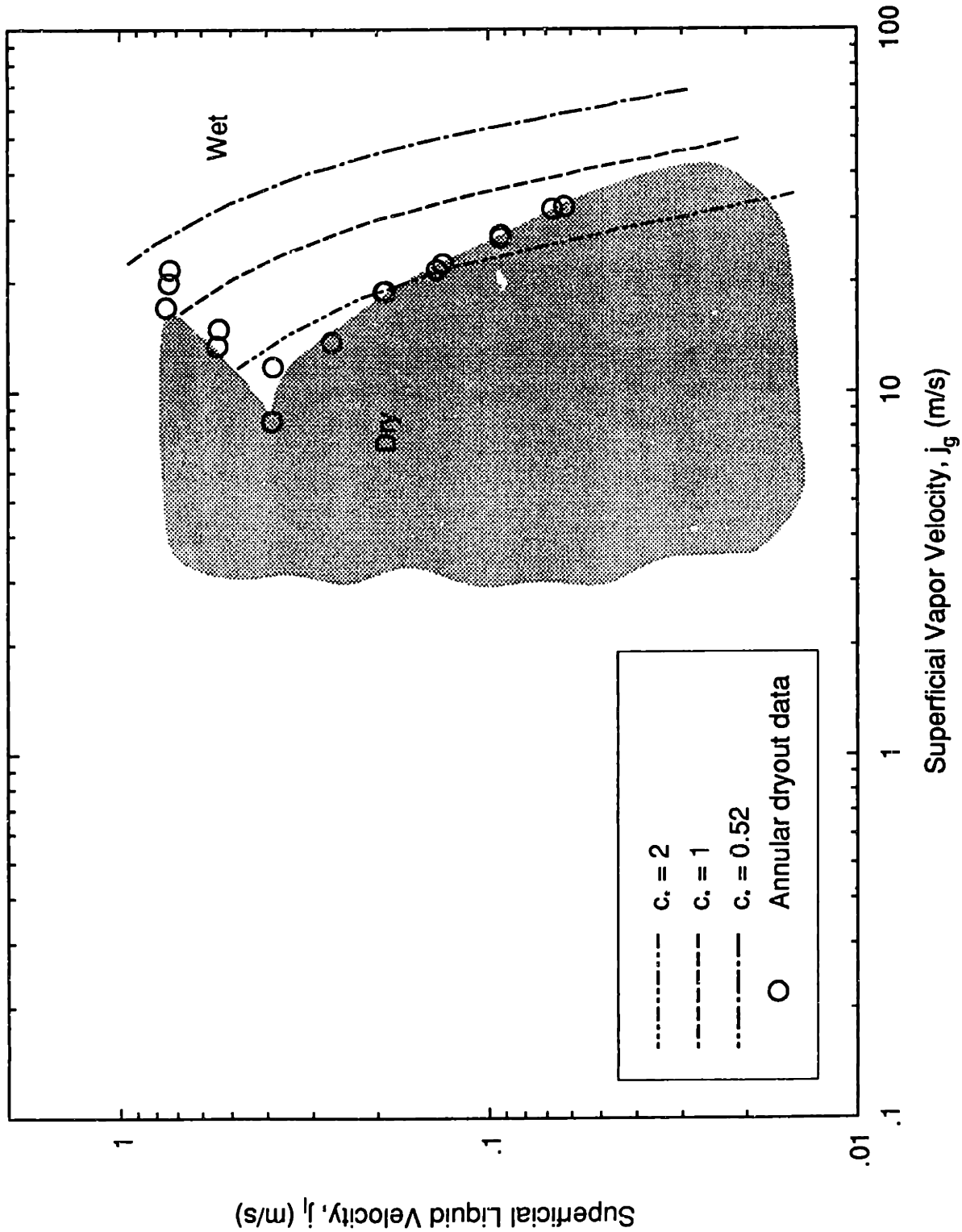

Figure 7.10: Effect of changing C_* on the predicted boundary

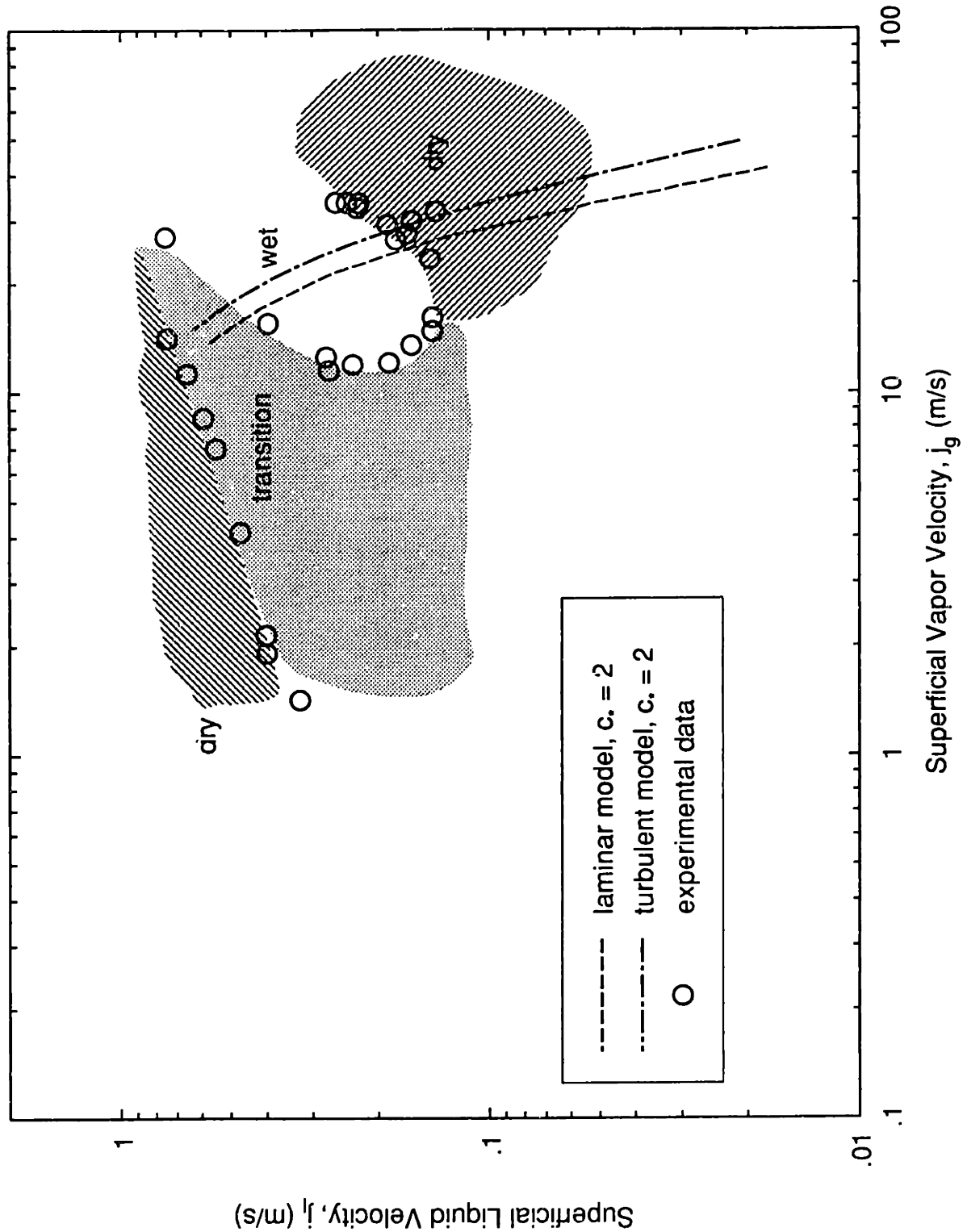

Figure 7.11: Comparison of annular transition models with $q'' = 146$ kW/m^2 data

First, the Colebrook approach to the friction factor computation is not appropriate because it does a poor job of prediction, it was intended for true sand roughness, and the necessity for specifying C_h without any basis is weak. Secondly, the choice of laminar or turbulent film flow models is not clear. Visual observation of the film would seem to indicate that it is turbulent, but a calculation of Reynolds number based on the axial film flow rate gives a value on the order of 100's depending on the precise conditions. For a free surface film, the transition Reynolds number is about 2000 which would say that the film is certainly laminar. On the other hand, it would seem likely that the turbulent gas core would help impart turbulence in the film.

For both heat fluxes tested, the laminar film model agrees better. In addition, the laminar film derived boundary is not as strongly dependent on heat flux which better represents the data trend. Since it is difficult to discern this from Figures 7.10 and 7.11, the boundary dependence on heat flux was computed and shown in Figure 7.12 for a liquid level of h/D = 0.25. Essentially, Figure 7.12 gives the minimum vapor velocity for the annular transition at h/D = 0.25. The steeper slope indicates the greater sensitivity for the turbulent case. It can be shown that the turbulent film velocity profile is nearly linear compared to parabolic for the laminar film. A consequence is that the film flow depends on τ_i^2 and τ_i^3 for the turbulent and laminar cases respectively; thus the smaller sensitivity for laminar films. Consequently, there is more support for the laminar, annular film.

Finally the choice of C_*, which relates the secondary flow to the upper and lower core friction velocities was based on a data fit of single phase air flow and sand roughness. The extrapolation to this case was dubious, so it seemed reasonable to adjust C_*

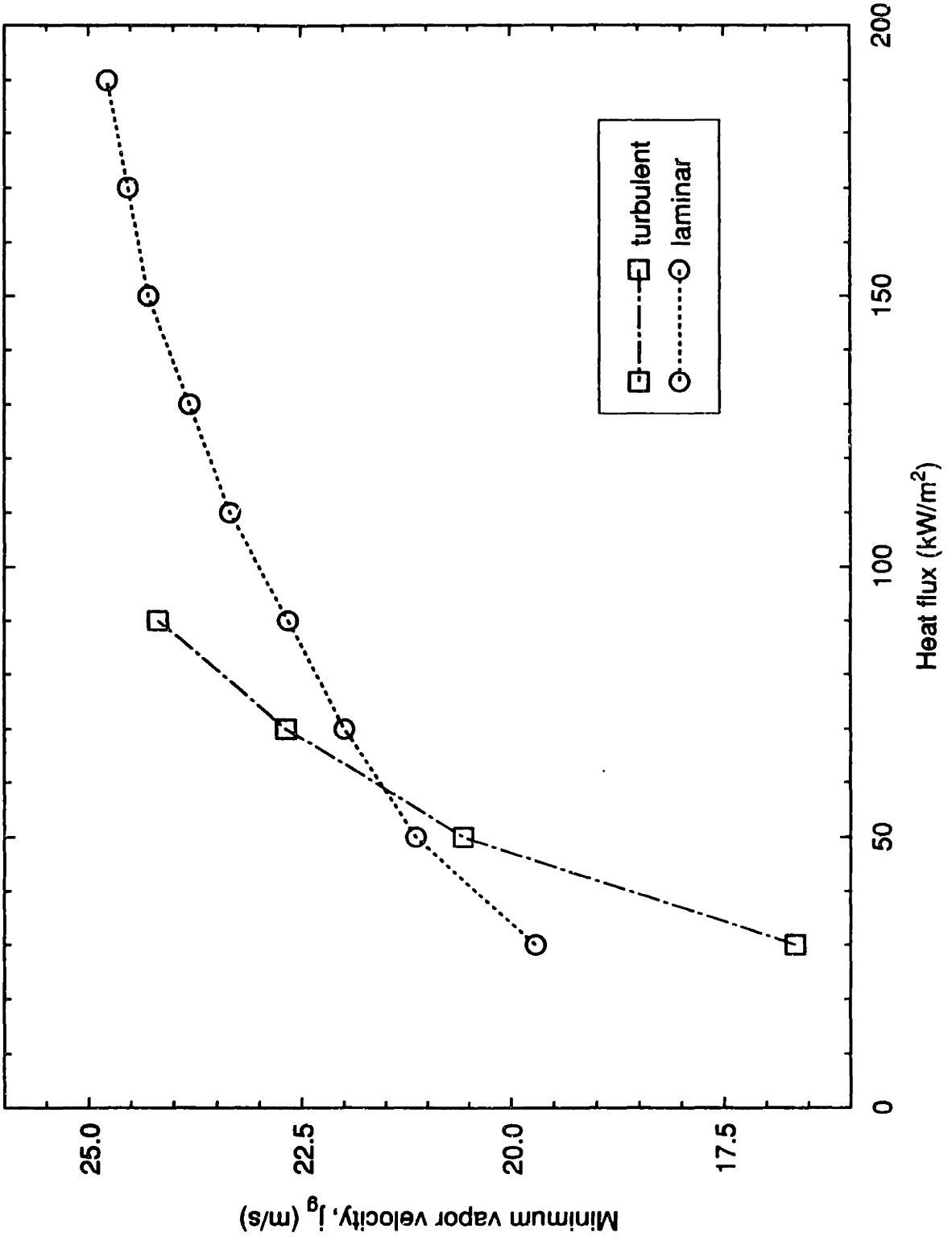

Figure 7.12: Calculated dependence of models on heat flux

to fit this data. Unfortunately, $C_* = 2$ was not universal; it did not predict both heat fluxes. Also, a computation of the secondary flow velocity with $C_* = 2$ gave values from 20-50% of the axial velocity which is unreasonable.

In this analysis, it was attempted to build a model based as much as possible on physical principles and well founded correlations without relying on fitting empirical constants to the data. The only empirical constant (C_*) used in this modeling was determined from a separate experimental database. Given this constraint, and the gross simplifications employed, the prediction of the annular flow transition using the laminar film theory is not unreasonable. A more sophisticated analysis might be concerned with the inherent unsteadiness and spatial variations of the annular film thickness.

CHAPTER 8

Conclusions

8.1. Findings concerning design

• In the horizontal two-phase flow experiments tube top overheating or oscillating temperatures resulting from dryout were found to exist under a variety of conditions. The tube dryout can be classified into four types:

1) Stratified flow dryout which is present at low liquid and vapor flow rates. This regime possesses two bounds: one leading to a transition to slug flow and the other leading to a transition to annular flow.

2) Intennittent flow dryout where the pipe wall temperature oscillates due to the periodic flow.

3) Very high quality dryout which was experienced only at the highest heat flux tested.

4) In addition, there is an entrance effect dryout which has associated high wall temperatures as in the stratified case, but is initiated by a flow disturbance immediately upstream.

• The conservative Ruder recommendation that the entrance liquid Froude number be kept greater than unity insures no dryout in the intermittent or wavy stratified regimes. It has proven conservative here as well, and remains our recommendation. Ruder's intermittent model predicted that the minimum liquid velocity scales with pipe diameter and intermittent dryout would govern for two inch pipes. Based on those results for one inch pipe and these results, scaling the liquid velocity by $\sqrt{D}$ is more appropriate.

• The fabrication details of the piping system can have a marked effect on the downstream thermal behavior.

• There is a quality limit above which tube wall overheating will occur which depends on heat flux. For a heat flux of 146 kW/m^2 this limit was x = 8.6%. This limit defines the usable range for horizontal steam generating tubes.

• For circumferentially uniform heat flux, dryout first occurs at the tube top. Determination of the dryout location when non-uniform heat flux is used (FBC's) will depend on the precise heat loading profile. The insensitivity of the intermittent dryout region to heat flux would suggest that the dryout region for non-uniform heat flux is unaltered. $Fr_l \geq 1$ is recommended to avoid tube overheating.

8.2. Dryout mechanisms

Stratified flow

• The stratified flow limit, which is the case of a stationary bubble, was found to agree

quite well with the dryout criterion given by $Fr_l \leq 0.542$.

Intermittent flow

- The measured film thickness for long times is about a factor of two less than the viscous flow drainage solution yields. The presence of surface waves is believed to have biased the measurement.

- The measured slug frequencies were considerably higher than those calculated using the fully-developed flow correlation employed in the Ruder analysis.

- Application of a high heat flux gave a significant enhancement of slug frequency over adiabatic conditions and reduced the tendency toward dryout.

- The relative surface area where bubble nucleation was observed was small even at high heat flux. The effect of bubble nucleation is thus negligible.

- Visual observation revealed negligible mass removal or transfer in the form of entrained droplets from the bursting bubbles.

- Nucleation in the thinning film at atmospheric pressure is suppressed quite rapidly due to the film's high thermal conductance.

Annular flow

- At the stratified-annular transition, the dominant mechanism for maintaining the tube top wet is secondary flow in the vapor core. The vapor flow rates are too low for

significant entrainment to play a role.

- At the high quality dryout boundary, significant droplet entrainment takes place but is insufficient to prevent dryout beyond x = 8.6% at $q'' = 146\ kW/m^2$ in a two inch pipe at atmospheric pressure.

Appendixes

Appendix A

Analysis of pipe temperature oscillations in intermittent flow

The intermittent dryout data defined on the four maps is dependent on the choice of fluctuation threshold. The chosen values were scaled with heat flux but were also dictated by defining clear regions of dryout points with a minimum of exceptional points.

The choice of these threshold values for oscillating temperatures was checked by simulating the unsteady thermal behavior of the pipe wall under the conditions where there is volumetric heat generation and a time varying inside heat transfer coefficient. The model of the pipe wall is now presented. Since the pipe wall thickness, $b \ll R$, it is safe to treat the wall as a 1-D slab. The transient conduction equation is:

$$\frac{\partial T}{\partial t} = \alpha \frac{\partial^2 T}{\partial x^2} + \frac{q'''}{\rho b c_{ss}} \qquad \text{(A-1)}$$

where q''' is the volumetric heat generation, x is the direction normal to the slab of thickness b. The boundary conditions are:

$$\frac{\partial T(b,t)}{\partial x} = 0 \qquad \text{(A-1a)}$$

and

$$k_{ss} \frac{\partial T(0,t)}{\partial x} = h_i(t)(T(0,t) - T_s) \qquad \text{(A-1b)}$$

where $x=0$ is the inside pipe surface, $h_i(t)$ is the time varying heat transfer coefficient associated with slug flow and T_s is the free-stream (saturation) temperature of the two-phase flow. Because we are interested in the long time behavior of this problem, the initial condition is arbitrary.

The equations above were left in dimensional form and the problem was solved using an explicit finite difference method. Starting with an assumed initial temperature distribution, the interior nodes were solved at the next time step using the discretized governing equation. The boundary temperatures were then solved. In particular, the inside wall temperature was solved using the h(t) from the previous time step. The inside heat transfer coefficient was varied as follows: For some period of time (parameter) the slug is passing a point and a constant h (5000 W/m^2K) was used. Then film drainage and evaporation took place. A discretized form of equation (5-11) was employed where q'' is now a function of time because the pipe temperature is oscillating. The heat flux q'' was found from the previously calculated wall gradient $k_{ss}\partial T(0,t)/\partial x$. The film was allowed to completely deplete before another slug passed (impending dryout). The amplitude of the *outside* wall temperature was found when the solution became periodically steady.

The results were parameterized using average heat flux and slug period. Figure A.1 shows the results of these simulations. It would appear that the fluctuation amplitude is as dependent on the time required for the slug to pass as it is on the heat flux. The chosen dryout threshold is shown for comparison. It appears that the threshold values deemed appropriate during data analysis are not unreasonable; falling within the predicted values over the range of heat flux and slug passage times. The chosen values correspond to slug passage times between one and two seconds which may be slightly high based the observations of the system frequency.

Thus, to be more precise, it is necessary to know the slug frequency at an operating condition in order to predict an appropriate value of the outside wall temperature

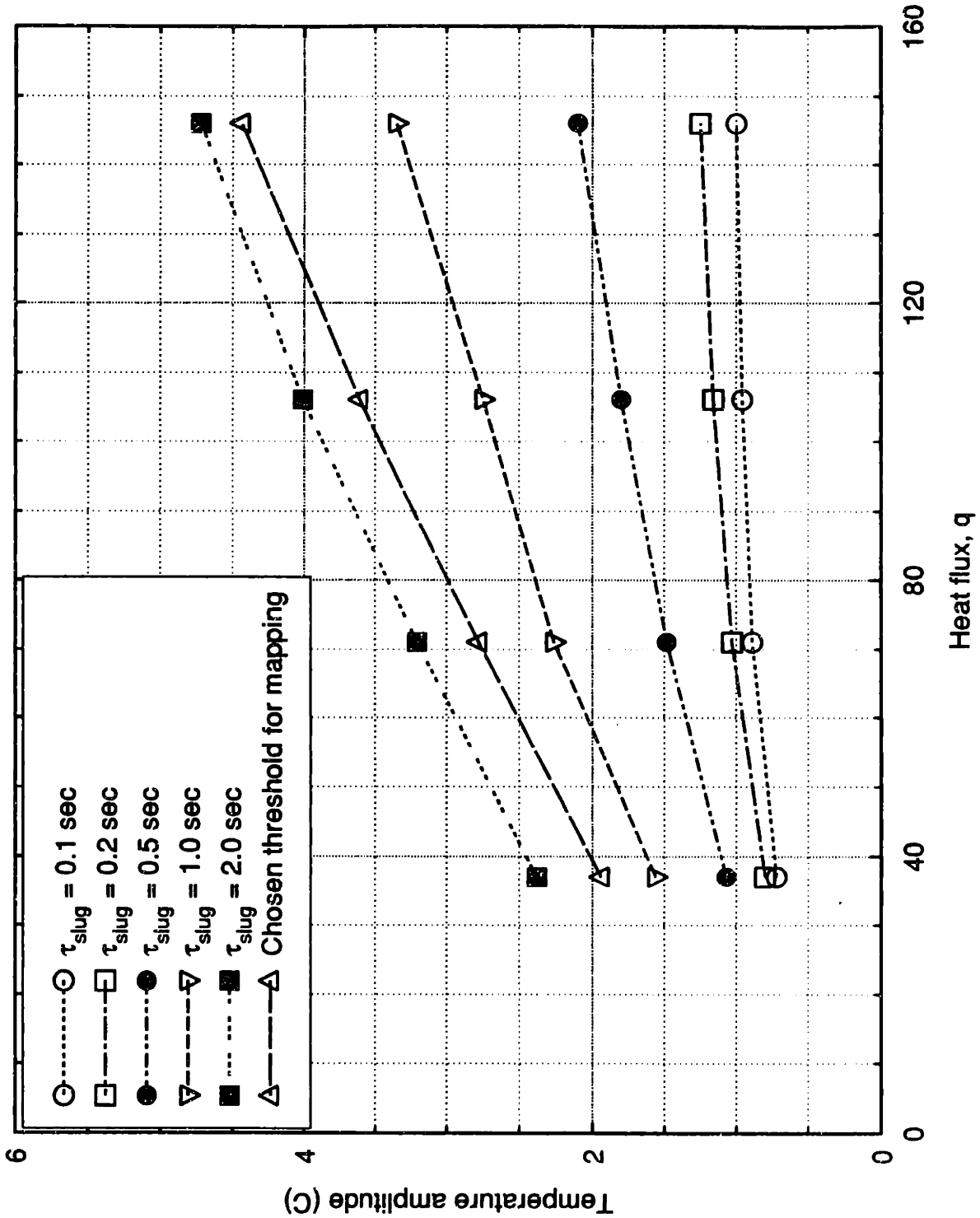

Figure A.1: Oscillating temperature amplitude vs. heat flux

oscillation. The slug frequency was not measured during the acquisition of these temperature traces and it would be difficult to accurately extract this from the T(t) data. In fact, if one knew the slug frequency and could rely upon the dryout time calculation, knowledge of the wall temperature fluctuations would be unnecessary.

Another uncertainty lies in the fact that temperature oscillations will exist in a periodic flow at zero heat flux because the pressure at a fixed location varies periodically. For the present system, these oscillations are about 1 psi and the corresponding change in saturation temperature is about 3.5^0F. This will increase the oscillation amplitude accordingly. In addition, the simulation does not account for the response character of the thermocouples. The added response time would tend to bring down the fluctuation amplitude which may in fact counteract the increase due to saturation temperature changes.

Concluding, there are many factors that influence the temperature response measured on the outside of the pipe in heated slug flow. It is not a simple matter of measuring a temperature or temperature amplitude. It must be born in mind that the inference of dryout incipience on the inside wall is very indirect this way. It is difficult to quantify all the effects and make a reliable measurement. However, the present study has presented the most detailed analysis to date on the precise means and justification for the inference of dryout.

Appendix B

Sensitivity of the intermittent dryout region to choice of temperature threshold

The results presented in Appendix A indicate that choice of the temperature fluctuation threshold defining dryout is not a trivial matter and seems to depend on the precise conditions employed. The choice employed in this work was built around showing contiguous regions of dryout points. This philosophy, though seemingly not well founded, has some basis. The phenomenon of dryout is expected to fall in continuous regions on the flow regime map. Stray data points with no neighbors have a lower credibility and are probably a measure of "noise", which includes numerous effects. Also, considered in the decision process was the scaling of the threshold with heat flux, while insuring that the threshold was not too small to be contained within noise and not too large as to miss the dryout bound.

The effect of changing the threshold on the intermittent dryout region was studied and presented here. Figures B.1 through B.4 show the dryout region in intermittent flow using ΔT_{fluc} values above and below the limits chosen in this work. Figure B.1 well illustrates what has been discussed. For $\Delta T_{fluc} > 2.5^0$, points can appear over all parts of the map without (m)any neighbors. Using $\Delta T_{fluc} > 4.5^0$ clearly satisfies all three criteria, but if one looks closely, it is seen that 4.5^0 filters data points too much; there are a few isolated points that satisfy this criteria without exceeding the other two. In short, it would appear that $\Delta T_{fluc} > 3.5^0$ is the best compromise for this heat flux.

The same observations can be made in Figure B.2. At the next higher heat flux (Figure B.3), it seems that the largest threshold is too large for complete continuity,

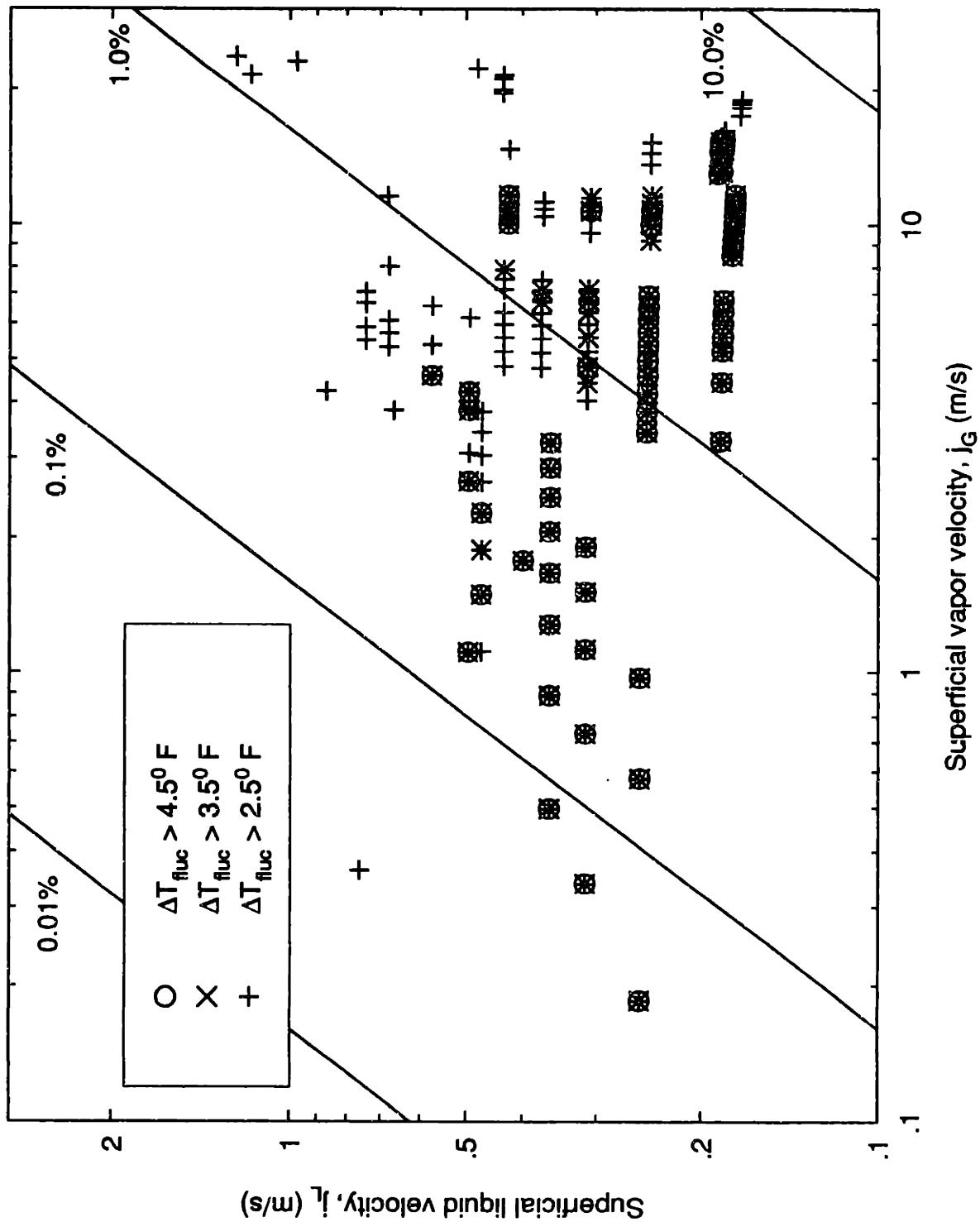

Figure B.1: Intermittent dryout data for q" = 37kW/m^2

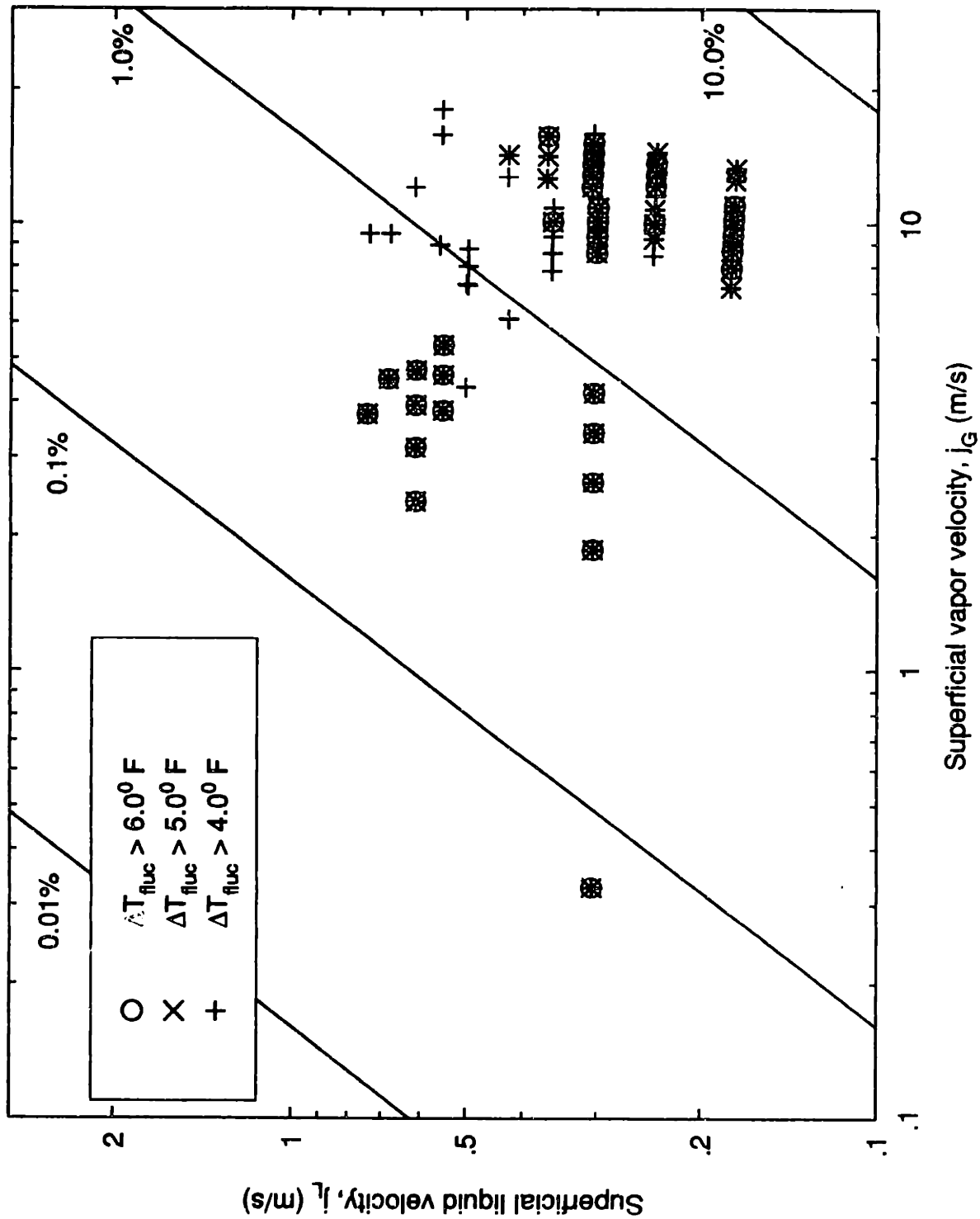

Figure B.2: Intermittent dryout data for q″ = 71kW/m^2

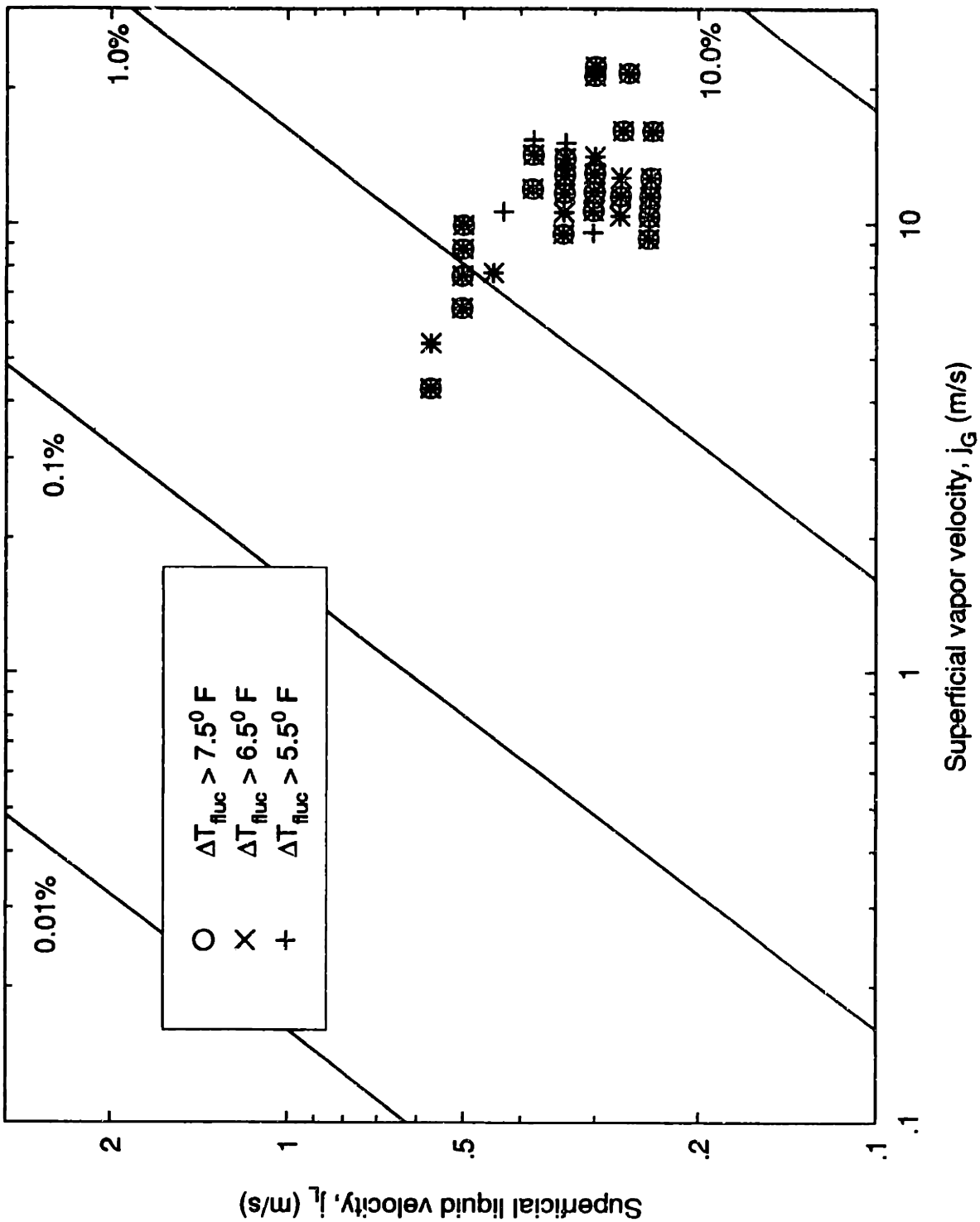

Figure B.3: Intermittent dryout data for q″ = 106kW/m^2

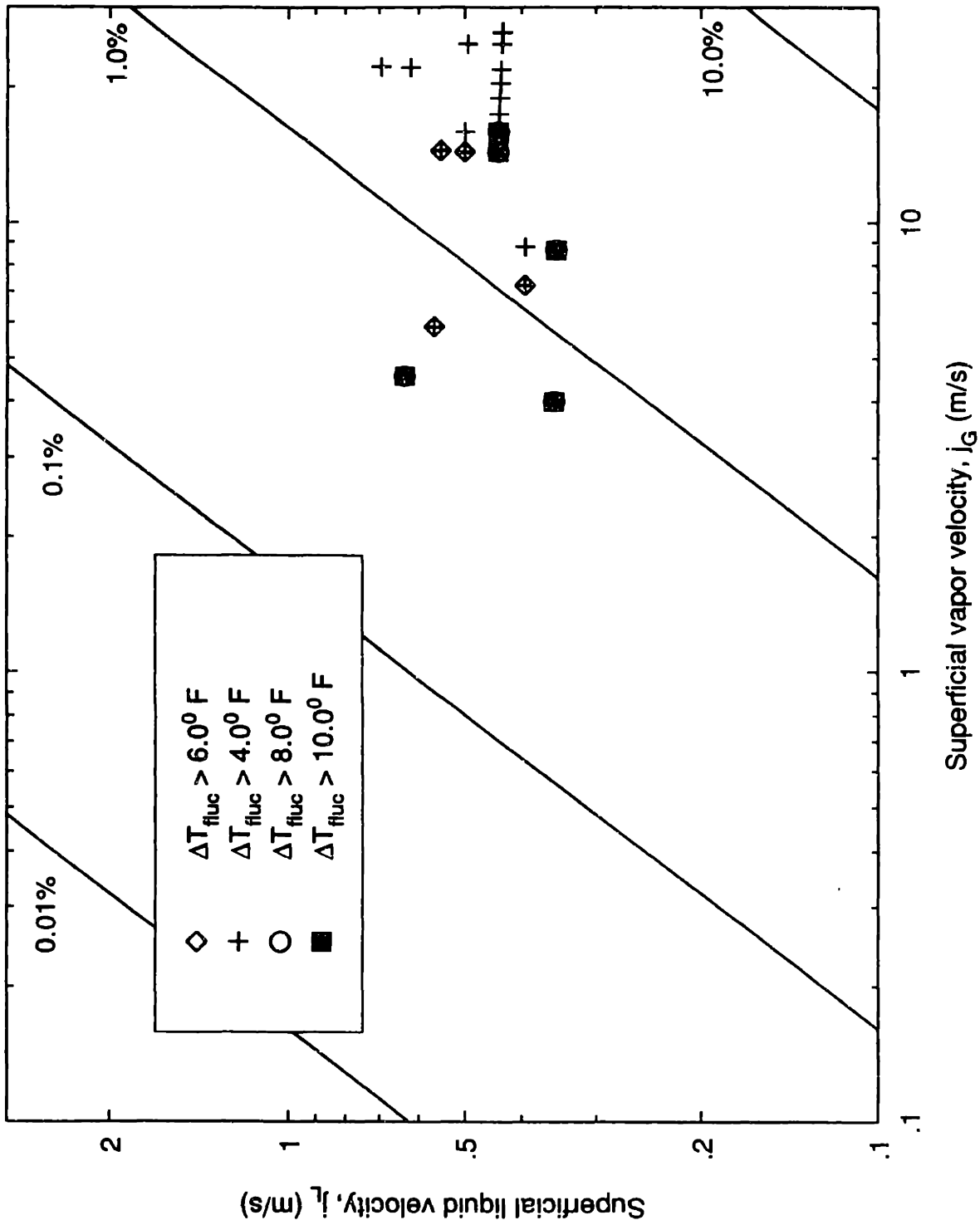

Figure B.4: Intermittent dryout data for q″ = 146kW/m^2

but both $\Delta T_{fluc} > 5.5^0, 6.5^0$ do a good job. It should be remembered that scaling with heat flux was a constraint used dictating the choice of $\Delta T_{fluc} > 6.5^0$. The results of the previous appendix support this method. The data of the highest heat flux are too sparse to conclude anything, but $\Delta T_{fluc} > 8.0^0, 10.0^0$ give the same result. In fact, with the exception of the small (2.5^0) threshold used (see Figure B.1), the dryout region is always below $j_l = 0.75$m/s ($Fr_l < 1$). Though the inference to dryout is a difficult and indirect step it can be stated that temperature fluctuations in the pipe will not be large when the liquid Froude number is above unity.

Appendix C

Inclusion of acceleration in the falling film momentum equation

In the previous analysis (see section 5.2.2), the acceleration terms were ignored in the momentum equation. The more accurate formulation is given by equation 5-2:

$$\frac{\partial u}{\partial t} + u\frac{\partial u}{\partial x} + v\frac{\partial u}{\partial y} = g_x + \nu_l\left[\frac{\partial^2 u}{\partial y^2} + \frac{\partial^2 u}{\partial x^2}\right] \tag{5-2}$$

subject to the no-slip condition,

$$u(x,0,t) = v(x,o,t) = 0, \tag{5-2a}$$

the zero shear condition,

$$\frac{\partial u}{\partial y}(x,\delta,t) = 0, \tag{5-2b}$$

and the initial condition:

$$u(x,y,0) = v(x,y,0) = 0 \tag{5-2c}$$

Clearly the acceleration terms have importance during free-fall which lasts approximately 0.1 seconds. When viscosity has affected the entire remaining film, these terms are still non-zero.

An order-of-magnitude approach can justify neglecting the advective terms. If we take U_{max} as the velocity scale, R as the x-direction length scale, and δ as the y-direction length scale, then the continuity equation says that $v \approx -U_{max}\delta/R$. The $u\,\partial u/\partial x$ and $v\,\partial u/\partial y$ terms are the same order of magnitude but *opposite* in sign (in contrast to boundary layer problems), so there is at least partial cancellation.

The gravity-driven viscous result indicates a velocity that changes with thickness, which in turn depends on time. Thus, the temporal acceleration is negative, so it adds

to the gravity term resulting in a thinner film prediction. The value of the temporal acceleration can be approximated using this result. To an order of magnitude,

$$\frac{\partial u}{\partial t} \approx \frac{\partial u_{max}}{\partial t} \tag{C-1}$$

$$u_{max} = \frac{g\delta^2}{2\nu_l} \tag{C-2}$$

Substituting the expression for film thickness (equation 5-10) gives

$$\frac{\partial u}{\partial t} \approx -\frac{3R}{4t^2} \tag{C-3}$$

This acceleration is one tenth of gravity at t = 0.15sec, δ = 0.16 mm, or around the "knee" of the drainage curve.

A more convincing answer can be obtained by solving the unsteady problem:

$$\frac{\partial u}{\partial t} = g_x + \nu_l \frac{\partial^2 u}{\partial y^2} \tag{C-4}$$

with boundary conditions (Note: these boundary conditions have been reversed which for the purpose here is irrelevant):

$$u(\delta,t) = 0 \tag{C-4a}$$

$$\frac{\partial u(0,t)}{\partial y} = 0 \tag{C-4b}$$

and the initial condition:

$$u(y,0) = 0 \tag{C-4c}$$

To get this set in a more tractable form, the following transformation is made:

$$U = u - g_x t \tag{C-5}$$

This results in the following governing equation:

$$\frac{\partial U}{\partial t} = \nu_l \frac{\partial^2 U}{\partial y^2} \tag{C-6}$$

with boundary conditions:

$$U(\delta,t) = -g_x t \tag{C-6a}$$

$$\frac{\partial U(0,t)}{\partial y} = 0 \tag{C-6b}$$

and the initial condition:

$$U(y,0) = 0 \tag{C-6c}$$

The solution of this set is given by:

$$U(y,t) = -gt\left\{1 - \frac{1}{2Fo}\left[1-\left[\frac{y}{\delta}\right]^2\right] + \frac{2}{Fo}\sum_1^\infty \frac{\sin\beta_i\cos(\beta_i y/\delta)}{\beta_i^3} e^{-\beta_i^2 Fo}\right\} \tag{C-7}$$

where $Fo = \nu_l t/\delta^2$ and $\beta_i = \pi/2, 3\pi/2, 5\pi/2, \ldots$. Transforming back to the velocity, u gives:

$$u(y,t) = \frac{g\delta^2}{\nu_l}\left\{\frac{1}{2}\left[1-\left[\frac{y}{\delta}\right]^2\right] - 2\sum_1^\infty \frac{\sin\beta_i\cos(\beta_i y/\delta)}{\beta_i^3} e^{-\beta_i^2 Fo}\right\} \tag{C-8}$$

As can be seen, for large time, the summation term approaches zero and the solution collapses back to the parabolic velocity distribution for the purely viscous case.

Integrating this velocity through the film thickness to get the flow rate at any time gives:

$$\Gamma = \frac{g_x\delta^3}{\nu_l}\left[\frac{1}{3} - 2\sum_1^\infty \frac{e^{-\beta_i^2 Fo}}{\beta_i^4}\right] \tag{C-9}$$

The continuity equation gives the evolution of film thickness:

$$\frac{\partial\delta}{\partial t} + \frac{\partial\Gamma}{\partial x} = 0 \tag{C-10}$$

Substituting the flow rate equation into this and applying the symmetry condition

$(\partial/\partial x = 0)$ at the tube top gives:

$$\frac{\partial \delta}{\partial t} + \frac{g\delta^3}{R\nu_l}\left[\frac{1}{3} - 2\sum_1^{\infty}\frac{e^{-\beta_i^2\nu_l t/\delta^2}}{\beta_i^4}\right] = 0 \qquad \text{(C-11)}$$

subject to an initial thickness condition.

This evolution equation was solved numerically with $\delta_0 = 2$mm. The results are shown in Figure C.1. For comparison, the drainage for the purely viscous flow (velocity already established initially) is shown. As can be seen, the unsteady analysis has a slower response initially owing to the acceleration of the fluid from rest. As a result, the viscous solution is always thinner and the inertial solution effectively lags behind. For better comparison, the viscous solution was offset in time by this lag. This results in nearly coincidental solutions beyond $t = 0.15$ sec. The time and thickness where the curves are indistinguishable also happens to agree with the crossing of the boundary layer growth curve found from $\delta_{bl} = \sqrt{\nu_l t}$.

It is concluded that inclusion of the temporal acceleration term only gives a significant discrepancy for very short times. Use of the pure gravity-driven viscous model is acceptable for times on the scale of the slug period. The unsteady model therefore cannot predict the experimental results which gave thicknesses about half of that predicted with inertia-free model.

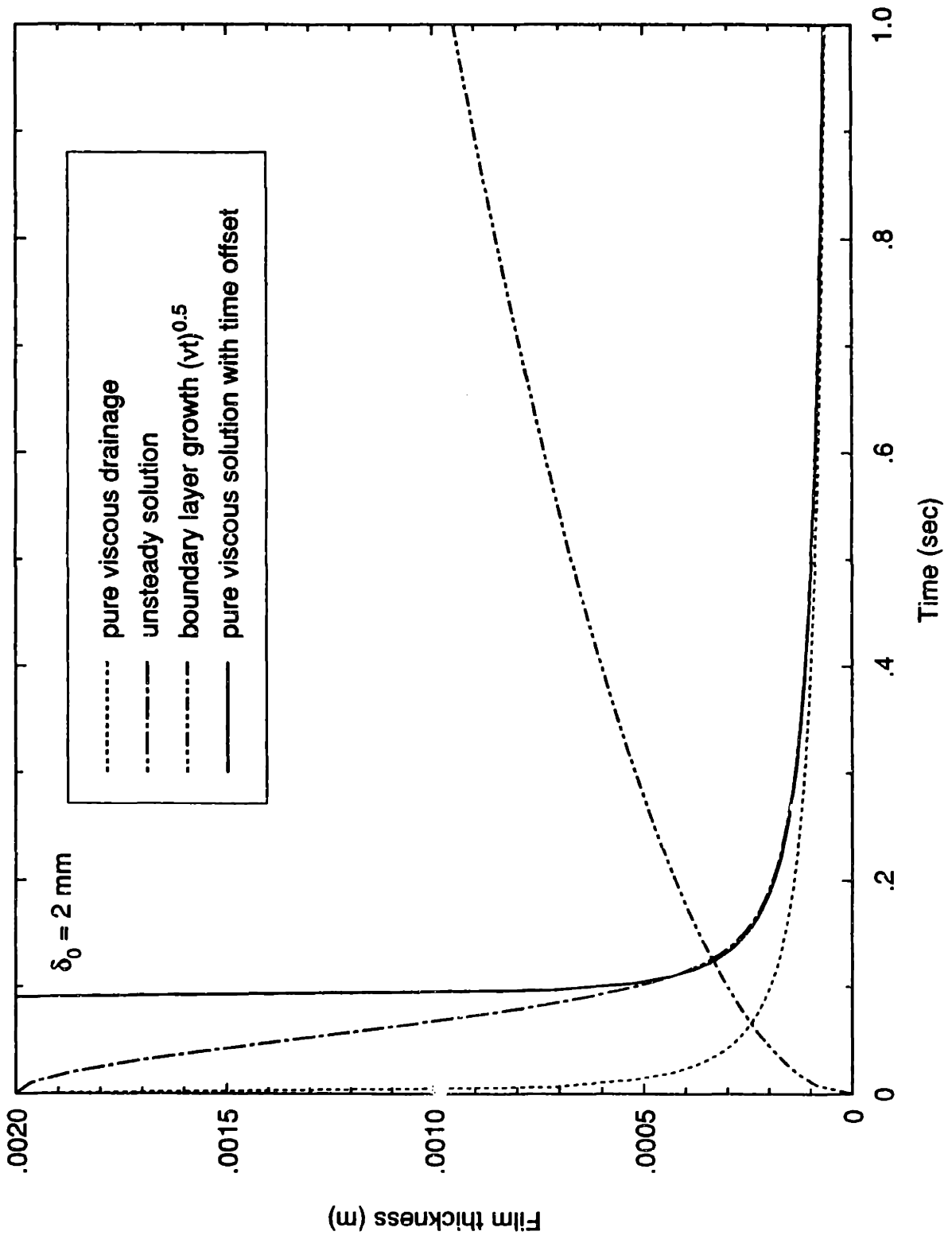

Figure C.1: Comparison of film drainage for steady-viscous and unsteady-viscous models

Appendix D

The effect of wave spreading extent on the stratified-annular transition

In the analysis of chapter 7, the dryout criterion was derived with the assumption that wave spreading brings an ample supply of liquid to the $\theta = 90^0$ point, but no further. The visual observations of annular flow support this assumption, but were not quantitative. The effect of altering the angle in the analysis was investigated and presented here.

The core flow model is unchanged, but there are three changes to the laminar film flow model: a) the film flow required is less as θ decreases. b) the gravity term scales with $\sin\theta$. c) the secondary flow velocity scales with $\sin\theta$. The required flow is given by:

$$\Gamma_\theta = \frac{q''D\theta}{2\rho_l h_{fg}} \tag{7-20}$$

The actual flow depends on the interfacial shear stress given by:

$$\Gamma_\theta = \frac{\tau_i^3}{6\rho_l^3 g^2 \nu_l} \tag{D-1}$$

According to the measurements of Darling & McManus,[35] the secondary flow velocity depends on $\sin\theta$ such that it is maximum at the tube side and a stagnation point results at the tube top. Under fixed conditions, the interfacial shear $\tau_i \approx \sin\theta$. Then,

$$\tau_{max} = \frac{\tau_i(\theta)}{\sin\theta} = \frac{(6\rho_l^3 g^2 \nu_l \Gamma_\theta)^{1/3}}{\sin\theta} \tag{D-2}$$

Substituting the expressions for Γ_θ and g will give the overall dependence of the maximum shear on the angle θ, where it is remembered that θ is the angle up to which fluid is delivered by wave action. The resulting dependence shows that

$\tau_{max} = (\theta/\sin\theta)^{1/3}$. This function increases with θ, indicating that solving for the necessary shear at the tube side represents a more stringent criterion than for any angle less than 90^0. It also says that if wave spreading fails to bring liquid to the tube side the bound derived is not the limit.

If one assumes for example $\theta = 45^0$ (which is rather extreme), the decrease in the necessary shear is only about 11% with an accompanying vapor velocity at the transition about 11% lower. This is indicated in Figure D.1 which shows the predicted transition bounds for 45^0 and 90^0. Thus, the bound is not sensitive to the angle up to which fluid is carried by wave spreading, although for low values of the liquid level, liquid may not reach the 90^0 point.

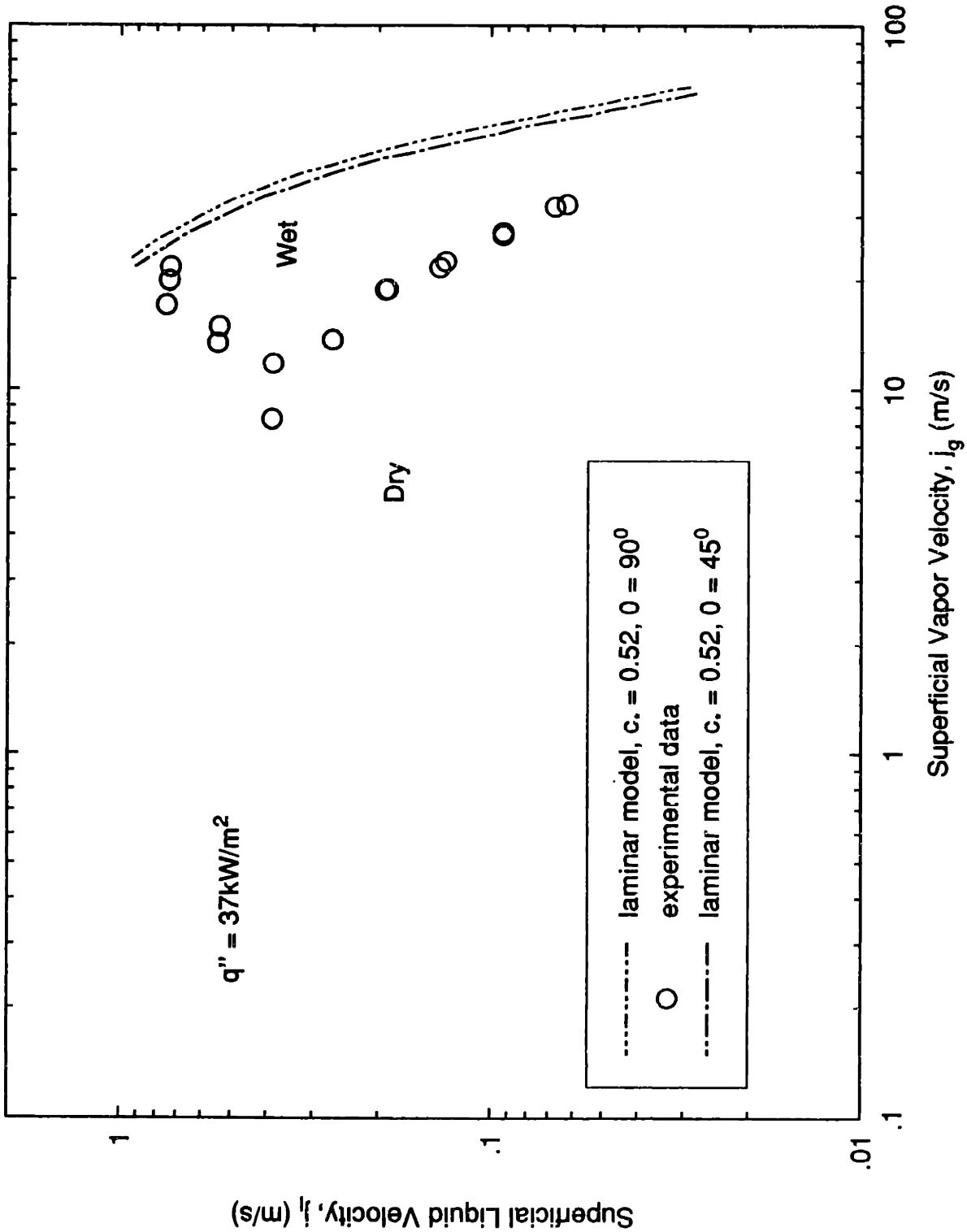

Figure D.1: Predicted annular flow bound for $\theta = 45^0$, 90^0

References

1. Y. Taitel and A. Dukler, "A Model for Predicting Flow Regime Transitions in Horizontal and Near Horizontal Gas-Liquid Flow," *AIChE Journal* 22(1) pp. 47-55 (Jan. 1976).

2. J.M. Mandhane, G.A. Gregory, and K.A. Aziz, "A Flow Pattern Map for Gas-Liquid Flow in a Horizontal Pipeline," *Int. J. Multiphase Flow* 1 pp. 537-54 (1974).

3. J. Weisman, D. Duncan, J. Gibson, and T. Crawford, "Effects of Fluid Properties and Pipe Diameter on Two-Phase Flow Patterns in Horizontal Lines," *Int. J. Multiphase Flow* 5 pp. 437-62 Pergamon/Elsevier, (1979).

4. M.A. Styrikovich and Z.L. Miropolski, "Rassloyeniye Potoka Paravodyanoy Smesi Vysokogo Dovlenia V Obogrevayemoy Gorizontalnoy Trube (Stratification in Vapor-Water Mixture Flow at High Pressures in Heated Horizontal Tube, in Russian)," *Dokl Akad Nauk, SSSR* LXXXI p. 2 (1950).

5. Z. Ruder, "The Influence of Two-Phase Flow Regimes on Circumferential Temperature Distribution in Horizontal, Steam Generating Tubes," Ph.D Thesis, Dept. of Mechanical Engineering, Ben Gurion University, Israel (1984).

6. J. Lis and J.A. Strickland, "Local Variations of Heat Transfer in a Horizontal Steam Evaporator Tube," *Proceedings of the 4th International Heat Transfer Conference* V(B4.6)(1970).

7. J.M. Robertson, "Dryout in Horizontal Hairpin Waste-Heat Boiler Tubes," *Thirteenth National Heat Transfer Conference*, (69) pp. 55-62 AIChE, (1972).

8. O. Baker, "Simultaneous Flow of Oil and Gas," *Oil Gas J.* 53 p. 185 (1954).

9. S.A. Fisher and S.K.W. Yu, "Dryout in Serpentine Evaporators," *Int. J. Multiphase Flow* 1 pp. 771-91 Pergamon/Elsevier, (1975).

10. M.W.E. Coney, "The Theory and Application of Conductance Probes for the Measurement of Liquid Film Thickness in Two-Phase Flow," *Journal of Physics E: Scientific Instruments* 6 pp. 903-10 (1973).

11. M.W.E. Coney, "The Analysis of a Mechanism of Liquid Replenishment and Draining in Horizontal Two-Phase Flow," *Int. J. Multiphase Flow* **1** pp. 647-69 (1974).

12. Zvi Ruder, Avram Bar-Cohen, and Peter Griffith, "Major Parametric Effects on Isothermality in Horizontal Steam Generating Tubes at Low- and Moderate Qualities," *Int. J. of Heat and Fluid Flow* **8**(3) pp. 218-27 (1987).

13. T.B. Benjamin, "Gravity Currents and Related Phenomena," *J. Fluid Mech.* **31** pp. 209-48 (1968).

14. Avram Bar-Cohen, Zvi Ruder, and Peter Griffith, "Development and Validation of Boundaries for Circumferential Isothermality in Horizontal Boiler Tubes," *Int. J. Multiphase Flow* **12**(1) pp. 63-77 (1986).

15. G.A. Gregory and D.S. Scott, "Correlation of Liquid Slug Velocity and Frequency in Horizontal Cocurrent Gas-Liquid Slug Flow," *AIChe Journal* **15**(6) pp. 933-5 (1969).

16. G.C. Gardner, "Drainage and Evaporation of a Liquid Film with Salt Deposition upon a Horizontal Cylindrical Surface," *Int. J. Heat Mass Transfer* **15** pp. 2063-75 (1972).

17. I.S. Gradshteyn and I.M. Ryzhik, *Table of Integrals, Series, and Products*, Academic Press, New York (1980).

18. K. Hanjalic and B. E. Launder, "Fully developed asymmetric flow in a plane channel," *J. Fluid Mech.* **51** pp. 301-35 (1972).

19. G.F. Hewitt, R.D. King, and P.C. Lovegrove, "Liquid Film and Pressure Drop Studies," *Chemical and Process Engineering*, pp. 191-200 (April 1964).

20. J.A. Shmerler and I.A. Mudawwar, "Local Evaporative Heat Transfer Coefficient in Turbulent Free-Falling Liquid Films," *Int. J. Heat Mass Transfer* **31** pp. 731-42 (1988).

21. W.J. Marsh and I. Mudawar, "Predicting the Onset of Nucleate Boiling in Wavy Free-Falling Turbulent Liquid Films," *Int. J. Heat Mass Transfer* **32**(2) pp. 361-78 (1989).

22. E.J. Greskovich and A.L. Shrier, "Slug Frequency in Horizontal Gas-Liquid Slug Flow," *Ind. Eng. Chem. Process Des. Develop.* **11**(2) pp. 317-8 (1972).

23. A.E. Dukler and Y. Taitel, "Flow Pattern Transition in Gas-Liquid Systems: Measurement and Modeling," pp. 1-94 in *Multiphase Science and Technology*, ed. G.F. Hewitt, J.M. Delhaye and N. Zuber,Hemisphere (1986).

24. L. Biasi, G.C. Clerici, S. Garribba, R. Sala, and A. Tozzi, "Studies on Burnout, Part 3 - A New Correlation for Round Ducts and Uniform Heating and its Comparison with World Data," *Energia Nucleare* **14**(9) pp. 530-6 (Sept. 1967).

25. J.E. Laurinat, T.J. Hanratty, and W.P. Jepson, "Film Thickness Distribution for

Gas-Liquid Annular Flow in a Horizontal Pipe," *PhysicoChemical Hydrodynamics* **6**(1/2) pp. 179-95 Pergamon Press Ltd., (1985).

26. D. Butterworth, "Air-Water Annular Flow in a Horizontal Tube," *Progress in Heat and Mass Transfer* **6** pp. 235-51 (1972).

27. G.F. Hewitt and N.S. Hall-Taylor, *Annular Two-Phase Flow,* Pergamon Press, Oxford (1970).

28. R.J. Anderson and T.W.F. Russell, "Circumferential Variation of Interchange in Horizontal Annular Two-Phase Flow," *Ind. Engng. Chem. Fundam.* **9** pp. 340-4 (1970).

29. D. Butterworth and D.J. Pulling, "A Visual Study of Mechanisms in Horizontal Annular Air-Water Flow," *Report No. AERE-M2556*, UKAEA, (1971).

30. S. Jayanti, G.F. Hewitt, and S.P. White, "Time-Dependent Behaviour of the Liquid Film in Horizontal Annular Flow," *Int. J. Multiphase Flow* **16**(6) pp. 1097-1116 Pergamon Press/Elsevier, (1990).

31. T. Fukano and A. Ousaka, "Prediction of the Circumferential Distribution of Film Thickness in Horizontal and Near-Horizontal Gas-Liquid Annular Flows," *Int. J. Multiphase Flow* **15**(3) pp. 403-19 Pergamon Press/Elsevier, (1989).

32. A.G. Flores, "Dryout Limits in Horizontal Annular Flow," S.M. Thesis, M.I.T., unpublished, Cambridge, MA (1992).

33. G.B. Wallis, *One-Dimensional Two-Phase Flow,* McGraw-Hill (1969).

34. J.O. Hinze, "Experimental Investigation on Secondary Currents in the Turbulent Flow Through a Straight Conduit," *Appl. Sci. Res.* **28** pp. 453-65 (1973).

35. R.S. Darling and H.N. McManus, Jr., "Flow Patterns in Circular Ducts with Circumferential Variation of Roughness: a Two-Phase Analog," *Developments in Mechanics: Proceedings of the 11th Midwestern Mechanics Conference* **5** pp. 153-70 (1968).

36. D. Butterworth, "Note on Fully-Developed, Horizontal Annular Two-Phase Flow," *Chem. Engng. Sci.* **24** pp. 1832-4 (1969).

37. C.F. Colebrook, "Turbulent Flow in Pipes with Particular Reference to the Transition Region Between the Smooth and Rough Pipe Laws," *Journ. of Institution of Civil Engineers*, (1939).

38. H. Schlichting, *Boundary Layer Theory,* McGraw-Hill (1955).

39. G.F. Hewitt and G.B. Wallis, "Flooding and Associated Phenomena in Falling Film Flow in a Tube," *Proceeding of the ASME Multi-Phase Symposium*, p. 62 (1963).